

Martin-Luther Universität
Halle-Wittenberg



International Max Planck
Research School-Nano
MPI-Halle

DISSERTATION THESIS

Micro- and nanophase separated tubes and rods by melt-infiltration of block copolymers into inorganic nanopores

Dissertation

Zur Erlangung des akademischen Grades
Doctor rerum naturalium (Dr. rer. nat.)

vorgelegt der

Naturwissenschaftlichen Fakultät II–Chemie und Physik
der Martin-Luther-Universität Halle-Wittenberg

von

Bhanuprathap Pulamagatta
geb. am 16. October 1980 in India

ausgeführt unter der Leitung von

Prof. Dr. Wolfgang Binder
Professor of Macromolecular Chemistry
Martin-Luther University, Halle-Wittenberg

Gutachter:

1. Prof. Dr. Wolfgang Binder (MLU, Halle)
2. Prof. Dr. Brigitte Voit (TU, Dresden)

Halle (Saale), den 15th Oct-2010

Acknowledgements

This dissertation is a result of three years of work, whereby I have been accompanied and supported by many people. Now comes the pleasant moment that I have the opportunity to express my gratitude to all those individuals, who in one way or another contributed and extended their valuable assistance in completion of this study.

I deem it a rare privilege and immense pleasure to express my cordial gratitude to my supervisor, Prof. Dr. Wolfgang Binder, for introducing me into the polymer chemistry research field. I am very appreciative for his guidance, time for scientific discussions, persistent interest, skilled advices and patience, (to name some of his contributions), throughout my thesis. Without his support, this thesis would not have been possible. I thank him for his concerns and care during the days when I was sick. One simply could not wish for a better, caring and friendly supervisor.

It gives me an immense pleasure to acknowledge Prof. Dr. Martin Steinhart (MPI-Halle and Universität Osnabrueck) for providing the nanoporous templates. I am also thankful to him for his valuable guidance and frequent scientific discussions concerning the nanotube project and his extended help in writing publication.

I would like to show my appreciation to Prof. Dr. Thomas Thurn-Albrecht for allowing me to conduct the physical measurements at their department. Useful discussions with him helped me in understanding and interpreting the X-ray scattering and rheology data.

I pay my special thanks to Dr. Mario Beiner for his valuable guidance, in depth scientific discussions and extended support to perform experiments at his lab. Without his help the nanophase separation studies of our polymers would not have been possible.

Some of the experiments had to be conducted in other departments and my special thanks to all of them who helped me and also made measurements for me. Thanks to Eric YAU for helping in infiltration work and for making large number of TEM and SEM images whenever I needed, Ilja Gunkel for helping in x-ray scattering measurements and analysis of those results with his expertise, Shireesh Pankaj for his valuable time and help in conducting DMA, dielectric spectroscopy and scattering measurements. I also thank Dr. Klaus Schröter for rheology measurements and Dirk Pefferkorn for melt surface energy measurements. Thanks to Dr. Erik Prell for providing autoclave and Samuel for allowing me to use DSC and TGA instruments.

I Thank Max Planck Institute at Halle for considering me as member of International Max Planck Research School (IMPRS) for Nanotechnology and allowing me to use facilities at their institute. I also like to thank all my colleagues and coordinator of IMPRS.

My background being engineering, I had no practical knowledge of synthesis when I started my thesis, but I am grateful to Dr. Robert Sachsenhofer and Dr. Ronald Zirbs for helping me initially to learn and conduct chemical reactions in the lab. In my daily work I have been blessed with a friendly and cheerful group of fellow colleagues like Haitham, Steffen, Katharina, Claudia, Onur, Elena, Matthias, Paul, Parvin, Florian, Ali, Sinem, Robert, Marlen, Maria, Ocha, Sussane and Norman. My special thanks to our secretary Anke Hassi for all the help she offered in official matters.

I thank all my friends in Germany, India and elsewhere for their support and encouragement throughout.

Finally, my deepest gratitude to my Parents, sister (Shilpa) and brother (Venu) for all their love and support and I dedicate this thesis to them.

Abstract

It is highly desirable to combine the functionalities of block copolymers and of tubular nanostructures as the rational design of the internal morphology of tube walls with specific dimensions and composition will allow them to be used as components for functional devices. Melt infiltration of Block copolymers (BCPs) into the anodized aluminum oxide (AAO) nanopores in the past has always yielded solid nanorods by capillary filling. In this work, we demonstrate upon the melt infiltration of specifically designed BCPs, containing fluorinated block, into the AAO porous template forms a precursor film. The solidification of precursor film yields tubular BCP nanostructures exhibiting internal mesoscopic fine structures. Fluorinated norbornene block copolymers were synthesized via ring opening metathesis polymerization (ROMP) using Grubbs type catalyst. The block copolymerization reactions were evaluated using gel permeation chromatography (GPC), nuclear magnetic resonance spectroscopy (^1H NMR) and especially the MALDI-mass- spectrometric method which allowed the monitoring of polymerization directly at the point of crossover-reaction. The fluorinated block tends to segregate to the BCP/air interface and hence, low surface energy of the BCP. Terminal flow of the BCP is apparently not a prerequisite for precursor film formation if the surface energy of the newly formed BCP/air interface is low enough. Thus, tubular BCP nanostructures with walls having mesoscopic fine structures such as concentric lamellae are accessible. Low surface energy of BCP melt was characterized by melt drop method water droplet contact angle measurements. Small angle X-ray scattering (SAXS) and TEM analysis of bulk BCP revealed lamellar and cylindrical bulk morphology (~ 30 nm) which upon melt infiltration forms tubes with concentric lamellar walls with comparable dimensions.

We also report on the formation of self assembled hierarchical nanostructures in norbornene block copolymer bulk containing longer fluorinated alky (C_8) side chains on one of the block. The nanophase separation of fluorinated alkyl side chains from the main polymer chains forms the nanodomain aggregates ($d_{\text{nps}}=3$ nm) within the microphase separated BCP structure ($d=24$ nm). Side chain nano-domains were characterized via X-scattering experiments. Main chain independent side chain dynamics and relaxation were probed using dynamic mechanical analysis (DMA) and dielectric relaxation spectroscopy as a proof for micro and nanophase separated structures.

Abstract

Durch Kombination von Blockcopolymeren mit röhrenförmigen Nanostrukturen gelangt man zu Materialien die durch ihre spezielle Morphologie anwendbar sind für funktionelle Bauteile. Die interne Morphologie der Röhrenwände mit spezifischen Dimensionen und Zusammensetzung ist dabei über das eingesetzte Blockcopolymer einstellbar. Aus früheren Artikeln resultierte die Schmelzinfiltration von Blockcopolymeren in anodische Aluminiumoxid (AAO) Nanoporen, die bisher nur stäbchenförmige Nanostrukturen auf Grund der Kapillar-Füllung ergab. In dieser Arbeit demonstrieren wir die Schmelzinfiltration von Blockcopolymeren mit fluorierten Seitenketten in poröse AAO-Vorlagen unter Bildung eines Präkursor-Films. Dieser Präkursor-Polymerfilm führt nach dem Übergang der Schmelze in die feste Phase zu röhrenförmigen Blockcopolymer Nanostrukturen die eine interne mesoskopische Feinstruktur aufweisen. Norbornen-Blockcopolymere mit fluorierten Seitenketten wurden durch Ringöffnungsmetathesepolymerisation (ROMP) unter Verwendung von Grubbs Katalysatoren hergestellt. Die Blockcopolymerisationen wurden mittels Gel-Permeations-Chromatografie (GPC), Kernspinresonanzspektroskopie ($^1\text{H-NMR}$) und im Besonderen mit MALDI-TOF Massenspektrometrie untersucht, welche die direkte Verfolgung der Polymerisation am Überkreuzungspunkt erlaubte. Die Blöcke mit fluorierten Seitenketten neigen zur Entmischung an der Blockcopolymer/Luft-Grenzfläche was zu einer niedrigen Oberflächenenergie des Blockcopolymeren führt. Im Fall einer niedrigen Oberflächenenergie des Blockcopolymeren ist ein terminales Fließen der Polymer-Schmelze offensichtlich keine Voraussetzung für die Bildung eines Präkursor-Films. Daher sind röhrenförmige Nanostrukturen, deren Wände mesoskopische Feinstrukturen aufweisen, mit dem von uns synthetisierten Blockcopolymer zugänglich. Die Oberflächenenergie des Blockcopolymeren wurde durch die Schmelztropfen Methode und die Wassertropfen-Kontaktwinkel Messung charakterisiert. Die synthetisierten Blockcopolymere weisen je nach Zusammensetzung lamellare oder zylindrische Morphologie (~ 30 nm) auf, welche durch Kleinwinkelröntgenstreuung (SAXS) und TEM-Analyse nachgewiesen werden konnte. Die Schmelzinfiltration des Blockcopolymeren führt zu Nanoröhren mit konzentrisch lamellaren Wänden. Weiterhin wird die Bildung von selbst assemblierenden hierarchischen Nanostrukturen in Norbornen-Blockcopolymeren untersucht, wobei ein

Block eine längere fluorierte Alkyl-Kette trägt (C₈). Die Nanophasen-Separation der fluorierten Seitenketten von der Hauptkette des Polymers führt zu Aggregaten ($d_{\text{nps}} = 3\text{nm}$) innerhalb der durch Mikrophasenseparation gebildeten Blockcopolymerstruktur ($d = 24\text{ nm}$). Diese durch aggregierte Seitenketten gebildeten Nanodomänen wurden mittels Röntgenstreuung untersucht. Den Beweis für Mikro- und Nanophasen separierte Strukturen erbrachte die Untersuchung der Dynamik und des Relaxationsverhaltens der Seitenketten, welche unabhängig von der Hauptkette sind, durch dynamisch mechanische Analyse (DMA) und dielektrischer Relaxationsspektroskopie.

Keywords: Polymer-Nanoröhren, Nanostäbe, Nanofasern, Schmelzinfiltration, Blockcopolymer, Ringöffnungsmetathesepolymerisation (ROMP), Blockcopolymerisation, Überkreuzungsreaktion, Polynorbornen, hierarchische Nanostrukturen, Nanophasen-Separation.

Keywords: Polymer nanotubes, nanorods, nanofibers, melt infiltration, block copolymer, ring opening metathesis polymerization (ROMP), block copolymerization, crossover reaction, Poly (norbornene), hierarchical nanostructures and nanophase separation.

Contents

Section 1

Introduction and motivation	1
1.1. Block copolymers (BCPs)	1
1.2. Block copolymers under confinement	2
1.3. Block copolymer nano -rods and -tubes	5
1.3.1. Self assembled BCP nano-rods and -tubes	6
1.3.2. BCP Nanotubes and rods via shape defining hard templates.....	7
1.4. Wetting/Filling of alumina porous templates by polymers.....	9
1.5. Nanophase separation	12
1.6. Ring opening metathesis polymerization (ROMP).....	15
1.6.1. Block copolymer synthesis via ROMP	16
1.7. Objective and Concept	19

Section 2

Synthesis and Characterization of Semi-fluorinated Norbornene BCPs	22
2.1. Concept.....	22
2.2. Experimental	24
2.2.1. Materials and methods	24
2.2.2. <i>Synthesis of endo,exo-2.2.11 bicyclo-2-ene-5,6-dicarboxylic acid dimethylester (2) (monomer A)</i>	26
2.2.3. <i>Synthesis of endo,exo-2.2.11 bicyclo-2-ene-5,6-dicarboxylic acid-bis(3,3,4,4,5,5,6,6,7,7,8,8,8-tridecafluorooctyl) ester (3) (monomer C)</i>	27
2.2.4. <i>Synthesis of exo-N-(4,4,5,5,6,6,7,7,7-nonafluoroheptyl)-10-oxa-4-azatricyclodec-8-ene-3,5-dione (8) (monomer D)</i>	27
2.2.5. <i>Synthesis of poly(A₁₀₀)</i>	29
2.2.7. <i>Synthesis of block copolymer Poly(A_m-b-D_n)</i>	30
2.3. Results and discussion	30
2.3.1. Polymerization of A _m -b-D _n	30
2.3.2. Monitoring Crossover Efficiency via MALDI	33
2.3.3. Polymerization of A _m -b-C _n	41
2.3.4. Thermal characterization of BCPs	42
2.3.5. BCP morphology characterization.....	43
2.4. Conclusions	46

Section 3

Block copolymer Nanotubes by Melt-Infiltration of Nanoporous Aluminum Oxide.....	47
--	----

3.1. Concept.....	47
3.2. Characterization methods for bulk A_m - b - D_n	48
3.3. Preparation of A_m - b - D_n nano-tubes and rods	49
3.4. Results and Discussion	50
3.4.1. X-ray scattering and Rheology characterization of bulk A_m - b - D_n	50
3.4.2. Surface energy characterization of A_m - b - D_n	55
3.4.3. Influence of chain length on nanostructure formation.....	56
3.5.4. BCP Tube wall morphology characterization.....	59
3.6. Conclusions	62
Section 4	
Hierarchical Nanostructures via Nano-and Micro-phase Separation.....	63
4.1. Concept.....	63
4.2. Characterization methods: Structure and Chain dynamics.....	64
4.3. Results and Discussion	65
4.3.1. X-ray scattering results: Small angle and Intermediate q range.....	65
4.3.2. Dynamic mechanical analysis (DMA).....	67
4.3.3. Dielectric Relaxation Spectroscopy results	69
4.3.4. Discussion on hierarchy of length scales	76
4.3.5. Temperature dependency of nanophase separation	77
4.4. Conclusions	81
Section 5. Summary	82
6. References.....	87
7. Appendix	
CURRICULUM VITAE	
ERKLÄRUNG	

Section 1

Introduction and motivation

Present day material science has taken a lot of interest in the preparation of nanostructures in the mesoscopic range (1 – 100 nm). Self-assembly process of soft materials is one of the promising key strategies for the fabrication of such nanostructured materials. Phase separating block copolymers (BCPs) are among such self assembling materials which have fascinated material scientists in many different fields of research. These materials are developed to enhance, simplify and reduce the cost of nano-patterning process. The application of these materials covers a wide range like materials science, micro electronics, nanoreactors, molecular biology and pharmacy.¹⁻⁴

1.1. Block copolymers (BCPs)

Block copolymers are comprised of at least two chemically different and incompatible polymer chains bonded together covalently at one end. Due to the long range repulsion forces (incompatibility) the polymer chains tend to phase separate but the short range attractive forces (covalent bond) does not allow the macro phase separation. In course they undergo micro phase separation and organize into an ordered structures as they pass through the order-disorder transition (ODT).⁵ The simplest AB type amorphous di-block copolymers organize into several geometry of morphologies like spheres, cylinders, gyroid and lamellae depending upon the ratio or volume fractions (f) of the two blocks (see figure 1.1). The phase transition (ODT) is governed by χN , where N is the degree of polymerization and χ is the Flory-Huggins interaction parameter which is a function of inverse temperature (T) and written as $\chi = A/T + B$, where $A > 0$ and B are constants for the given value of f and N . Hence, ODT can be traversed by changing the temperature, T : high temperature favors the entropy of polymer chains as they randomly fill space, whereas at low temperatures the enthalpy dominates which drives the segregation of the blocks to minimize the contacts between them. ODT can also be traversed through the changes in the degree of polymerization (N) i.e. molecular weight (M_n). Increase in the molecular weight (M_n) leads to increase in the enthalpic contribution and hence ordering occurs. Figure 1.1 shows the phase diagram of di-block copolymers.

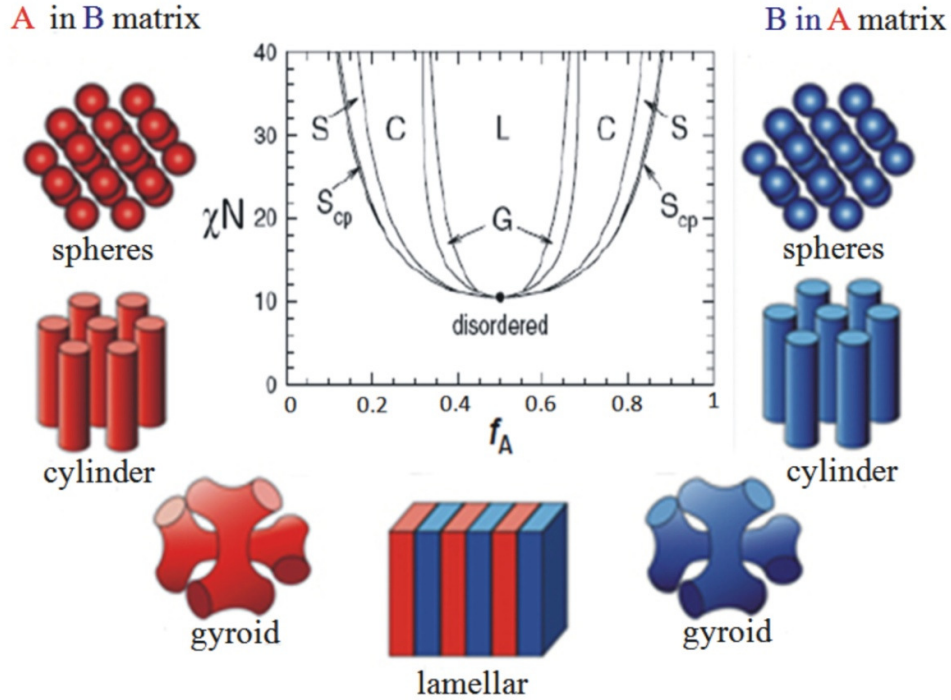


Figure 1.1. Phase diagram for diblock copolymer AB type⁶ and schematic pictures showing geometry of morphologies. Phases are labeled-L (lamellar), C (hexagonal cylinders), G (gyroid) S (bcc spheres), S_{CP} (close-packed spheres). (The phase diagram in the center is taken from reference 6).

The above stated geometry of morphologies for diblock copolymers are the equilibrium structures below ODT temperature and true only in the bulk state. Whereas when these block copolymers are subjected to certain physical confinement (1D, 2D or 3D) the reorganization of molecular arrangement can occur leading to novel morphologies which cannot be accessed in the bulk state.

1.2. Block copolymers under confinement

The fundamental principle of block copolymer microphase separation in a confined state lies in a breaking of structural symmetry and the consequence of commensurability⁷ between the repeat period of BCP and the physical dimension of the confinement. If they are incommensurate, the morphology of BCP deviate from its equilibrium due to the confinement induced structural frustration, entropy loss and surface interactions.⁸ The self assembly of symmetric and asymmetric block copolymers under one- (1D) and two-dimensional (2D) confinement, imposed by thin films or two parallel bounding surfaces

or topographically patterned substrates,⁹⁻¹⁹ has been extensively studied both theoretically²⁰ and experimentally.

1D confinement and BCP thin films : The preferential segregation of one of the blocks to the interface in BCP thin films orient the microdomains parallel to the interface resulting in multilayered film structure.^{10, 12, 13 21} In the case of symmetric BCP the same blocks segregate to both interfaces while, in the case of asymmetric BCP, different blocks segregate to the two different interfaces. Incommensurability in thin films on a solid substrate with free surface occurs when there is a mismatch between the film thickness (t) and the bulk equilibrium periods (nL_0) of the BCP. The frustration resulting from incommensurability is relieved by the formation of a surface topography consisting of terraces of step height L_0 , so that highly oriented layers can propagate throughout the entire film.^{12, 22} In symmetric BCPs the lamellae normal to the surface is obtained when the film thickness (t) is greater than the equilibrium periods (nL_0) whereas the surface-perpendicular lamellae are often formed when film thickness is less than nL_0 .²³ The former morphology satisfies the substrate boundary condition, which demands contact with the block having more favorable substrate interactions and the later morphology maximizes the conformational entropy of the chains by allowing L_0 to be expressed laterally.²³⁻²⁶ Such lateral morphologies are particularly interesting because they offer the possibility of designing chemically patterned surfaces on a nanoscale. If the energy required to accommodate the BCP chains is greater than the total interfacial energy, then the lamella will orient parallel to the surface preserving the natural period of the BCP at the expense of interfacial energy.¹²

2D confinement : If the BCP film is confined between the two solid interfaces (homogenous or heterogeneous) the surface topography formation mechanism by relieving an imposed frustration is prohibited and hence the BCP must find an alternative route to do so.^{9, 27-29} The BCP chains are accommodated in multilayers by stretching or compressing, if the interfacial interactions are strong enough. If the thickness of the confined film is changed the number of layer will change and the total amount of deformation will be distributed throughout the film, so that the extent of deformation will decrease with increasing the film thickness. Nealy and coworkers have applied two dimensional (2D) confinements to the BCPs by using the chemically or lithographically patterned substrates in addition to the film thickness to order the BCP domains either parallel or perpendicular to the substrate with precise control over dimensions.^{9, 14-18}

Cheng et al. has used the photo-lithographically created troughs to induce frustrations on a natural period of the sphere and cylindrical domain forming BCPs causing perturbation in the lateral packing of microdomains.³⁰ 1D and 2D confinement of block copolymers does not provide an opportunity to generate unusual structures; instead it is most frequently used to control the long range ordering and orientation of lamellar or cylindrical structures either normal or perpendicular to the bounding surfaces.

3D confinement: Three-dimensional (3D) confinement, for example: hard nanopores and nanospheres induce additional boundary conditions of curvature in addition to the incommensurability between the pore size and BCP repeat periods, which promotes the unusual BCP morphologies different from the bulk. In combination with interfacial interactions between the blocks of BCP and confinement walls, the preferential segregation of one component to the walls, spatial confinement and forced curvature are shown to induce transition of BCP morphology seen in bulk.

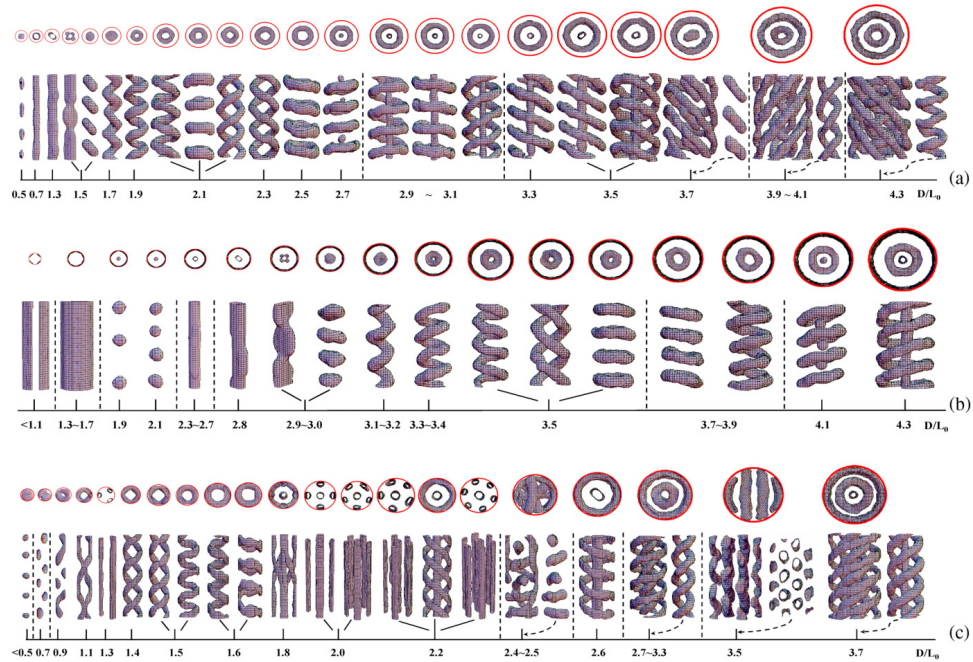


Figure 1.2. Self-assembled morphologies as a function of the ratio D/L_0 for different wall-polymer interactions. The parameter D/L_0 is given underneath each morphology. Both a top view and a side view are given. The outmost circles in the top views indicate the wall of the cylindrical pores. For some large diameters, the inner ring is shown separately. (a) The case where the wall attracts the majority blocks ($f_A = 1/6$). (b) The case where the wall attracts the minority blocks ($f_A = 1/6$). (c) The case of a neutral wall ($f_A = 1/4$). (Figure is taken from reference 34).

Extensive theoretical studies³¹⁻³⁴ have been made for both symmetric and asymmetric BCPs under cylindrical nano confinement to conclude that the type of morphology depends on the D/L_0 ratio, where D and L_0 are pore diameter and domain size respectively. Several researchers³¹⁻³³ have predicted the concentric cylindrical structures from lamella-forming BCPs under cylindrical confinement. Bin Yu et al.³⁴ predict a rich variety of novel morphologies like helices to toroids to complex networks (see figure 1.2) in cylindrical confinement with cylinder forming asymmetric BCPs using simulated annealing method.

Russel et al.³⁵⁻³⁷ and sun et al.³⁸ experimentally found the concentric ring structures, when D is larger than L_0 , with confining the PS-*b*-PBD and PS-*b*-PMMA block copolymers respectively within the ordered nanoporous alumina template. Whereas stacked-disk, toroid or helices structures^{36, 37, 39} were found when D is equal to L_0 and D/L_0 is not an integer. Recently Steinhart and coworkers⁴⁰ were able to obtain some of the theoretically predicted structures like helices, multiple helices, core shell structure and stacked doughnuts, etc. by confining polystyrene-block-poly(2-vinylpyridine) (PS-*b*-P2VP) within hard porous alumina templates. Other than creating novel BCP morphologies the cylindrical nano confinement of BCPs promotes the fabrication of nano-fibers/rods or tubular structures having internal mesoscopic fine structures formed by phase separation. Further, the selective degradation⁴¹ or selective swelling^{40, 42} of one of the blocks could convert these nanoscopic domain structures into polymeric scaffolds containing mesoporous structures and such structures can be exploited as nanoscopic containers, separation media and scaffolds for depositing inorganic materials etc.

1.3. Block copolymer nano -rods and -tubes

Nanotubes and nanorods exhibiting internal mesoscopic structures represent a new and exciting class of nanomaterials as the different parts of rods or tubes can be selectively functionalized in order to engineer the electronic, optical, chemical and mechanical properties. The fabrication of such nanostructures is technically demanding and requires special process with state-of-art technique. In general, two fundamental strategies allow the fabrication of block copolymer nanotubes and rods. The first strategy is via direct self assembly of block copolymer chains and the other strategy is via physical templating of block copolymers inside the aligned arrays of hard pores such as self ordered nanoporous aluminum oxide (AAO).

1.3.1. Self assembled BCP nano-rods and -tubes

Amphiphilic block copolymers in block selective solvents agglomerate to form nano sized aggregates called micelles.^{4, 43} Micelles are the structures with the lowest Gibbs free energy under a given set of experimental conditions. Depending on the solvent, block copolymer composition, and preparation method, the micelle-like aggregates can have various morphologies⁴⁴⁻⁴⁸. For diblock copolymer aggregates, the morphologies range from spheres⁴⁹ to cylindrical micelles^{47, 50, 51}, vesicles or bilayers^{48, 52} etc. The shape of these self assembled amphiphiles is governed by the ratio of hydrophobic part to the hydrophilic one which sets in the curvature of its interface. Block copolymers with large soluble blocks, that is, with small curvature radii form spherical micelles preferably, whereas cylindrical micelles or vesicles result from smaller soluble blocks, that is, with greater curvature radii.^{4, 53} The block copolymer nanotubes via self assembling in selective solvent was first reported by Eisenberg and coworkers^{52, 54} using polystyrene-*block*-poly(ethylene oxide) (PS-PEO) samples in DMF/water mixture.

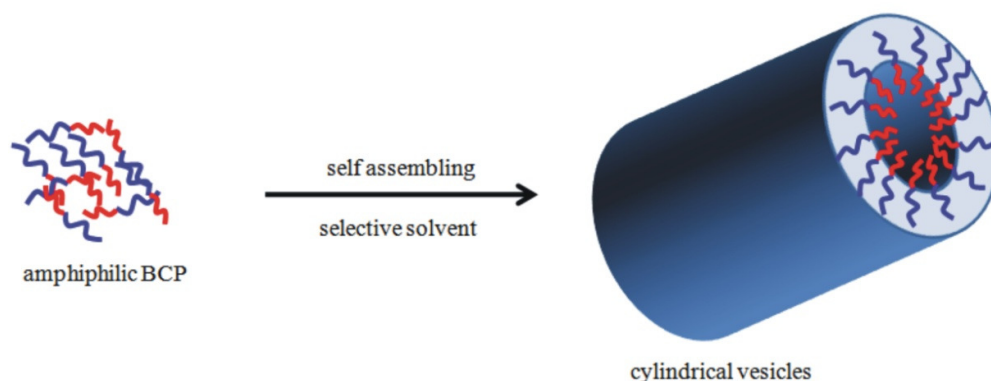


Figure 1.3. Schematic illustrations showing the formation of tubular vesicles from amphiphilic block copolymer in a block selective solvent.

crystalline-coil poly(ferrocenyldimethylsilane)-*block*-poly(dimethyl siloxane) or PFS-PDMS diblock copolymers were reported by Ruez, Manners, and Winnik⁵⁵ to form nanotubes readily in block-selective solvents hexane and *n*-decane, which solubilized the rubbery PDMS blocks and not the crystalline PFS blocks. The first ABC triblock copolymer used to prepare nanotubes was polyisoprene-*block*-poly(2-cinnamoyloxyethyl methacrylate)-*block*-poly(*tert*butylacrylate) or PI-PCEMA-PtBA.⁵⁶ Nanotube preparation involved dispersing the triblock in methanol (MeOH). Since only the PtBA block is soluble in MeOH, the triblock copolymer self-assemble into cylindrical aggregates

consisting of a PtBA corona and a PI core encapsulated by an insoluble PCEMA intermediate layer. The aggregates in MeOH are then subjected to UV light irradiation to cross-link the PCEMA pendant double bonds via 1,4-cycloaddition. Nanotubes with hollow centers can be obtained after the degradation of the PI core by ozonolysis and fragment extraction using a solvent. See figure 1.4 for schematic illustration.

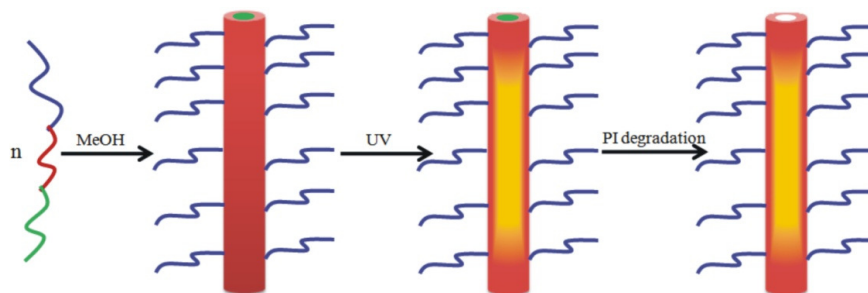


Figure 1.4. Schematic diagram showing the steps involved in preparing nanotubes from PI-PCEMA-PtBA.

The alternative method for the fabrication of nanotubes and rods is by using self assembled block copolymers as solid precursors.⁵⁷ In this context, self-assembled di- or tri- block copolymers to hexagonal cylindrical morphology in which the cylinders forming block containing the photo-crosslinkable moieties have been used.^{56, 58-60} Photo-crosslinkable block allows fixing the structure by cross-linking and later the fibers and tubes can be sculptured via selective dissolution or degradation of matrix or core. The advantages of this method lie in the straightforward bulk phases of BCP, instead of more complicated solvent phases. However it is limited only to photo-crosslinkable polymers. The detail discussion and more examples of block copolymer self assembled nanotubes and rods are discussed elsewhere.⁶¹ Hybrid organic inorganic rods have been prepared by combined process of sol-gel reaction of aluminosilicates together with self-assembling of poly(ethylene oxide)-block-poly(isoprene).⁵⁷ The jet electro spinning of BCP solution have been also used to prepare the BCP nano-rod and tubular structures.⁶²

1.3.2. BCP Nanotubes and rods via shape defining hard templates

The infiltration of shape-defining hard templates containing arrays of cylindrical nanopores, such as self-ordered nanoporous anodic aluminum oxide (AAO)^{63, 64} with organic supramolecules is a well-established synthetic approach to prepare one-dimensional (1D) nanostructures.⁶⁵ For infiltration of polymeric materials, an AAO

template is brought in contact with either a polymeric melt or a polymer solution and subsequently driven into the pores by capillary forces^{37, 66} or wall wetting process^{67, 68}. Subsequent removal of the template releases the nanoinfiltrate, generating polymer rods or tubes in the dimensions of the initial template-structure.

1.3.2.1. Wetting Phenomena

To understand the wetting of polymer melts on alumina surface, it is necessary to understand the wetting phenomena of low molar mass liquids on flat substrates. Wetting can be defined as the phenomena resulting in the creation of a solid-liquid interface, when two phases, one solid and the other liquid, are in contact. A liquid drop on a solid surface is shown in figure 1.5.

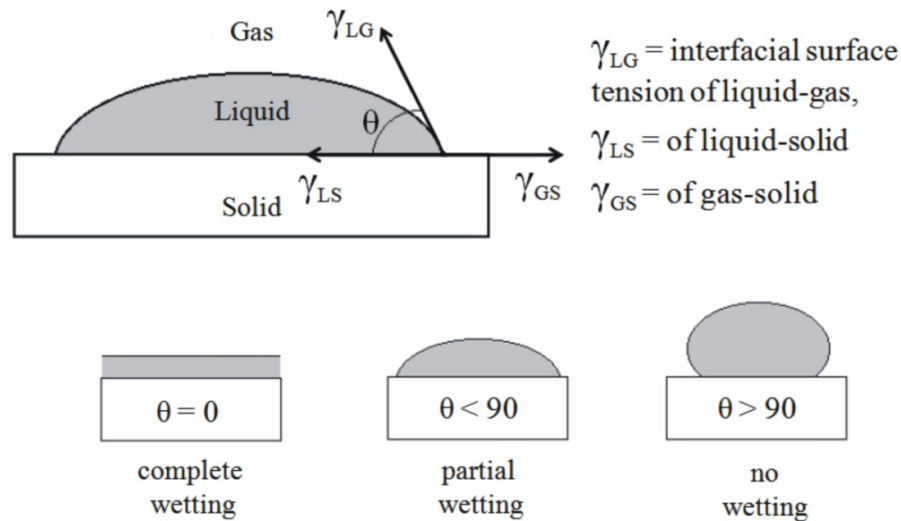


Figure 1.5. Schematic diagram of liquid droplet on the solid substrate with force balance in three phase contact line and the three situations of wetting.

The spreading of a liquid on a solid surface placed in a gas provokes the displacement of this gas: the original interface (gas/solid) disappears and is replaced by the new area of interface liquid/gas.⁶⁹⁻⁷¹ In this process, it is the variation of free surface energy that plays the determining role. The free surface energy (γ_{GS}) is defined as the reversible work done in creating unit area of fresh, flat, free surface and it plays an important role in interfacial interactions with other materials. Estimation of surface energy can be obtained from measurement of the contact angle of a liquid drop on the solid surface and using the *Young's equation*. Ideally, if we only take into account the surface energy and if no other

frictional forces are involved, the spreading will take place spontaneously in the direction of a reduction of the free energy of the total surface. The shape taken by the drop on the solid is therefore characteristic of the interactions between the liquid, the solid and the gas. Wetting is thus characterized by a contact angle (θ) representing the degree of spreading of the drop. The contact angle (θ) can vary between 0° and 180° , and conventionally three situations are schematized in the figure 1.5. Young first proposed a thermodynamic equation for the relationship between the equilibrium contact angle of a liquid drop on a solid surface and the equilibrium of forces.

$$\gamma_{GS} = \gamma_{LS} + \gamma_{LG} \cdot \cos \theta \quad \text{-----Youngs equation}$$

This equation can be written as

$$\cos \theta = \frac{\gamma_{GS} - \gamma_{LS}}{\gamma_{LG}}$$

It is now easy to understand that:

- Low surface tension of the liquid drop leads to an increase of $\cos \theta$, and thus the decrease in contact angle (θ).
- Solids, with low surface energies, will be more difficult to wet, γ_{GS} being weak, $\cos \theta$ is small and consequently the contact angle (θ) is big.

Normally the high energy solids such as glass, metals, ionic crystals and inorganic substrates characterized by high bonding energy are wettable by almost all organic liquids.⁷⁰ The viscous liquids like polymer melts and solutions normally have low surface energy and wet the substrates with high surface energy⁶⁸ forming a precursor film of few tens of nanometer thick spontaneously and later complete spreading takes place over the substrate with infinite time (figure 1.6).



Figure 1.6. Spreading droplet with a precursor film.

1.4. Wetting/Filling of alumina porous templates by polymers

Organic polymers generally have surface energies one order to several orders of magnitude smaller than those of hydroxyl-terminated inorganic oxides such as alumina.⁷⁰

Thus, organic polymers spread on inorganic oxide surfaces such as the pore walls of AAO to form a precursor film. Infiltration of organic polymers into AAO is, therefore, a spontaneous process. If the formation of a precursor film is suppressed by any kind of infiltration condition or by material property itself, the filling of pore volume is governed by capillary forces.⁷² The strong adhesive forces between the polymer and the pore walls are still effective but are not strong enough to drive single molecules out of the polymeric bulk reservoir on top of the hard template. However, removing single molecules from the bulk is a prerequisite for the rapid formation of a precursor film. In capillary filling a solid thread of viscous polymer, preceded by meniscus, slowly moves into the pores of the hard template to fill the pore volume completely to yield nanorods. Hence, wall wetting and capillary filling of the pores take place on different time scales. The stable precursor film formed on AAO pore wall by a polymer melt or a solution has to be solidified, by cooling or solvent evaporation respectively, to get the tubular structures. Otherwise, after an infinite long time the more polymer flows into the pore or the menisci across the pores at local instabilities develops in the precursor film⁷³ similar to the low viscous liquids in pores.^{69, 74, 75} As the more liquid flows into the menisci, their surfaces move in the opposite directions until the equilibrium is attained that is complete filling of pore volume to yield rods. The schematic of melt infiltration of AAO porous template with polymer melt leading to tubes and rods are shown in figure 1.7.

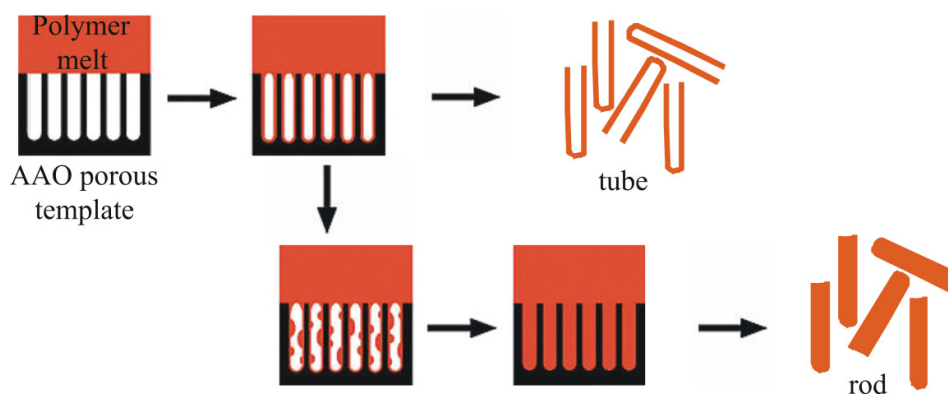


Figure 1.7. Schematic of melt infiltration of polymer into AAO porous template forming tubes via precursor film formation and rods by complete filling.

Precursor wetting and capillary wetting represent only different kinetic routes to attain equilibrium that is characterized by complete filling of the pores with the polymer melt. Complete filling (leading to rods) or partial filling (generating nanotubes) has been

observed for homopolymers such as poly(styrene) (PS),⁶⁷ poly(methylmethacrylate) (PMMA),^{67, 72} poly(ethyleneoxide) (PEO), poly(vinylidene fluoride) (PVDF)⁷⁶ and poly(vinylalcohol) (PVA).⁷⁷ In case of homopolymer melt infiltration, the transition from wall wetting (tubes) to capillary filling (rods) has been observed upon increase in temperature, change in molecular weight or pore size (D_p).^{72, 77}

Since nanotubes might be exploited as nanoscopic containers, micro-pipelines or separation media, it is highly desirable to fabricate tubular nanostructures, the walls of which consist of microphase-separated BCPs. Hence, potential functionalities of nanotubes and of BCPs could be combined. For example, nanotubes with walls composed of multiple concentric layers having different properties could be accessible in this way. BCP nanotubes inside nanoporous hard templates have been produced by infiltration of BCP solutions.^{78, 79} However, adsorption kinetics depends on a multitude of parameters including temperature and thermodynamic quality of the solvent. Moreover, the evaporation of the solvent inevitable for solidification of the BCP is a non-equilibrium process difficult to control in a satisfactory manner, which may involve additional migration of polymer from the supernatant solution into the pores, separation into solvent-rich and polymer-rich phases, occurrence of hydrodynamic instabilities and surface reconstruction processes, as well as uncontrolled development of ill-defined gradient structures. The generation of specific functionalities requires control over mesoscopic structure formation processes occurring in the confined geometry of nanotube walls, such as crystallization and phase separation and thus wetting the hard pore walls by BCP melt and subsequent rate of cooling can gain control over such structure formation. While infiltration of BCP melts into the cylindrical pores has always yielded only solid nanorods^{80, 81} via capillary filling as it is difficult for the polymer chains to come out of the ordered and microphase separated BCP melt to form a precursor film via wall wetting.

Key to the formation of BCP nanotubes having walls with nanoscopic domain structures is the capability of the microphase-separated BCPs to form mesoscopic precursor films on the pore walls and the possibility to quench infiltration at this stage, as reported previously for homopolymers. The development of precursor films should reduce the overall surface energy of the system but this process is accompanied by the formation of a new polymer/air interface. Henceforth it is reasonable to assume that the surface energy of the new polymer/air interface is among the parameters determining whether or

not precursor films occur. Hence, minimizing this newly formed polymer/air interfacial surface energy is a promising strategy to induce the formation of precursor films. Therefore, the part of this thesis work is focused on synthesizing block copolymers with low surface energy with one of the block having a strong tendency to segregate to the BCP/air interface and further melt infiltration into the nanoporous alumina template to form precursor film generating the BCP nanotubes with internal mesoscopic fine structures. To this end, we have synthesized the norbornene and oxy-norbornene block copolymers with fluorinated alkyl sides via ring opening metathesis polymerization (ROMP). It is well known that fluorinated homopolymers and BCPs have outstandingly low surface energies.^{82, 83} In thin-film configurations, fluorinated blocks of BCPs show a strong tendency to segregate to the BCP/air interface.⁸⁴ For example, the poly(methyl methacrylate) blocks of a model BCP studied by Al-Hussein et al.⁸⁵ segregated to the hydroxyl-terminated substrate, whereas poly(acrylate) blocks bearing semi-fluorinated alkyl side chains segregated to the film/air interface.

1.5. Nanophase separation

The microphase separation in block copolymer systems due to the block incompatibility and its structure formation (typical domain size $> 10 - 100\text{nm}$) has been extensively studied and well established. In contrast nanophase separation, a phenomenon occurring in the side chain polymers due to phase segregation of incompatible side chains (alkyl-C > 4) from the main polymer chain to form nano-domains (size $d_{\text{nps}} \sim 0.5 - 5 \text{ nm}$),^{86, 87} has been a interest among material scientist's in recent years. These nano-domains have a typical dimension of $0.5 - 5 \text{ nm}$ and the formation of such nano-domains in small and large molecules have been reported in past by several researchers.^{86, 88-90} The nanophase separation of side chains is characterized by the X-ray scattering experiments normally in the scattering vector (q) range of $0.2 \leq q \leq 0.6 \text{ \AA}^{-1}$ and the appearance of a 'prepeak' in the intermediated q range support the nano-domain picture. Beiner et. al.⁹¹ have characterized such alkyl nanodomains in poly(n-alkyl acrylates) (PnAA) and poly(n-alkyl methacrylates) (PnAMA). The alkyl nano-domain size (d_{nps}) i.e. the main chain to main chain distance in PnAA and PnAMA depends on the side chain length. It has been shown that the scattering prepeak maxima, for PnAA and PnAMA having different alkyl side chain length ($C = 1-10$), shifts to lower q (larger domain size) with increasing side chain length. The one dimensional and three-dimensional schematic view for amorphous side chain polymers is shown in figure 1.8, depicting the aggregation of alkyl side chains

from different monomeric units belonging to one or different polymer chains. The scattering experiments performed for other alkyl side chain containing polymers like poly(di-n-alkyl itaconates)⁹², hairy rod polyimides⁹³, poly(alkylbenzimidazol-*alt*-thiophene)⁹⁴, and poly(3-alkyl thiophenes)⁹⁵ are in agreement with results of poly(n-alkyl acrylates). This shows that the nanophase separation occurs in several polymer series having alkyl side chains and that the nano-domain size mainly dependent on the number of alkyl carbon atoms per side chain. Arbe and co-workers⁹⁶ have exploited the selectivity of neutron scattering combined with isotopic substitution to study the nanophase separation of series of poly(n-alkyl methacrylates) by labeling the side chains and main chains by deuteration. Results from selective neutron scattering gives additional evidence for alkyl nano-domains in side chain polymers and supports the X-ray scattering data. The diffraction peak originating from the side chains is absent in case of sample deuterated only along the main chain indicating the nano ordering of alky side chains.

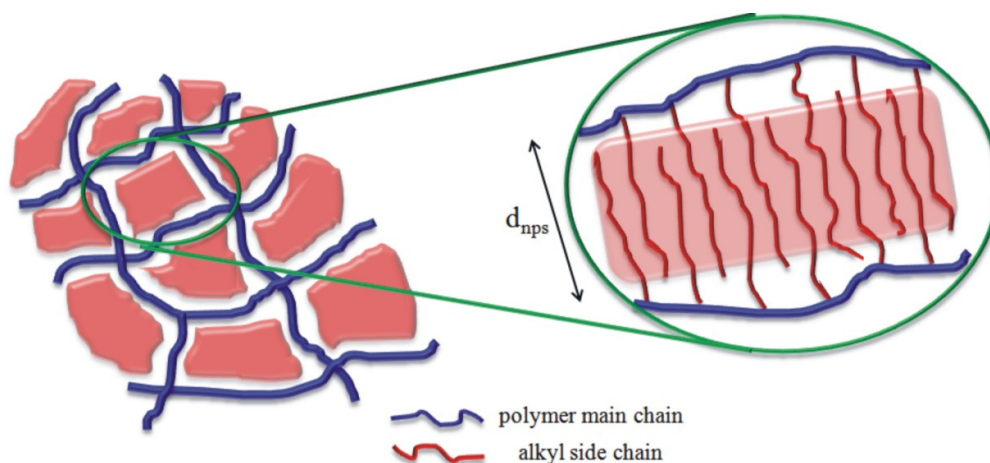


Figure 1.8. Schematic picture illustrating the alkyl nanodomains formed by nanophase separation of alkyl side chain from main polymer chain.

Considering the dynamic heterogeneity picture, a phase separated system shows varied cooperative dynamics and relaxation behavior,⁹⁷ whereas in a miscible blend the dynamic glass transition merges together indicating uniform phase picture. Hence, the nanophase separation in amorphous side chain polymers can be traced by studying the dynamics or relaxation behavior of side chains and main chains using dynamic mechanical analysis (dynamic shear measurements) or dielectric relaxation spectroscopy for the polymers containing an active dipole moment. It has been shown⁸⁶ for PnAMAs

that there are two coexisting independent relaxation processes having typical features of a primary relaxation process (α) or dynamic glass transition. A polyethylene (PE)-like glass transition (α_{PE}) is observed at low temperatures besides the conventional glass transition (α) of the main chain at higher temperature in shear measurements. This implies that an independent cooperative process (α_{PE}) occurs within small alkyl nanodomains formed by nanophase separation of incompatible alkyl side chains from the main polymer chain. In these shear data the intensity of the α_{PE} process increases systematically with the volume fraction of alkyl side chains, whereas the conventional glass transition (α) shifts to lower temperature with increase in side chain length due to the internal plasticization effect caused by flexible side chains. Similar trend has been noticed in the series of poly(3-alkyl thiophenes).⁹⁵

The side chain dynamic and relaxation behavior has been characterized for PnAMA series^{86, 91} using broad band dielectric relaxation spectroscopy and the dielectric data show that the α_{PE} process is localized within the alkyl side chains and the results are comparable with shear data. The α_{PE} process in PnAMA contributes a weak dielectric signal due to the fact that the dipole moment is located in the carboxyl group close to the backbone. Dielectric spectroscopy has been successfully employed to study the molecular dynamics in semifluorinated-side chain containing polysulfone (PSU)^{84, 98, 99}, polyesters,^{100, 101} and polystyrenes.¹⁰¹ The fluorinated side chains have highly active dipoles and hence the side chain dynamics can be traced independent of the polymer backbone chain. The long alkyl side chains ($C \geq 10$) undergo crystallization and also some side chains exhibit liquid crystalline behavior. The details of side chain crystallization and side chain liquid crystals are reported and discussed elsewhere.^{95, 102, 103 85, 90, 104} Recently a lot of attention and research has been devoted to the preparation of hierarchical nanostructures but it still remains a great challenge to find a general and simple synthetic process for the formation of hierarchical nanostructures with well-controlled shape, size, and composition at different levels. The self assembling in soft matters has been used to a greater extent to this end in combination with other techniques like lithography. However, the quest to search for a simple and cheaper process is still on; in this regard it is desirable to combine the incompatibility driven microphase separation in block copolymers with the nanophase separation of side chains to obtain the nanoscopic domains ($d = 0.5 - 5\text{nm}$) of side chains as second hierarchical structure level within the microphase separated block copolymer domains ($d > 10 - 100\text{nm}$).

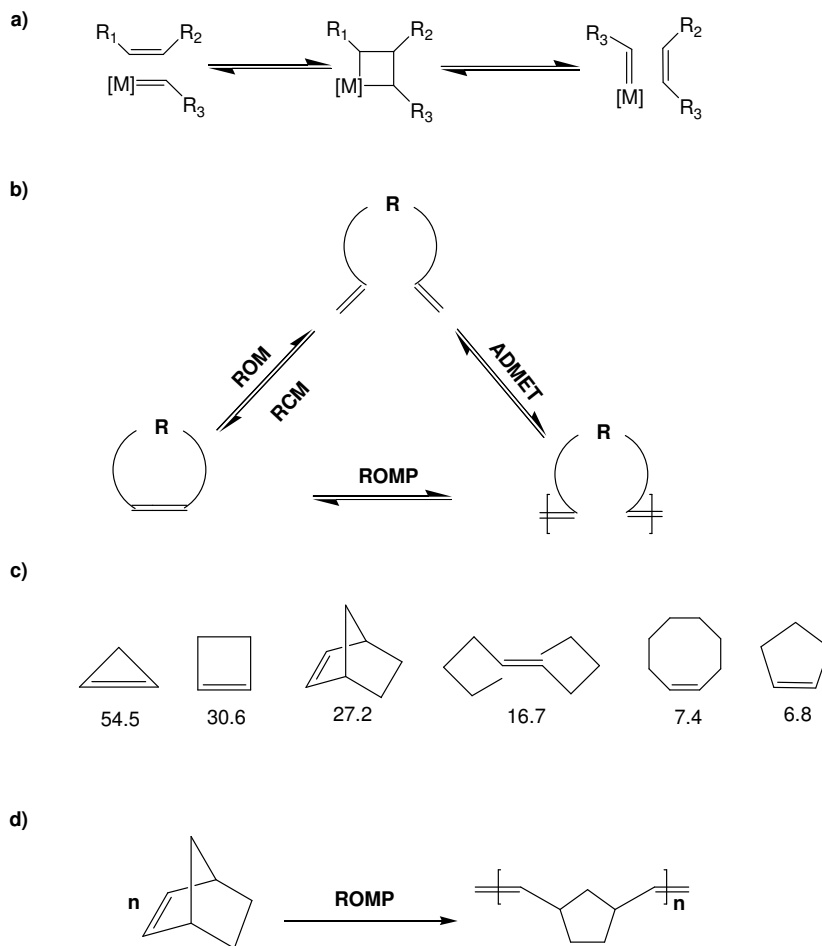
1.6. Ring opening metathesis polymerization (ROMP)

Synthesis of block copolymers demands the controlled or living polymerization reaction as the different monomers are polymerized sequentially one after the other. Anionic polymerization, reversible addition-fragmentation chain transfer radical polymerization (RAFT), atom transfer radical polymerization (ATRP) and ring opening polymerization (ROMP) are some of the living polymerization techniques, been used in synthesizing the variety of block copolymers with controlled architectures.¹⁰⁵⁻¹⁰⁷

Living ROMP has emerged as a powerful technique and employed in the synthesis of functionalized homopolymers and block copolymers of cyclic olefins having interesting properties (electronic, optical, biological and mechanical properties).¹⁰⁸ The ROMP mechanism is based on the olefin metathesis reaction, which is a metal mediated carbon-carbon double bond exchange process.¹⁰⁹ The mechanism of metathesis reaction proposed by Chauvin is shown in the Scheme 1.1a. Cross metathesis (CM), ring closing metathesis (RCM), ring opening cross metathesis (ROCM), ring opening metathesis polymerization (ROMP) and acyclic diene metathesis polymerization (ADMET) are the most prominent members of olefin metathesis family.¹¹⁰ The Nobel Prize (2005) in chemistry was awarded to Yves Chauvin, Robert H. Grubbs and Richard R. Schrock for their contributions in the development of olefin metathesis chemistry.^{109, 111, 112}

The cyclic olefins like cyclopropene, cyclobutene, cyclopentene, cyclooctene and norbornene (see scheme 1.1c)¹¹³ which possess a considerable degree of ring strain (>5kcal/mol) are the commonly used monomers in ROMP. Cyclohexene with a low ring strain is an exception for ROMP. The ROMP of cyclic olefin monomers is initiated by transition metal carbene catalyst and the initiation starts with coordination of a transition metal alkylidene complex to a cyclic olefin and subsequently undergoes [2+2] cycloaddition to form four member metallacyclobutane intermediate. Further the cycloreversion of this intermediate gives new metal alkylidene complex containing a monomer unit. The newly formed complex has the same reactivity of initial catalyst towards the monomers. Further the polymerization propagates in similar fashion until all the monomer is consumed or equilibrium is reached or reaction is terminated by adding quenching reagents or the second monomer can be introduced into the reaction to proceed with the copolymerization in order to obtain the block copolymer (BCP). Although the ROMP reactions are reversible they are equilibrium controlled, hence there

is a chance of secondary metathesis reactions like chain transfer or backbiting leading to poly-dispersed or cyclic polymers.¹⁰⁸



Scheme 1.1. Schematic of a) olefin metathesis mechanism according to Chauvin's model, b) family of metathesis reactions, c) different ROMP monomers (cyclic olefins) with their relative ring strain (kcal/mol), d) ROMP of norbornene.

1.6.1. Block copolymer synthesis via ROMP

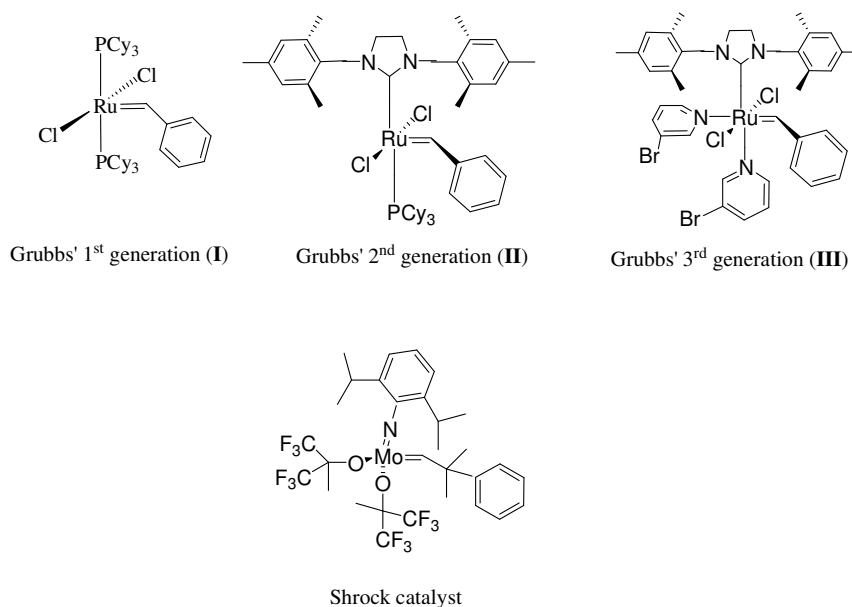
ROMP reaction, initiated with new generation ruthenium or molybdenum based catalysts, are considered to be a living polymerization reaction according to the classical rules for a living polymerization as the livingness of the reaction is characterized by low polydispersity index (PDI <1.2) and linear relationship between polymer molecular weight and monomer conversion.^{113, 114} Hence, ROMP can be employed to synthesize the block copolymers.

Block copolymers can be synthesized via ROMP by sequential addition of different monomers one after the other i.e. the 1st monomer is polymerized until all the monomer has been consumed and further addition of 2nd monomer results in a continued polymerization of 2nd monomer onto the already polymerized chain with the retained active catalyst species on the polymer chain end due to the absence or insignificant termination reactions. The continued polymerization after the addition of the 2nd monomer (i.e. cross-over reaction) is only possible when the catalyst species on the already polymerized 1st polymer chain is active or living.

The achievement of a successful block-copolymerization of monomers via living ROMP is linked to critical parameters such as (a) the optimization of the optimal monomer/catalyst combination, (b) the maintenance of livingness of the active species throughout the polymerization reaction; (c) avoiding backbiting-reactions, thus reducing the loss of already polymerized monomers from the chains in the form of cycles (d) achieving faster initiation in relation to propagation (i.e.: $k_i > k_p$) and secondary metathesis reaction (k_s), (e) avoiding chain transfer-reactions and (f) efficient crossover reaction. In particular the quest of an appropriate monomer/catalyst combination often proves difficult as even structurally related monomers often cannot be polymerized equally well with the same type of catalyst, thus leading to poor polymerization and crossover reaction with broader polydispersities and less defined molecular weights. With the advent of Grubbs (Ru based) and Shrock (Mo based) type catalyst^{108, 111, 112} a set of relatively stable, commercially available and kinetically highly diverse catalytic systems having resistance towards variety of functional groups has become available. Scheme 1.2 shows the structures of Grubbs and Shrock type catalysts. These catalysts have been successfully used for the synthesis of variety of di- and tri-block copolymers using cyclic olefin monomers.

Norbornene ring exhibits the characteristic high ring strain needed for irreversible ($k_p \gg k_s$) ROMP (scheme 1.1c) and hence polymerize well with fast initiating ($k_i/k_p \geq 1$) Grubbs 1st and 3rd generation catalysts to produce polymers with low PDIs and controlled molecular weight.¹¹⁵ Secondary metathesis is limited by steric hindrance of the olefins in the backbone of substituted polynorbornenes.¹¹⁵ Hence, norbornene and its functionalized derivatives including fluorinated norbornenes^{116, 117} have become the monomers of choice for living ROMP and also their general ease of synthesis and functionalization. Hence in this work the functionalized (semi fluorinated) norbornene

and oxy-norbornene monomers were synthesized and employed ROMP for synthesizing the block copolymers further used to melt infiltrate into the nanoporous template. Also the formation of hierarchical structures via nanophase separation⁹¹ of the long semi fluorinated side chains from the microphase separated main chain was studied.



Scheme 1.2. Structures of Grubbs and Shrock type catalyst used for metathesis reactions

The other alternative methods for preparing the block copolymers involving ROMP are coupling reaction,¹¹⁸⁻¹²¹ transformation of propagating species¹²²⁻¹²⁴ and by application of bimetallic initiators.¹²⁵ Coupling reaction involves the coupling of a ROMP polymer with another polymer chain synthesized by different living polymerization technique via Wittig-like coupling or by hydrogen bonding. Transformation of ROMP polymer chain end into an initiator for a different type of polymerization allows the synthesis of block copolymers. Transformation can be from ROMP to Ziegler-Natta polymerization or GTP or ATRP or anionic polymerization. Application of bimetallic initiator in polymerization allows the simultaneous growth of the polymer chains from both ends of initiator. Synthesis of ABA triblock copolymers via two step ROMP using bimetallic ruthenium initiators, which is living at both chain ends, has been reported.

1.7. Objective and Concept

The main objective of this work was to prepare the polymer nanotubes with differently functionalized inner and outer surface. In this regard, the microphase separating block copolymers to be melt-infiltrated into a self ordered nano-porous hard aluminum oxide (AAO) template. Formation of BCP nanotubes with one of the block segregating to outer and the other to inner surface is feasible only by preferential wetting of the pore walls by BCP melt to form a precursor films and the possibility to quench the infiltrate at this stage, as reported previously for homopolymers.^{67, 79} While, the melt infiltration of block copolymer into cylindrical pores has always yielded solid nanorods^{37, 38} via capillary filling and this is the challenge we have to overcome. The development of precursor film on the pore walls is accompanied by replacement of wall/air interface by a new polymer/air interface to reduce overall surface energy. Hence, minimizing this newly formed polymer/air interfacial surface energy would be the driving force behind the formation of precursor film. To realize this, it was necessary to synthesize the block copolymers having low surface energy with one of the block preferentially segregating to the polymer/air interface and the other to the AAO pore wall. From literature we know that fluorinated polymers have outstandingly low surface energies and the fluorinated chains show strong tendency to segregate to the polymer/air interface.^{84, 85, 126-130}

Hence, in order to accomplish our objective we have to synthesize the functionalized (COOCH₃) norbornene and semifluorinated oxy-norbornene monomers according to the literatures^{131, 132} to block copolymerize via ring opening metathesis polymerization (ROMP). The section 2 in this thesis describes the detailed synthesis and characterization of monomers and block copolymers. It includes the through study on kinetics and cross-over reactions of block copolymerization using GPC, ¹H-NMR and MALDI-TOF mass spectrometry methods.

Further, to evaluate whether microphase-separated BCPs containing one fluorinated block form precursor films in AAO pores that can be solidified to yield BCP nanotubes, we have to melt infiltrate it into the self ordered porous AAO templates. In section 3 of this report we discuss the melt infiltration of fluorinated BCPs in to AAO templates to form nanotubes. Melt drop and contact angle measurements of BCP thin films were performed to confirm the low surface energy and hydrophobic surface caused due to the segregation of fluorinated chains to polymer/air interface. BCP infiltrate structures (tubes and rods) were characterized via electron microscopy (SEM and TEM).

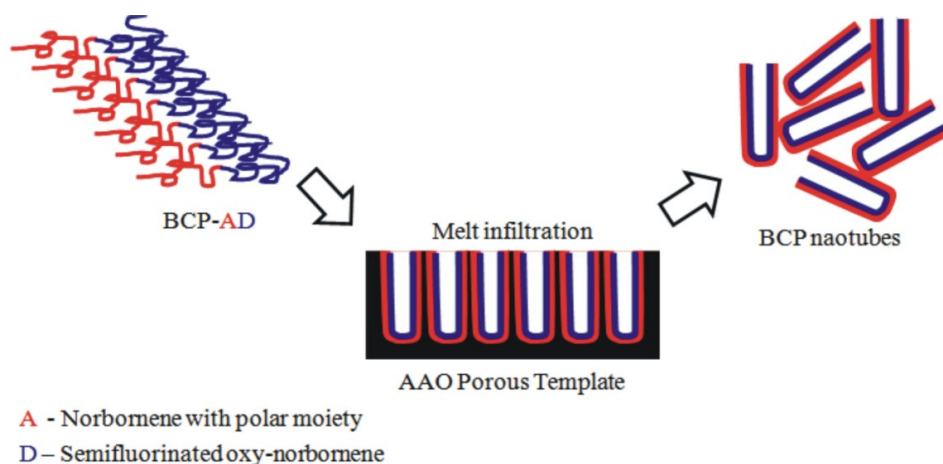


Figure 1.9. Schematic illustration of preparing polymer nanotubes having different inner and outer surface functionalities by melt infiltration of microphase separated BCP into AAO porous template to form precursor film on pore walls via wall wetting.

Many polymers with semi-fluorinated (SF) side chains have been investigated previously. Hydrocarbon main chain of polymers and fluorocarbon side chains are thermodynamically not miscible with each other. Such compounds are characterized by strong nanophase separation, if the number of C atoms in the SF segments is above a critical value, resulting in the formation of typically layerlike, well-organized, solid-state structures.^{85, 127, 133-135} Combination of microphase separation in block copolymers and aggregation of side chains via nano phase separation from main chains can be seen as a promising key strategy to prepare well defined layered nanostructures with different hierarchical levels.

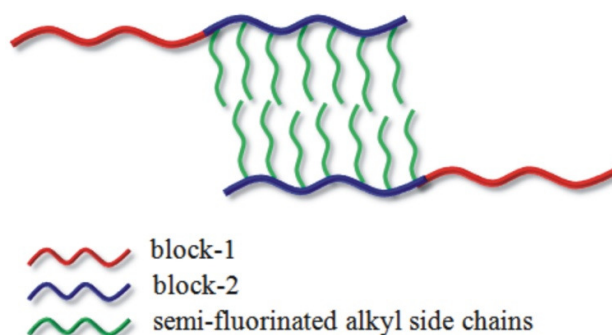


Figure 1.10. Schematic picture showing the microphase separating symmetric BCP with one of the block containing semi-fluorinated alkyl side chains which phase separate from the main polymer chain.

In this context it was essential to synthesis a block copolymer with one of the block containing long fluorinated alkyl side chains and hence the norbornene block copolymer

in which one of the block bearing long fluorinated alkyl side chains ($\text{COOCH}_2\text{CH}_2(\text{CF}_2)_5\text{CF}_3$) were synthesized as described in the synthesis part of section 2.

In section 4 we focus on the characterization of micro- and nano-phase separation of main chains and side chains. X-ray scattering technique was employed for structural characterization of nanoscopic domains within the mesoscopic domains. Main chain independent dynamics and relaxation of nanophase separated side chains were probed via dynamic mechanical analysis (DMA) and dielectric relaxation spectroscopy as a proof for phase separated side chain nano domains in prepared block copolymer.

Section 2

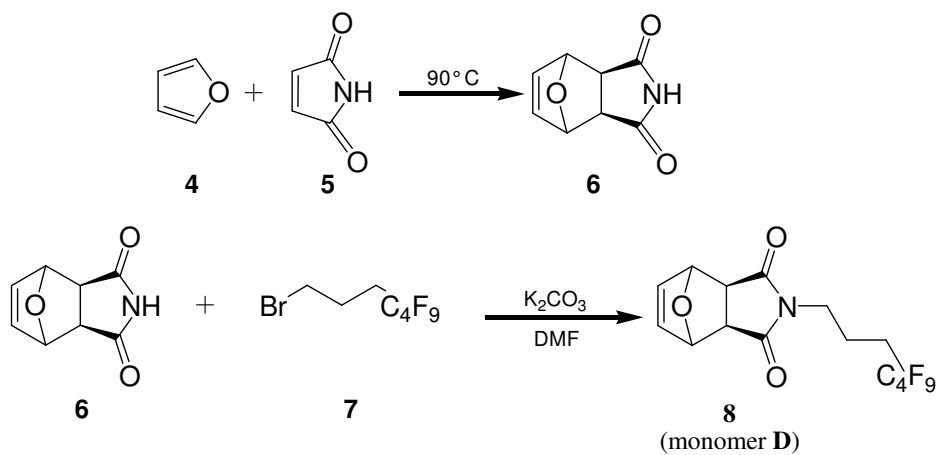
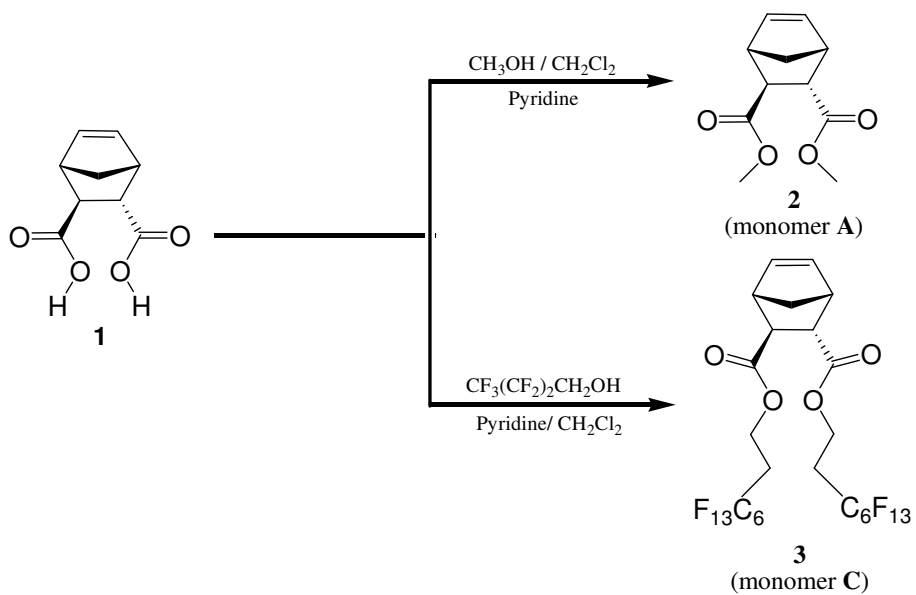
Synthesis and Characterization of Semi-fluorinated Norbornene BCPs

2.1. Concept

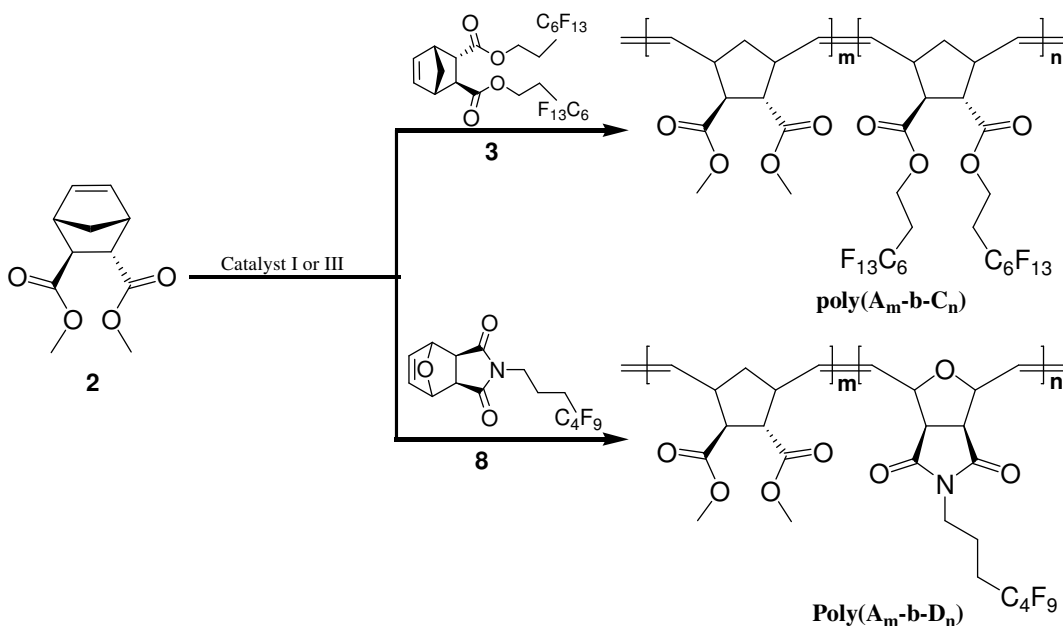
The aim was to synthesize the norbornene block copolymers with one of the block having semi-fluorinated side chains in order to obtain a low surface energy BCP. The successful block copolymerization of functionalized norbornene monomers via ROMP needs a high purity of monomers, optimal monomer/catalyst combination to maintain the livingness of the active species throughout the polymerization reaction, efficient crossover reaction from first monomer to the second monomer and optimal reaction times. Therefore three different norbornene monomers, endo,exo[2.2.1] bicyclo-2-ene-5,6-dicarboxylic acid dimethylester (2) (monomer **A**), endo,exo[2.2.1] bicyclo-2-ene-5,6-dicarboxylic acid-bis(3,3,4,4,5,5,6,6,7,7,8,8,8-tridecafluorooctyl) ester (3) (monomer **C**) and exo-N-(4,4,5,5,6,6,7,7,7-nonafluoroheptyl)-10-oxa-4-azatricyclodec-8-ene-3,5-dione (8) (monomer **D**) were synthesized according to the modified literature synthesis.^{131, 132} Monomer **A** contains two methyl ester groups (COOCH₃) and the monomer **C** contains two semi-fluorinated alkyl ester (COOCH₂CH₂(CF₂)₅CF₃) side chains. Monomer **D** is based on oxy-norbornene containing one perfluoroalkyl-maleimide-moiety (scheme 2.1). A thorough study of the homo and block copolymerization kinetics and cross-over reactions of **A** to **C** and **A** to **D** with different generations of Grubbs catalyst systems were conducted by GPC, ¹H-NMR and MALDI mass spectrometric methods to find the optimal monomer/catalyst combination with appropriate reaction time and conditions. Further the two different block copolymers, poly(**A**_m-b-**C**_n) and poly(**A**_m-b-**D**_n) with different block compositions were synthesized by the sequential addition of respective monomers by employing the suitable catalyst and procedure. The micro-ordered structures of these block copolymers were analyzed via small angle X-ray scattering (SAXS) and transmission electron microscopy (TEM). The low surface energy block copolymer poly(**A**_m-b-**D**_n) was used for the melt infiltration into nanoporous AAO template (see section 3) and poly(**A**_m-b-**C**_n) with longer fluorinated sides chains was used to study the nanophase separation of side chain from the main polymer chain (see section 4).

Synthetic Concept

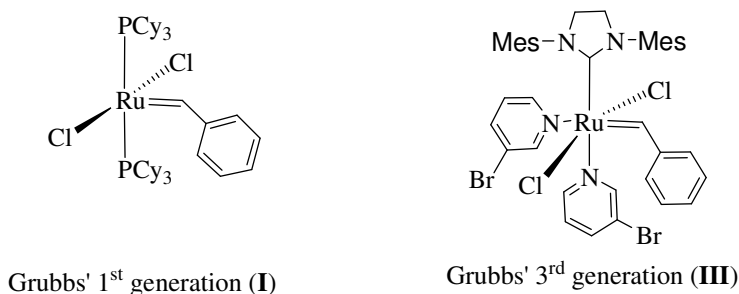
a) Monomer Synthesis:



b) Block copolymer Synthesis:



c) Catalyst:



Scheme 2.1. synthetic pathway for a) monomer synthesis; b) block copolymer synthesis and c) Grubbs catalyst structures.

2.2. Experimental

2.2.1. Materials and methods

Grubbs 1st and 3rd generation catalysts were obtained from Sigma-Aldrich. Dichloromethane (CH_2Cl_2) and dimethylformamide (DMF) were freshly distilled over CaH_2 and degassed with argon prior to use. The other solvents like petrolether, ethyl acetate and n-hexane were used after distillation. All other reagents were purchased from Sigma Aldrich (Germany) and were used without further purification.

Nuclear-magnetic-resonance ^1H NMR : The chemical structures of synthesized monomers and polymers were characterized via ^1H NMR, performed on a Varian Gemini

200 or 400 MHz FT-NMR spectrometer with MestRec (4.9.9.9) for data interpretation. The ^1H NMR was also employed for the kinetic experiments. For kinetic measurements, a pyrene stock solution was prepared from 70 mg of pyrene dissolved in 2 mL of CDCl_3 . The NMR-tube was filled with the first monomer (i.e.: monomer **A**, 17 mg) dissolved in CDCl_3 (0.2 mL) and pyrene stock solution (0.2 mL). Before adding the initiator solution, the ratio of the monomer to the internal standard was determined by NMR. Based on this value the monomer concentration at $t = 0$ was determined. A solution of the initiator in CDCl_3 , ($[\text{c}] \sim 3.3$ mg in 0.2 mL of CDCl_3) was added via a syringe to yield the desired monomer to initiator ratio. After shaking the NMR-tube was inserted into the NMR-spectrometer and the decrease of the monomer concentration with time was monitored. The second monomer (i.e.: monomer **D**, 33 mg) dissolved in CDCl_3 (0.2 mL) was added after complete conversion of the first monomer. For determination of the monomer concentration at $t = 0$ and the monomer consumption, the corresponding signals were integrated: for monomer **A** the signals at 6.27 and 6.07 ppm (2H) and for monomer **D** the signal at 6.50 ppm (2H) was compared to the one at 8.20 ppm (4H, d, CH) from the internal standard pyrene (see appendix for NMR spectra). The time between the addition of the initiator solution and the first measurement was added to the first measuring point.

Gel permeation chromatography (GPC): The relative molecular weight and molecular weight distribution of homo and block copolymers were determined by GPC measurements done on a Viscotek VE2001 system using THF as an eluent with a flow rate of 1 mL/min and injection volume of 100 μL . Polystyrene standards were used for conventional external calibration using a Viscotek VE3580 refractive index detector.

MALDI-TOF (Matrix Assisted Laser Desorption/Ionisation-Time of Flight): The cross-over reactions of block copolymer were determined both qualitatively and quantitatively using MALDI mass spectrometry. Positive ion MALDI-TOF measurements were performed on Bruker Autoflex-III instrument equipped with smart ion beam laser. Measurements were carried out in linear and reflector mode. Samples were prepared from THF solution by mixing matrix (20 mg/mL), polymer (20 mg/mL), and salt (20 mg/mL solution) in a ratio of 100:10:1. Dithranol (1,8-dihydroxy-9(10H)-anthracetone, Aldrich 97%), was used as matrix. Sodium trifluoroacetate (Aldrich, 98%) salt was added for ion formation, with sodium trifluoroacetate used as the optimal salt for obtaining the highest S/N-ratio.

Differential Scanning Calorimetry (DSC) : The glass transition temperatures of synthesized polymers were determined by DSC. Perkin Elmer Diamond was used for measurements with the heating and cooling rates of $dT/dt=10K/min$. Samples with approximately 5mg mass was encapsulated in the closed pans. Instrument was calibrated using indium as the reference material.

Small angle X-ray scattering (SAXS) : X-ray scattering measurements were performed on a small angle instrument assembled by JJ X-rays based on a 2D detector by Bruker Hi-star and a Rigaku rotating anode with focusing optics. Cu-K α radiations with wavelength $\lambda=1.56\text{\AA}$ was used for measurements. Instrument was calibrated using silver behenate as a reference material.

Transmission electron microscopy (TEM): TEM analyses were carried out using a JEOL 1010 machine operated at 100 keV to get the block copolymer morphology images.

2.2.2. Synthesis of *endo,exo*[2.2.1] bicyclo-2-ene-5,6-dicarboxylic acid dimethylester (2) (monomer A)

A modified literature synthesis¹³¹ was adopted. A dry round bottom flask equipped with magnetic stir bar was flushed with argon and charged with *endo, exo*-Bicyclo[2,2,1]-hept-5-ene-2,3-dicarboxylic acid (**1**) (4.33 g, 23.78 mmol) and excess thionyl chloride (SOCl₂) (17.13 mL, 0.24 mol). The mixture was refluxed for 4 h at 90° C and later the excess thionyl chloride was removed under reduced pressure to obtain *endo, exo*-Bicyclo[2,2,1]-hept-5-ene-2,3-dicarboxylic acid chloride. Further the methanol (3.1 g, 94.9 mmol) and pyridine (7.5 g, 95.2 mmol) were dissolved in 60 mL of dry CH₂Cl₂. Under ice cooling *endo,exo*[2.2.1] bicyclo-2-ene-5,6-dicarboxylic acid chloride (5.2 g, 23.8 mmol) was dropped into the reaction mixture and stirred overnight at room temperature. The reaction mixture was filtered to remove the pyridinium salt and extracted with CH₂Cl₂. The organic layer was extracted with 2N HCl solution, saturated sodium bicarbonate and dried with sodium sulfate. The solvent was removed under reduced pressure. Finally, the product was purified using column chromatography with petrolether/ethyl acetate (10:1) as the solvent mixture to yield 3.9 g (78%) of **2** (monomer A) as a white solid.

¹H NMR (δ , CDCl₃, 400 MHz): 6.27 (q, 1H), 6.07 (q, 1H), 3.71 (s, 3H), 3.64 (s, 3H), 3.37 (t, 1H), 3.26 (s, 1H), 3.13 (s, 1H), 2.68 (m, 1H), 1.60 (m, 1H), 1.47 (m, 1H).

^{13}C NMR (δ ppm, CDCl_3 , 101 MHz): 174.74, 173.54, 137.48, 135.12, 52.02, 51.74, 47.93, 47.66, 47.35, 47.18, 45.67.

2.2.3 Synthesis of *endo,exo*[2.2.1] bicyclo-2-ene-5,6-dicarboxylic acid-bis(3,3,4,4,5,5,6,6,7,7,8,8,8-tridecafluorooctyl) ester (3) (monomer C)

A dry round bottom flask equipped with magnetic stir bar was flushed with argon and charged with *endo, exo*-Bicyclo[2,2,1]-hept-5-ene-2,3-dicarboxylic acid (**1**) (2.5 g, 13.73 mmol) and excess thionyl chloride (SOCl_2) (8.23 mL, 0.114 mol). The mixture was refluxed for 4 h at 90° C and later the excess thionyl chloride was removed under reduced pressure to obtain *endo, exo*-Bicyclo[2,2,1]-hept-5-ene-2,3-dicarboxylic acid chloride. Further 1H,1H,2H,2H-perfluoro-1-octanol (15.78 mL, 34.3 mmol) and pyridine (3.68 mL, 50.2 mmol) were dissolved in 40 mL of dry CH_2Cl_2 . Under ice cooling *endo,exo*[2.2.1] bicyclo-2-ene-5,6-dicarboxylic acid chloride (2.42 g, 11.42 mmol) was dropped into the reaction mixture and stirred overnight at room temperature. The reaction mixture was filtered to remove the pyridinium salt and extracted with CH_2Cl_2 . The organic layer was extracted with 2N HCl solution, saturated sodium bicarbonate and dried with sodium sulphate. Organic phase was collected and the solvent was removed under reduced pressure. Finally, the product was purified using column chromatography with petrolether/ethyl acetate (10:1) as the solvent mixture to yield 6.96 g (70%) of **3** (monomer C) as a white solid.

^1H NMR (δ ppm, 400 MHz, CDCl_3) 6.27 (dd, $J = 5.59, 3.12$ Hz, 1H), 6.06 (dd, $J = 5.60, 2.81$ Hz, 1H), 4.36 (td, $J_{H-F} = 30.15, 6.35$ Hz, 4H), 3.41-3.20 (m, 2H), 3.17-3.06 (m, 1H), 2.66 (dd, $J = 4.57, 1.63$ Hz, 1H), 2.57-2.30 (m, 4H), 1.64-1.41 (m, 1H), 1.28-1.19 (m, 1H).

^{13}C NMR (δ ppm, CDCl_3 , 101 MHz): 173.63, 172.41, 137.55, 134.98, 100.00 – 120.20 (multiplet), 56.84 (dd, $J = 6.40, 2.74$ Hz), 56.59 (dd, $J = 6.70, 2.70$ Hz), 48.05, 47.50 (d, $J = 11.92$ Hz), 47.26, 45.67, 30.95-30.52.

2.2.4 Synthesis of *exo-N*-(4,4,5,5,6,6,7,7,7-nonafluoroheptyl)-10-oxa-4-azatricyclodec-8-ene-3,5-dione (8) (monomer D)

The synthetic procedure was adopted from reference.¹³² Freshly distilled furan (**4**) (15mL, 207.1 mmol) and maleimide (**5**) (2g, 20.6 mmol) were placed in a 100 mL large autoclave equipped with heating bath. The mixture was stirred at 90° C under argon

atmosphere for 10 h. The reaction vessel was cooled down to RT to regain atmospheric pressure whereupon white crystals precipitated. The white precipitate was collected by vacuum filtration and washed two times with furan. The white precipitate was dried further under high vacuum over night to yield 3.3 g (96%) of pure and dry exo-10-oxa-4-aza-tricyclo-dec-8-ene-3,5-dione (**6**).

^1H NMR (δ ppm, 400 MHz, DMSO): 11.09 (s, 1H), 6.48 (s, 2H), 5.07 (s, 2H), 2.83 (s, 2H).

^{13}C NMR (δ ppm, 101 MHz, DMSO): 178.8, 137.4, 81.3, 49.4.

A solution of 4,4,5,5,6,6,7,7,7-nonafluoro-heptan-1-ol (1.0 g, 3.60 mmol) and tetrabromomethane (1.878 g, 5.663 mmol) in dry CH_2Cl_2 (20 mL) was cooled to 0 °C, and a solution of triphenylphosphine (1.415 g, 5.393 mmol) in dry CH_2Cl_2 (5 mL) was added slowly. The ice bath was removed, and the mixture was stirred for 12 h at ambient temperature. After complete conversion the solvent was removed under reduced pressure (care was taken not to remove the intermediate 7-bromo-1,1,1,2,2,3,3,4,4-nonafluoroheptane from the reaction mixture under reduced pressure), and the crude product (**7**) was subsequently reacted without any further purification. Potassium carbonate (1.098 g, 7.910 mmol) and exo-10-oxa-4-azatricyclodec-8-ene-3,5-dione (**6**) (0.653 g, 3.955 mmol) was added to the crude 7-bromo-1,1,1,2,2,3,3,4,4-nonafluoroheptane (**7**) and resuspended in dry DMF (60 mL). The reaction mixture was stirred for 24 h at ambient temperature, and the solvent was removed subsequently under reduced pressure. The obtained crude compound was dissolved in CH_2Cl_2 and extracted with water, dried and subsequently the CH_2Cl_2 was removed under reduced pressure. Finally, the product was purified by chromatography (SiO_2 , hexane/ethyl acetate =1/1) in order to yield 1.0 g (61%) pure white crystals of **8** (monomer **D**).

^1H NMR (δ ppm, 400 MHz, CDCl_3): 6.51 (td, $J = 4.42, 0.80$ Hz, 2H), 5.26 (td, $J = 1.87, 0.90$ Hz, 2H), 3.57 (t, $J = 6.92$ Hz, 2H), 2.88-2.83 (m, 2H), 2.14-1.97 (m, 2H), 1.95-1.83 (m, 2H).

^{13}C NMR (δ ppm, 101 MHz, CDCl_3): 176.00, 136.44, 121.5-105.0 (multiplets, $J_{FC}^1 = 98\text{Hz}$, $J_{FC}^2 = 22$ Hz), 81.01, 47.40 (d, $J = 7.59$ Hz), 37.84, 28.52 (t, $J_{FC}^2 = 22$ Hz), 28.30, 28.08, 18.87 (t, $J = 3.85$ Hz).

2.2.5. Synthesis of poly(A₁₀₀)

A heated and argon-flushed glass tube equipped with a magnetic stirbar was charged with monomer **A** (83.0 mg, 0.39 mmol) in 1 mL of CH₂Cl₂. To this solution was added catalyst **I** (3.3 mg, 0.004 mmol) dissolved in 1 mL of CH₂Cl₂. The reaction mixture was stirred for 4 hours at room temperature till all of the monomer **A** was consumed, as checked by thin layer chromatography. The reaction was then quenched with cold ethyl vinyl ether and the resulting polymer was precipitated into cold methanol (300 mL). The methanol was decanted and the product was dried under high vacuum overnight to yield 80 mg (96%) of poly (**A**). The polymerization of monomer **A** with catalyst **III** was carried out in the same manner but with the polymerization time of 1 h due to the faster reaction. Poly (**A**)_n with different chain lengths (n) with both catalysts **I** and **III** were also prepared using the same procedure by adopting the required polymerization times.

¹H NMR (δ ppm, CDCl₃, 400 MHz): 5.48 -5.24 (m, 2H), 3.75-3.57 (m, 6H), 3.04-2.88 (m, 4H), 1.96 (s, 1H), 1.56 (s, 1H).

2.2.6. Synthesis of block copolymer Poly(A_m-b-C_n)

The general synthesis procedure of block copolymer Poly(A_m-b-C_n) is described below, for example Poly(A₅₀-b-C₁₃); monomer **A** (240.2 mg, 1.2 mmol) in 2 mL of CH₂Cl₂ was added to the Grubbs 1st-generation catalyst, [RuCl₂(PCy₃)₂(CHPh)] (18.8 mg, 0.022 mmol) dissolved in 2 mL of CH₂Cl₂ in a heated and argon-flushed glass vial equipped with a magnetic stir bar. The polymerization was carried out at room temperature for 2 h till all of monomer **A** was consumed, as checked by TLC. Monomer **C** (259.8 mg, 0.3 mmol) as a solution in 2 mL of CH₂Cl₂ was then added to the above reaction mixture and stirred for 7 h at room temperature till all of the monomer **C** was consumed, as checked by TLC. The polymerization was quenched by adding cold ethyl vinyl ether. The produced polymer was isolated by precipitating in to cold methanol. Finally the product was dried under high vacuum overnight to yield 485 mg (97%) of poly(A₅₀-b-C₁₃). The other block copolymer poly(A₅₀-b-C₈) with different block composition was synthesized using the above stated procedure but adopting the different monomer/initiator ratio.

¹H NMR (δ ppm, CDCl₃, 400 MHz): 5.60-5.10 (m, 2.6H), 4.51-4.15 (m, 1.2H), 3.73-3.57 (m, 6H), 3.38-2.59 (m, 5.1H), 2.43 (s, 1.3H), 1.95 (s, 1.2H), 1.54 (s, 1.2H).

2.2.7. Synthesis of block copolymer Poly(A_m-b-D_n)

The general synthesis procedure of block copolymer Poly(A_m-b-C_n) is described below, for example Poly(A₁₀₀-b-C₁₀₀); monomer **A** (33.1 mg, 0.16 mmol) in 0.5 mL of CH₂Cl₂ was added to the catalyst **I** [Grubbs 1st-generation, RuCl₂(PCy₃)₂(CHPh)] (5.18 mg, 0.006 mmol) dissolved in 1 mL of CH₂Cl₂ in a heated and argon-flushed glass vial equipped with a magnetic stir bar. The polymerization was carried out at room temperature for 1 h till all of monomer **A** was consumed, as checked by NMR and TLC. Monomer **D** (66.9 mg, 0.16 mmol) as a solution in 0.5 mL of CH₂Cl₂ was then added to the above reaction mixture and stirred for 1 h at room temperature till all of the monomer **D** was consumed, as checked by NMR and TLC. The polymerization was quenched by adding cold ethyl vinyl ether. The produced polymer was isolated by precipitating in to cold methanol or alternatively, the polymer was isolated by column chromatography (SiO₂). Finally the product was dried under high vacuum overnight to yield 97 mg (97%) of poly(A₁₀₀-b-D₁₀₀). The other block copolymers with different block composition were synthesized using the above stated procedure but adopting the different monomer/initiator ratio. The block copolymers poly(A_n-b-D_m) with catalysts **III** were synthesized using the same procedure but adopting the different reaction times according to the kinetic data.

¹H NMR (δ ppm, CDCl₃, 400 MHz): 6.20-4.22 (m, 6H), 3.77-3.60 (m, 6H), 3.60-3.45 (s, 2H), 3.43-2.60 (m, 6H), 2.15-1.77 (m, 5H), 1.55 (s, 1H).

2.3. Results and discussion

2.3.1. Polymerization of A_m-b-D_n

Polymerization reactions were conducted using Grubbs 1st- (**I**) and Grubbs 3rd-generation (**III**) catalyst. Grubbs 2nd generation (**II**) catalyst was not further investigated, as monomer **A** is only poorly polymerized with this catalyst (c.f. table 2.1). The kinetic features of the polymerization reactions were first analyzed via M_n vs. time-graphs (as measured by GPC with the monomers **A-D**). The GPC kinetic- and crossover-data are shown in figures 2.1 and table 2.1.

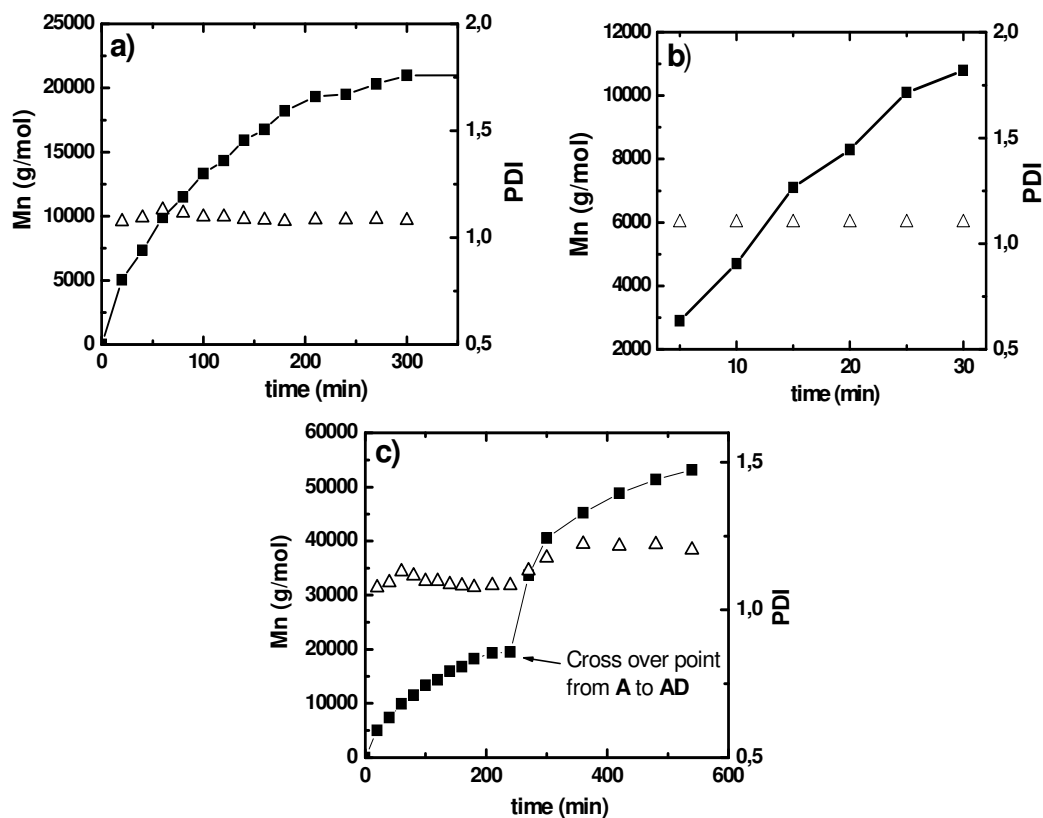


Figure 2.1. Increase in $M_n(\text{GPC})$ with polymerization time (t) a) for poly(**A**₁₀₀) and c) poly(**A**_{100-b-D}₁₀₀) using catalyst **I**, b) for poly(**A**₅₀) using catalyst **III**.

Figure 2.1 shows the homopolymerization of monomer **A** with catalyst **I** and **III** (Figure 2.1a, c) and the crossover-reactions from living poly (**A**) to monomer **D** (Figure 2.1c) and both reactions are well controlled, clearly demonstrating an efficient crossover-reaction between these monomers. GPC-data for the crossover-reactions are shown in Table 2.1, indicating the efficiency of this process, with M_w/M_n -values ranging from 1.1 – 1.2. In both cases, a significant change in the kinetics before and after the crossover-point can be seen. The polymerization of **D** onto the poly **A** chain was too fast with catalyst **III** to follow the kinetics with GPC and this prompted to study kinetics before and after the crossover-reactions, as monitored by $^1\text{H-NMR}$ -spectroscopy (figure 2.2), directly obtaining the $\ln(M_o/M_t)$ vs. time (t) graphs.

Table 2.1 GPC data for homo and block copolymerization of monomer **A** and **D**

sample	catalyst	M_n (calc.)	M_n (GPC)	PDI (GPC)
A ₁₀₀	I	21,000	20,400	1.1
A ₅₀	III	10,500	10,800	1.1
A ₁₀₀ D ₁₀₀	I	63,500	53,800	1.2
A ₁₀₀ D ₁₀₀	III	63,500	57,000	1.2
A ₁₀₀	II	21,000	91,200	1.2

Figure 2.2 shows the kinetic plots of homo and block copolymerization obtained by ¹H-NMR-spectroscopy and the extracted kinetic data (k_p -values) are compiled in Table 2.2, assuming first-order kinetics. k_p values were obtained by dividing the slope of $\ln(M_0/M_t)$ vs. time (t) linear curves by initial catalyst concentration $[I_0]$. Using Grubbs 1st-generation catalyst, monomer **A** is polymerized ~50 times slower than monomer **D** (k_p (**A**) = 0.05 L/(mol*s) vs. k_p (**D**) = 2.2 L/(mol*s)). Whereas a significant acceleration is observed when using Grubbs 3rd-generation catalyst with monomer **A** (k_p (**A**) = 2.6 L/(mol*s)), changes are insignificant with monomer **D** (k_p (**D**) = 5.7 L/(mol*s)). Observing the kinetics of the monomer **D** blockcopolymer (initiating polymerization with a constant block of living poly (**A**₂₀)) does lead only to small changes of the k_p -values of the individual monomers, indicative that the presence of a homopolymer chain poly (**A**) does not induce changes in the kinetics and thus the transitions-states during the catalytic process. The presence of residual monomer **A** before the crossover-reaction was checked by ¹H-NMR-spectroscopy and thin layer chromatography (tlc) to be below 1/100 of its starting value, thus excluding residual monomer **A** during the crossover-reaction.

Table 2.2. Polymerization kinetics data obtained from ¹H-NMR spectroscopy

experiment	catalyst	$[I]_0$ (mol/L)	k_p (L/mol*s)
D ₂₀	I	0.0065	homo-D 2.20
A ₂₀ D ₂₀	I	0.02	homo-A 0.05
A ₂₀ D ₂₀	I	0.015	block-D 1.30
D ₂₀	III	0.0066	homo-D 5.70
A ₂₀ D ₂₀	III	0.018	homo-A 2.60
A ₂₀ D ₂₀	III	0.0049	block-D 11.90

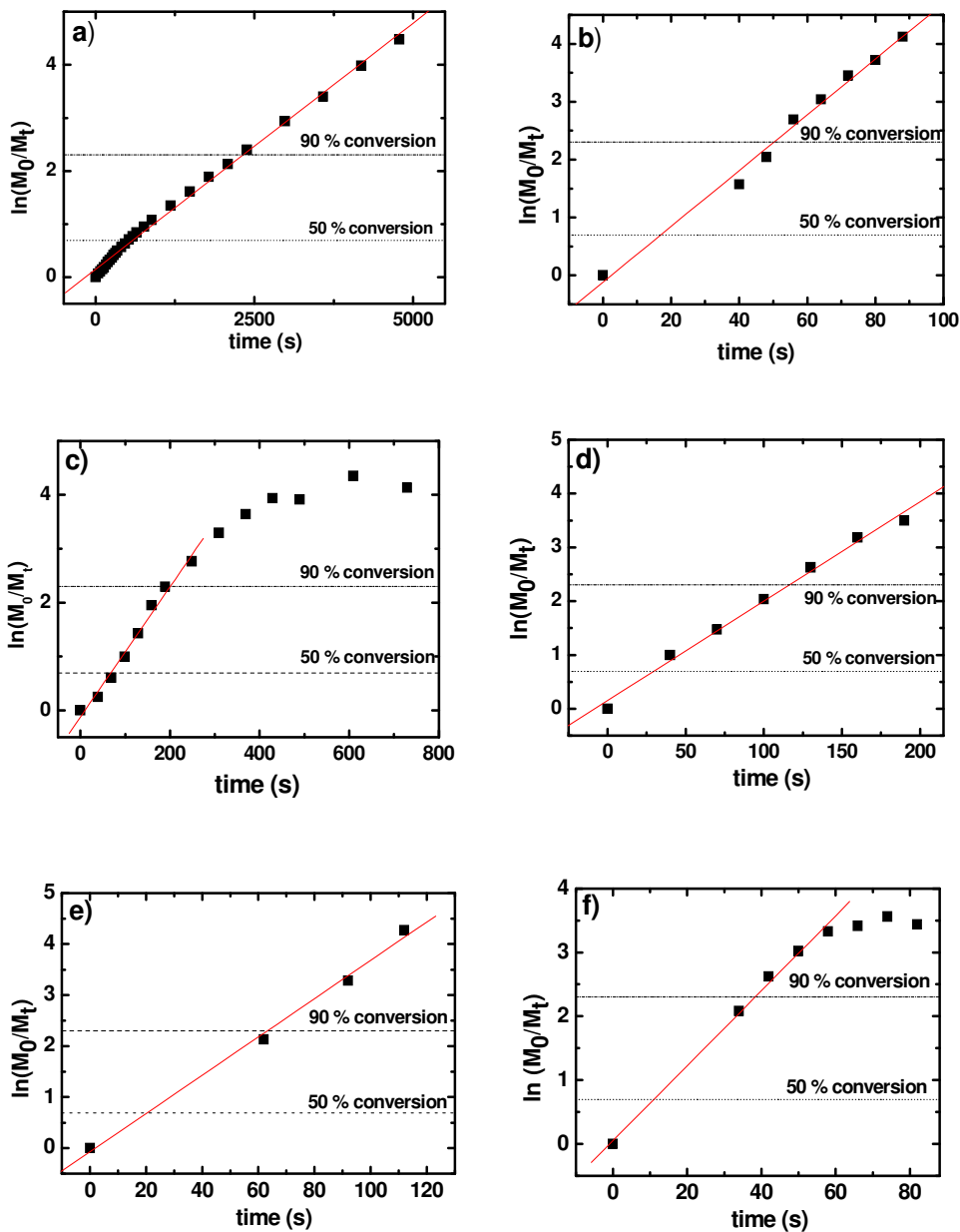


Figure 2.2. Monomer conversion v/s time (t) plots obtained from $^1\text{H-NMR}$ a) poly(A) with catalyst I, b) poly(A) with catalyst III, c) poly(D) with catalyst I, d) D in poly(A-b-D) with catalyst I, e) poly(D) with catalyst III and f) D in poly(A-b-D) with catalyst III. Solid line represents a linear fit.

2.3.2. Monitoring Crossover Efficiency via MALDI

As GPC or NMR-methods cannot provide a deeper insight into the crossover reaction, we have studied this process by MALDI-TOF-methods¹³⁶ as homopolymers derived from monomer A can be very well desorbed and detected by MALDI-methods as

analytical tool for monitoring the crossover-reaction. MALDI-mass spectrometry enables to monitor the analysis of copolymers¹³⁷, mostly described via block-copolymers prepared by mostly anionic-¹³⁸⁻¹⁴² and ring-opening-^{143, 144} polymerization processes. Thus, the successful analysis of ROMP- polymers has been described by various authors, enabling also the application to homopolymerization reactions¹⁴⁵ or endcapping-reactions^{146, 147} of norbornene-based monomers. The crossover-reaction was studied starting from the living poly (A_{15})-species (initiated either with Grubbs 1st- or 3rd-generation catalyst) and subsequent addition of exactly 1 or 4 equivalents of the second monomer (D) with respect to the living Ru-carbene – similar to step-crossover-experiments in living anionic polymerization processes.¹³⁹ GPC-traces do show the expected shift in molecular weight with increasing amounts of the second monomer (see figure 2.3) as also indicated in Table 2.3.

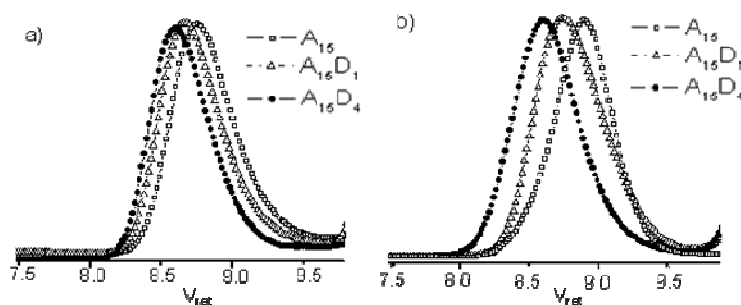


Figure 2.3. GPC curves of poly(A_{15}) and block-copolymer poly(A_{15} -b- D_1) and poly(A_{15} -b- D_4), a) polymerized with Grubbs-1st generation catalyst, b) polymerized with Grubbs-3rd generation catalyst

The polydispersity remains within the range of the homopolymer ($\sim 1.1 - 1.2$), the molecular weights (M_n) increase with increasing amount of added equivalents of monomer. As poly- (A_{15}) is an excellent probe for desorption in MALDI, the crossover-reaction was monitored directly using mass-spectrometry, enabling to check the individual species due to their different masses and isotope-patterns. Figure 2.4 and figure 2.5 show the MALDI-spectra for the crossover-reaction of the living homopolymer poly(A_{15}) with monomer D using Grubbs 1st - and 3rd - generation catalyst, respectively. The crossover-reaction of poly(A_{15} -b- D_1) and poly(A_{15} -b- D_4) using Grubbs 1st-generation catalyst indicates a slow crossover-reaction, with significant amounts of homopolymer present even after the addition of four equivalents of monomer D (see Figures 2.4). Thus significant peaks assignable to A_n -species without added D -monomers

can be observed. Surprisingly the crossover-reaction of poly(A_{15} -b- D_1) and poly(A_{15} -b- D_4) in the reaction catalyzed by Grubbs 3rd-generation catalyst show a similar picture (see Figure 2.5), despite the fact that the kinetics for monomer **D** and monomer **A** are significantly faster with Grubbs 3rd-generation catalyst (1st-generation (**I**): k_p (**A**) = 0.05 and k_p (**D**) = 2.2 L/(mol*s); 3rd-generation (**III**): k_p (**A**) = 2.60 and k_p (**D**) = 11.90 L/(mol*s)). The MALDI-analysis leads to the picture of a still incomplete crossover-reaction even with 4 equivalents of monomer **D**, irrespective of the use of Grubbs 1st- or 3rd-generation catalyst.

Table 2.3. Results for block copolymers obtained by crossover-reactions from monomer **A** to monomer **D**.

sample	catalyst	M_n (calc.) ¹	M_n (GPC)	PDI (GPC)	M_{peak} (MALDI) ²	M_n (MALDI) ³	PDI (MALDI) ⁴
A ₁₅	I	3255.4	2800	1.15	3280.3	2646.5	1.20
A ₁₅ D ₁	I	3680.5	3300	1.16	3494.8	3350.1	1.13
A ₁₅ D ₄	I	4955.7	3900	1.16	4556.0	4934.8	1.07
A ₁₅	III	3255.4	2500	1.13	2018.5	2250.9	1.07
A ₁₅ D ₁	III	3680.5	2900	1.18	3068.8	3888.3	1.09
A ₁₅ D ₄	III	4955.7	3900	1.14	4979.0	5878.5	1.06

¹) Calculated monoisotopic peak value including starting group (Ph), end group (vinyl) and excluding ions,

²) peak maximum of main series from MALDI spectra, ³) Calculated average M_n using Polytools[®] software,

⁴) M_w/M_n calculated using Polytools[®] software.

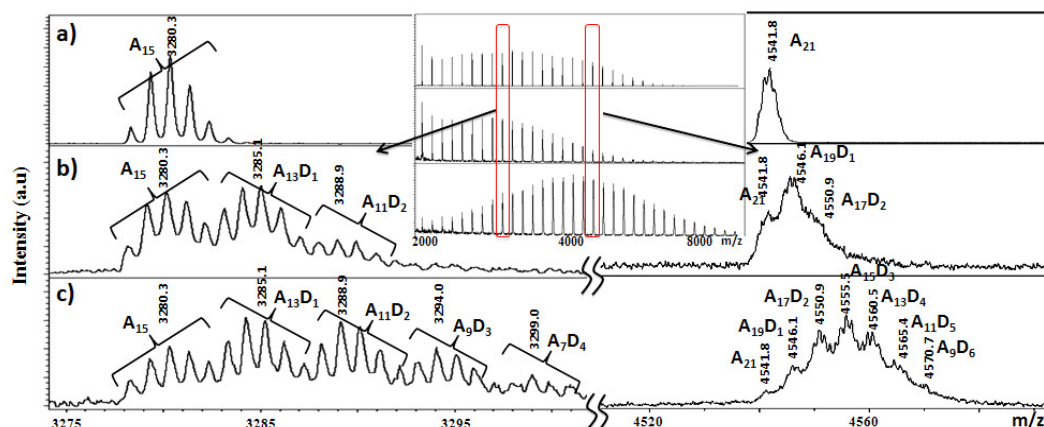


Figure 2.4. MALDI-TOF mass spectra of a) poly(A_{15}), b) poly(A_{15} -b- D_1) and c) poly(A_{15} -b- D_4) prepared via catalyst **I**. (Insert shows the complete MALDI-spectra of the sample a-c), (all chains are desorbed as $[M-Na^+]$ -ions).

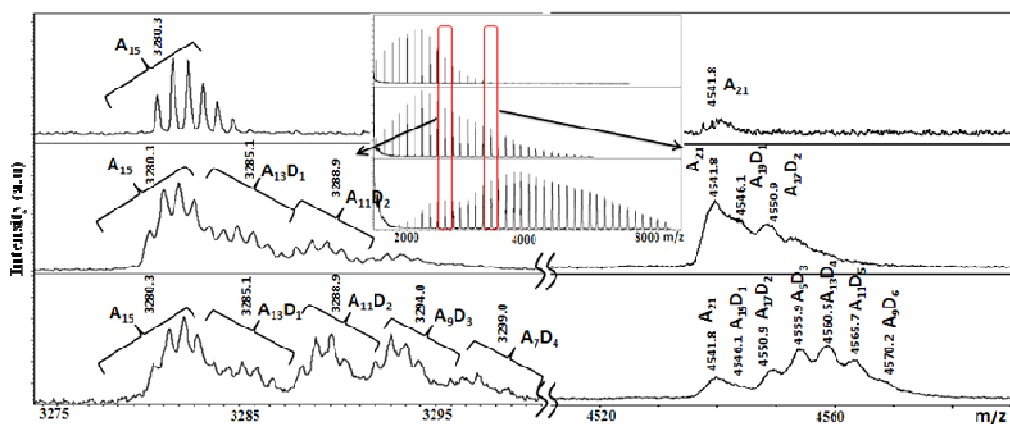


Figure 2.5. MALDI-TOF mass spectra of, a) poly(A_{15}), b) poly(A_{15} - b - D_1) and c) poly(A_{15} - b - D_4) prepared via catalyst **III**. (Insert shows the complete MALDI-spectra of the samples a-c), (all chains are desorbed as $[M-Na^+]$ -ions).

It is well known that MALDI-analyses can hardly be quantified between polymers of different chemical structures, as desorption of even high- and low molecular weight species of the same type of polymer might be different.¹⁴⁸⁻¹⁵² To this purpose we have measured sensitivity-plots according to literature^{149, 151, 153, 154}, by quantifying the intensity of defined physical mixtures in the final corresponding MALDI-spectra. The MALDI spectra of several stoichiometric mixtures (stoichiometric mixture ratios are shown in table 2.4) of poly- A_{15} and poly(A_{15} - b - D_4) were measured and the figure 2.6 shows the MALDI spectra of these mixtures. The samples for MALDI measurement were prepared by mixing different ratios of 20 mg/mL stock solutions of homopolymers and block copolymers with salt and matrix (dithranol). In the MALDI spectra of mixtures (figure 2.6) we see a bimodal distribution of the molar mass as expected. In the region 2000 to 5000 m/z we see the peaks originating from the Poly- A_{15} species and the peaks in the region of 5000 to 9000 m/z are related to poly(A_{15} - b - D_4). From the figure 2.6e it is obvious that the desorption of A_{15} and A_{15} - b - D_n species are quite different as the MALDI peak intensities originating from the A_{15} and A_{15} - b - D_n species are not same even though the mixture ratio of A_{15} to A_{15} - b - D_4 is one to one. These results demonstrate that the direct quantification of MALDI peaks is not possible and hence we measure the sensitivity plots as described below.

Table 2.4. Stoichiometric mixture ratios of poly-**A**₁₅ and poly(**A**₁₅-b-**D**₄). (Mixture solution concentration was 20 mg/mL in THF).

sample	A ₁₅ (μ L)	A ₁₅ -b- D ₄ (μ L)	M (μ L)	S (μ L)
a	1	9	100	1
b	2	8	100	1
c	3	7	100	1
d	4	6	100	1
e	5	5	100	1
f	6	4	100	1
g	7	3	100	1
h	8	2	100	1

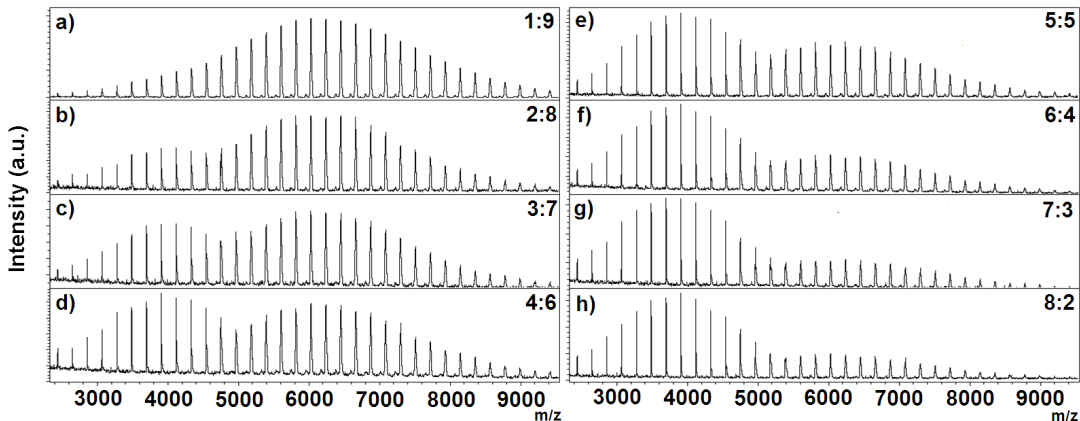


Figure 2.6. MALDI spectra of the samples for poly (**A**₁₅)/poly(**A**₁₅-b-**D**₄) mixtures showing bimodal distribution. The Peaks in the region of 2000 to 5000 m/z are originating from the Poly-**A**₁₅ species and the peaks in the region of 5000 to 9000 m/z are related to poly(**A**₁₅-b-**D**₄).

The quantities of the individual species were calculated from the individual MALDI peak intensity values, and the respective amounts of the poly(**A**_m-b-**D**_n)-species were summed up and thus quantified from the MALDI-spectrum. Thus we have quantified the influence of chain length of the second block (**D**) by measuring physical poly (**A**₁₅) vs. poly(**A**₁₅-b-**D**_n) mixtures (n = 1, 2, 3, and 4) against the individual ions (i.e.: by quantifying the poly(**A**₁₅)-[Na⁺] ion vs. the poly(**A**₁₅-b-**D**₁)-[Na⁺] ion, poly(**A**₁₅-b-**D**₂)-[Na⁺] ion, poly(**A**₁₅-b-**D**₃)- [Na⁺] ion, poly(**A**₁₅-b-**D**₄)-[Na⁺] ion). See table 2.5 for the weight ratios and the respective intensity ratios for the selected individual species.

Further the intensity ratios ($I_{A_{15}}/I_{A_{15}D_n}$) were plotted against the corresponding weight ratios ($W_{A_{15}}/W_{A_{15}D_n}$), yielding the individual sensitivity-values for the corresponding desorbed ions. The results are shown in figure 2.7, which provides the sensitivity factors of the poly(A_{15} -b- D_n)-series with : (A_{15} -b- D_1) / (A_{15} -b- D_2) / (A_{15} -b- D_3) / (A_{15} -b- D_4) = 2.14 / 2.38 / 2.02 / 1.52, all measured in relation to the poly(A_{15})-[Na⁺] ion. The differences between the desorption of the individual poly(A_{15} -b- D_n)-species are small, indicating that – including the above measured factors - the (semi-) quantification and thus evaluation of the individual species is possible.

Table 2.5. MALDI signal intensity ratios of poly (A_{15})/poly(A_{15} -b- D_4) mixtures.

Sample	$W_{A_{15}}/W_{A_{15}D_n}$	$I_{A_{15}}/I_{A_{15}D_1}$	$I_{A_{15}}/I_{A_{15}D_2}$	$I_{A_{15}}/I_{A_{15}D_3}$	$I_{A_{15}}/I_{A_{15}D_4}$
a	0.11	0.99	0.58	0.35	0.25
b	0.25	1.53	1.08	0.77	0.52
c	0.43	1.84	1.56	0.96	0.93
d	0.67	2.97	2.36	1.66	1.24
e	1	3.46	3.31	2.41	1.76
f	1.5	4.53	4.20	3.49	2.71
g	2.33	5.76	5.91	4.78	3.59

W=weight fraction in stoichiometric mixtures, I=intensity of a MALDI peak.

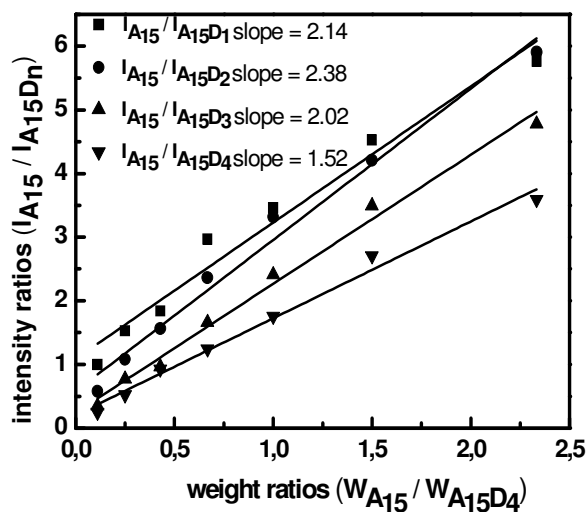


Figure 2.7. Plot of signal intensity ratios vs. weight ratios (MALDI-TOF mass spectra) of poly(A_{15}) and poly(A_{15} -b- D_4) mixtures. (Solid lines represent the linear fit).

Based on these data analysis, a rough quantification of the different species emerging directly after the corresponding crossover-reactions of living poly(A_{15}) with the various monomers, based on MALDI-analyses, was achieved (see Table 2.6).

Table 2.6. MALDI signal intensity ratios for crossover-reactions and the corrected intensities* are given within brackets.

entry	sample	catalyst	A ₁₅	A ₁₅ D ₁	A ₁₅ D ₂	A ₁₅ D ₃	A ₁₅ D ₄
1	A ₁₅ D ₁	I	1.00	1.10 (2.35)	0.51 (1.22)	-	-
2	A ₁₅ D ₄	I	1.00	1.55 (3.32)	2.03 (4.83)	2.10 (4.24)	1.92 (2.92)
3	A ₁₅ D ₁	III	1.00	0.72 (1.54)	0.51 (1.22)	-	-
4	A ₁₅ D ₄	III	1.00	0.53 (1.13)	1.64 (3.90)	1.73 (3.49)	1.65 (2.51)

(*) corrected intensities or the quantification number of A₁₅D_n species calculated by multiplying the MALDI peak intensity values with the respective slopes obtained from sensitivity plots of the individual ions (figure 9)

The data are shown for the individual crossover-experiments, listed according to the A_n-values, with setting the intensity of the respective poly(A₁₅)-species within one spectrum to 1.0. The values in brackets give the corresponding amounts generated by multiplying with the previously obtained sensitivity factors, thus representing the relative amounts of the individual poly(A₁₅-b-D_{1, 2, 3, 4}) species. Poly(A₁₅-b-D_n) (*entry 1 - 4*) show the poorer crossover-reaction as the amounts of initial homopolymer poly(A₁₅)-species are significantly increased relatively to poly(A₁₅-b-D₁), both with Grubbs 1st- and Grubbs 3rd-generation catalyst. Even with four equivalents of **D** (*entries 2 and 4*) the amount of poly(A₁₅) species is significant. This indicates that the point of crossover in ROMP may be very different from what kinetic data allow us to see, demonstrating the high importance of MALDI-methods for the (*semi*-)quantitative analysis of such processes.

Overall from these experiments we know that the Grubbs-3rd is much faster than the Grubbs-1st generation catalyst, whereas the crossover reactions are same in both the systems. The faster polymerization rate in case of Grubbs 3rd- compared to Grubbs 1st generation catalyst is a consequence of the more labile bis(3-bromopyridine) ligand and strongly binding N-hetero-cyclic (NHC) ligand.^{108, 115, 155} The bis(3-bromopyridine) ligands in Grubbs 3rd-generation catalyst dissociates from the metal center much faster than the highly electron donating tricyclohexylphosphine (PCy₃) ligands of Grubbs 1st generation catalyst to give an intermediate 14 e⁻ ruthenium species and hence faster initiation (k_i) with Grubbs 3rd-generation catalyst. Further a strong electron donating N-hetero-cyclic (NHC) ligand on Grubbs 3rd-generation catalyst compared to tricyclohexylphosphine (PCy₃) ligand in Grubbs 1st generation catalyst forms a stable

intermediate increasing the reactivity towards acidic olefins relative to the other electron donors in the system and hence faster propagation (k_p) of Grubbs 3rd- compared to Grubbs 1st generation catalyst.¹⁵⁵⁻¹⁵⁸ So overall Grubbs 3rd-generation catalyst having greater k_i and k_p and $k_i/k_p > 1$ (see table 2.2) compared to Grubbs 1st generation catalyst provides faster and controlled polymerization with both monomer **A** and **D**.

The polymerization kinetics being faster with Grubbs 3rd-generation catalyst, it is obvious that one would expect a better and complete crossover reaction from monomer **A** to **D** during block copolymerization with Grubbs 3rd-generation catalyst. However, according to MALDI-TOF MS results the presence of significant amount of homopolymer Poly-**A** chains after the block copolymerization with four equivalents of monomer **D** in the presence of Grubbs 3rd-generation catalyst contradicts the above statement. The faster copolymerization rate of monomer **D** compared to the polymerization of poly-**A** with both Grubbs 1st and Grubbs 3rd-generation catalyst, indicates the change in K_i and K_p at the second stage i.e. after addition of the second monomer **D**. We speculate that the slow initiation of the macro initiator^{159, 160} (poly-**A** chain with active ruthenium species) to coordinate with monomer **D** at the crossover from poly-**A** to **D** relative to the further propagation of block **D** could be the reasons for incomplete crossover reaction. The probable reasons for the slow initiation at the second stage could be a) the steric hindrance of the poly-**A** chain with ruthenium species hindering the faster co-ordination of monomer **D** to the ruthenium center, b) monomer **D** have an electron withdrawing semi-fluorinated side chains and such groups decrease the amount of electron density localized in the double bond,^{159, 161} thereby decreasing the ability of monomer **D** to co-ordinate to the ruthenium center, c) the association of dissociated ligands [tricyclohexylphosphine (PCy_3) in Grubbs 1st and bis(3-bromopyridine) ligand in Grubbs 3rd-generation catalyst]^{158, 159} onto the ruthenium center, which are still present in the reaction mixture, are preferred over monomer **D**. This is due to the higher electron donating nature of dissociated ligands in relative to monomer **D**. It is also well known that the phosphine ligands binds less strongly to the metal alkylidene than to the metal alkylidene bearing the growing polymer chain.¹⁵⁹ Due to the practical limitation it was not possible to resolve the rate of initiation (k_i) and rate of propagation (k_p) at the second stage of polymerization and hence k_{app} are listed in table 2.2. With all performed experiments it should be noted that all block copolymers could be obtained with defined molecular weights as calculated and low polydispersities

($M_w/M_n < 1.20$) and crossover with more equivalents of monomer **D** would give better cross over reaction. Further the block copolymer A_m-b-D_n with different block compositions having longer chain lengths were synthesized using Grubbs-1st generation catalyst, keeping the overall degree of polymerization constant to 200 units. The GPC data for all composition of A_m-b-D_n polymers are listed in table 2.7.

2.3.3. Polymerization of A_m-b-C_n

Block copolymerization of poly(A_m-b-C_n) was carried out using Grubbs-1st generation catalyst and the increase in molecular weight (M_n) with polymerization time was monitored with GPC. The monomer **A** was first polymerized for 2h to obtain a living polymer A_{50} chain with molecular weight ($M_n = 8,400$ g/mol) which was comparable to the calculated molecular weight with low polydispersity index (PDI = 1.17). Subsequently monomer **C** was added to the above reaction mixture. 4 hours after adding monomer **C** the M_n was increased to 16,400 g/mol according to GPC measurements suggesting the addition of ~ 10 units of monomer **C** onto the polymer A_{50} chain and confirming the crossover reaction. However, further proceeding with the reaction did not remarkably increase the molecular weight, instead there was an increase in PDI value and also precipitation occurred. The integral value of ¹H-NMR spectra suggested that 13 units of **C** addition onto the polymer **A** chain (see appendix for NMR spectra). The precipitation indicates that the limited solubility of the block copolymer is responsible for stopping the polymerization. Thus, a maximum of 13 repeating units of monomer **C** was able to polymerize onto the polymer **A** chain irrespective of the chain length of **A**. The block copolymers with two different block length of **C** i.e. 8 and 13 was synthesized keeping the block **A** length constant to 50 units. See table 2.7 for the GPC data of poly(A_m-b-C_n). Homo-polymerization of monomer **C** was not possible due to the precipitation of the polymer after polymerizing 3-4 units.

Table 2.7. GPC and DSC data for polymers A_m -b- D_n and A_m -b- C_n

sample	M_n (cal) ¹⁾ (g/mol)	M_n (GPC) (g/mol)	PDI	T_g A (° C)	T_g D/C (° C)
A ₂₀₀	42,046	40,000	1.17	77.9	-
A ₁₇₀ -b-D ₃₀	48,450	37,300	1.20	83.8	-
A ₁₄₀ -b-D ₆₀	54,900	40,300	1.20	83.6	103.1
A ₁₀₀ -b-D ₁₀₀	63,500	53,800	1.20	82.9	101.3
A ₆₀ -b-D ₁₄₀	72,100	41,900	1.20	81.7	105.5
A ₃₀ -b-D ₁₇₀	78,550	46,200	1.20	-	105.6
A ₅₀ -b-C ₁₃	21,862	16,400	1.20	67.5	24.8
A ₅₀ -b-C ₈	17,492	13,000	1.20	68.1	22.0

¹⁾ Calculated molecular weight

2.3.4. Thermal characterization of BCPs

The thermal glass transition temperature (T_g) of all synthesized block copolymers was determined by DSC measurements and the thermal stability was checked by TGA. The homopolymer A₂₀₀ exhibits a T_g around $\sim 78^\circ$ C (figure 2.8 and table 2.7) whereas the block copolymers A₅₀-b-C₁₃ and A₁₀₀-b-D₁₀₀ shows two different T_g 's. In the DSC specific heat curve for A₅₀-b-C₁₃ (figure 2.8b) we see two steps, one at $\sim 80^\circ$ C corresponding to the T_g of block A (according to homopolymer A DSC data) and the other at $\sim 30^\circ$ C corresponding to the block C. The lower T_g of block C can be accounted to the shorter chain length and the internal plasticization effect induced by the flexible semi-fluorinated alkyl side chains.¹⁶² Whereas in case of A₁₀₀-b-D₁₀₀ the T_g corresponding to the block A is found at $\sim 80^\circ$ C and the T_g of block D at higher temperature around 100° C (figure 2.8c). The presence of two T_g 's is a clear indication of a two phase system formed due to microphase separation. The T_g values for all the block copolymers are tabulated in table 2.7. The TGA curves for A₂₀₀, A₅₀-b-C₁₃ and A₁₀₀-b-D₁₀₀ are plotted in figure 2.9. All polymers are quite stable till 250° C and the onset of degradation occurs above this temperature, probably due to the cleavage of ester groups on norbornenes. The major degradation happens from around 350° C to 450° C.

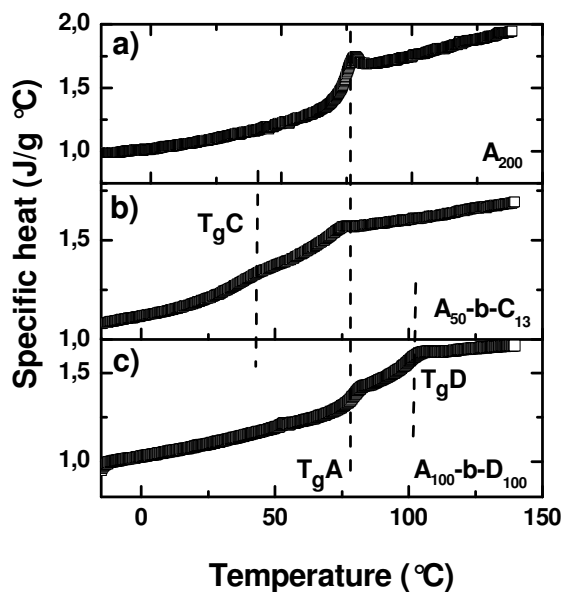


Figure 2.8. Specific heat vs. temperature (DSC) curves for a) homopolymer A_{200} and block copolymers b) $A_{50}\text{-b-C}_{13}$ and c) $A_{100}\text{-b-D}_{100}$.

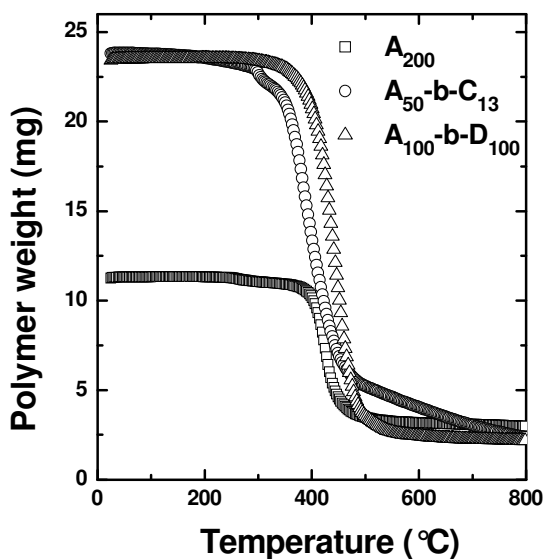


Figure 2.9. TGA curves, change in polymer weight with temperature, for a) homopolymer A_{200} and block copolymers b) $A_{50}\text{-b-C}_{13}$ and c) $A_{100}\text{-b-D}_{100}$.

2.3.5. BCP morphology characterization

The microphase separation and its morphology of the synthesized block copolymers, $A_m\text{-b-D}_n$ and $A_m\text{-b-C}_n$, was determined by small angle X-ray scattering (SAXS). The SAXS data are listed in table 2.8 and the scattering curves are shown in figure 2.10. The higher order scattering peaks up to third or fourth order in case of block copolymers $A_{100}\text{-b-}$

D_{100} , $A_{140}\text{-b-D}_{60}$, $A_{50}\text{-b-C}_{13}$ and $A_{50}\text{-b-C}_8$ indicates the presence of long range ordered structures due to microphase separation.¹⁶³ Whereas in the block copolymers with other compositions the absence of higher order scattering peaks with quite broad first order scattering peak (q_1) indicates the probable disordered state.¹⁶⁴

Table 2.8. Small angle X-ray scattering (SAXS) data of block copolymers

sample	q_1 (\AA^{-1})	period (nm), (SAXS)	morphology
$A_{170}\text{-b-D}_{30}$	0.022	28	lamellar
$A_{140}\text{-b-D}_{60}$	0.019	33	lamellar
$A_{100}\text{-b-D}_{100}$	0.020	31	hexagonal
$A_{60}\text{-b-D}_{140}$	0.028	22	disordered
$A_{30}\text{-b-D}_{170}$	-	-	miscible
$A_{50}\text{-b-C}_{13}$	0.026	24	hexagonal
$A_{50}\text{-b-C}_8$	0.030	21	lamellar

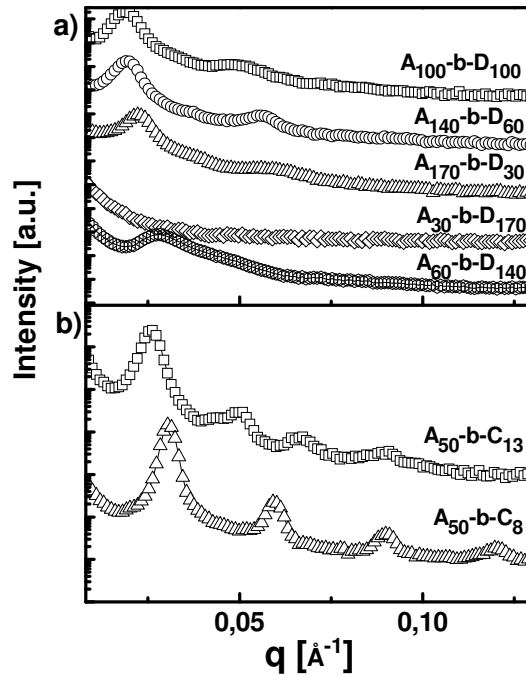


Figure 2.10. Small angle X-ray scattering curves (I vs q) for a) $A_m\text{-b-D}_n$ and b) $A_m\text{-b-C}_n$ at room temperature. The data sets are vertically shifted.

In the case of $A_{100}\text{-b-D}_{100}$, a prominent first order scattering peak centred at 0.020 \AA^{-1} corresponding to the long period (d) of 31 nm according to $q = 2\pi/d$ and the relative peak positions of the higher order scattering peaks with q_1 are in the ratio of $1:\sqrt{3}:\sqrt{7}$

suggesting the hexagonally ordered cylindrical structures. In case of $A_{140}\text{-b-D}_{60}$ the q_1 is positioned at 0.019 \AA^{-1} and the higher order scattering peak positions are in the ratio 1:2:3 indicating the lamellar structure with 33 nm periods. The lamellar and cylindrical morphologies of $A_m\text{-b-D}_n$ were confirmed by transmission electron microscopy (TEM). Block **D** containing fluorine and oxygen display higher mass/thickness contrast than the non-fluorinated block **A**. Figure 2.11a displays the TEM image of $A_{100}\text{-b-D}_{100}$ in which the cylinders of block **A** (bright) are arranged hexagonally in the matrix of **D** (dark), but in $A_{140}\text{-b-D}_{60}$ (figure 2.11b) the bright (**A**) and dark (**D**) lamellae are seen.

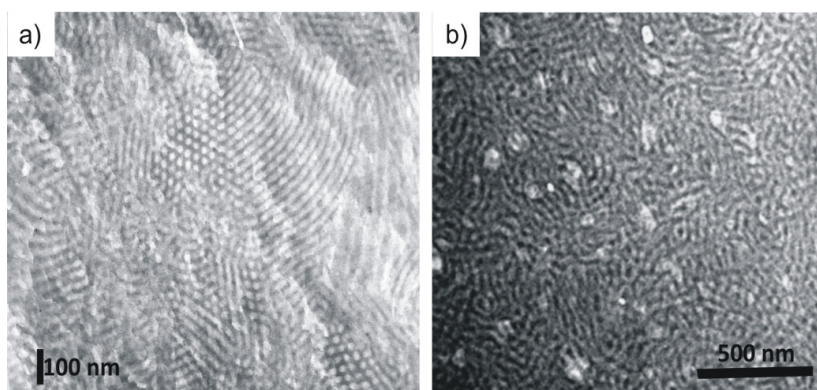


Figure 2.11. TEM image of a) $A_{100}\text{-b-D}_{100}$, hexagonally packed cylinders (bright) of block **A** in matrix of block **D** (dark). b) $A_{140}\text{-b-D}_{60}$, lamellar morphology.

In the case of $A_{50}\text{-b-C}_{13}$, we can see a sharp first order scattering peak (q_1) positioned at 0.026 \AA^{-1} corresponding to the long period (d) of 24 nm and the relative peak positions of the higher order scattering peaks with q_1 are in the ratio of $1:\sqrt{3}:\sqrt{4}:\sqrt{7}:\sqrt{9}$ suggesting the hexagonally ordered cylindrical structures. Whereas in case of $A_{50}\text{-b-C}_8$ a narrow first order scattering peak (q_1) is positioned at 0.030 relating to the long period (d) of 21 nm with equidistantly spaced higher order peaks in relative to q_1 (1:2:3:4) confirming the lamellar structure (see figure 2.10b). The transition from cylindrical to lamellar structures upon decreasing the chain length of block **C** from 13 to 8 indicates the larger volume fraction of **C** in block copolymer $A_{50}\text{-b-C}_{13}$ and hence it is reasonable to assume the cylinders of **A** in the matrix of **C**. The TEM imaging of $A_m\text{-b-C}_n$ was not possible due to the poor contrast.

2.4. Conclusions

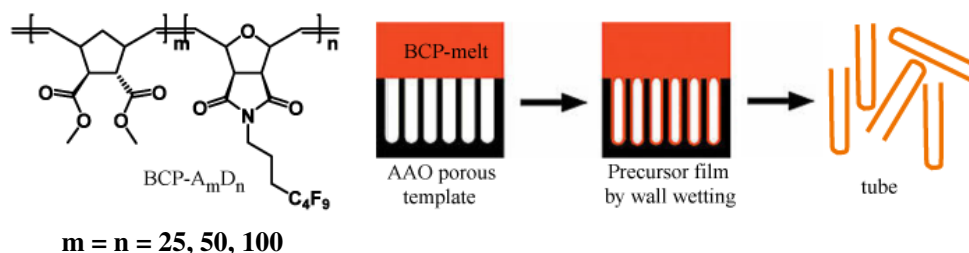
In this section, we presented the synthesis of well defined semi-fluorinated norbornene block copolymers via ROMP using Grubbs type catalyst. Polymerization kinetics study via ^1H NMR and GPC shows that the Grubbs 3rd generation is faster than Grubbs 1st generation catalyst. Both catalysts provide controlled polymerizations to give homo and block copolymers with low polydispersity of 1.2 indicating the good cross over reaction. In contrast MALDI analysis revealed a large amount of homopolymer A species present even after completion of reaction proving the incomplete crossover reactions. Hence MALDI spectrometry method can be effectively used to study the crossover reactions of similar type of monomers both qualitatively and quantitatively. However final BCPs obtained have low polydispersities sufficient for our studies. SAXS and TEM analysis revealed the lamellar and cylindrical morphologies of synthesized BCPs with period of 20-30 nm.

Section 3

Block copolymer Nanotubes by Melt-Infiltration of Nanoporous Aluminum Oxide

3.1. Concept

In this section, we discuss about the preparation of BCP nanotubes by melt infiltration of specifically designed norbornene block copolymers into AAO porous templates. The preparation of BCP nanotubes by infiltration of BCP solutions into shape-defining nanoporous hard templates cannot be controlled to a satisfactory degree, while infiltration of BCP melts in past has always yielded only solid nanorods by capillary filling. The precursor film formation by BCP melt on pore walls via wall wetting and subsequent solidification can yield BCP tubular structures. The BCP precursor film formation on pore walls would be possible if the surface energy of the newly formed BCP/air interface is low enough. Hence, we evaluate if it is possible to form a BCP precursor film on the alumina pore wall via wall wetting to obtain the BCP nanotubes by melt infiltration of poly(A_m - b - D_n) into porous alumina template. The synthesis of the low surface energy block copolymers poly(A_m - b - D_n) (scheme 3.1) are discussed in section 2 in which **A** block bearing polar group prefers AAO pore wall and on the other hand fluorinated block-**D** prefers the polymer/air interface. The surface energy of poly(A_m - b - D_n) is measured by water drop contact angle and melt drop measurements and the infiltrate structures are analyzed by SEM and TEM imaging. The BCP melt infiltration process also depends on the rheological properties and microscopic states of order of BCPs. Hence, we also evaluate the influence of BCP rheology and ordering on the morphology of nanostructures formed, i.e. tubes or rods, by altering the overall chain length of poly(A_m - b - D_n) ($m=n=25, 50, 100$). Rheological properties and microscopic state of order are evaluated using melt shear and scattering experiments respectively.



Scheme 3.1. The general structure of BCP A_m - b - D_n and melt infiltration into AAO porous template.

3.2. Characterization methods for bulk A_m -b- D_n

Gel Permeation Chromatography (GPC): GPC measurements were carried out on a Viscotek VE2001 system to determine molecular weight distributions. Polystyrene standards were used for conventional external calibration with Viscotek VE3580 refractive index detector.

Differential Scanning Calorimetry (DSC): DSC measurements were performed under nitrogen atmosphere at heating rates of 10 K/min, a Mettler Toledo DSC-H22 instrument was used. Glass transition temperatures were acquired from the second heating runs. Samples with approximately 10mg mass was encapsulated in the standard open pans.

Small Angle X-ray scattering (SAXS): SAXS measurements on bulk samples were performed on a small angle instrument assembled by JJ X-rays based on a 2D detector by Bruker Hi-star and a Rigaku rotating anode with focusing optics. Cu-K α radiations with wavelength $\lambda=1.56\text{\AA}$ was used for measurements. Instrument was calibrated using silver behenate as a reference material. For high temperature measurements, Linkam hot stage was used with equilibration time of 30 minutes.

Rheological measurements: Dynamic shear modulus $G^*=G'+iG''$ and complex viscosity (η^*) of BCP melt was measured using Anton Paar MCR501 rheometer. Parallel plate geometry was used and measured in the frequency range from 0.01 to 100 rad/s in the linear deformation range. All the measurements were performed in controlled nitrogen atmosphere.

Surface energy measurements: The sessile drop method was employed to determine the surface tension of A_m -b- D_n at 150 °C under argon atmosphere with a video-supported contact angle instrument OCA20 (DataPhysics Instruments, Germany). To assure formation of axisymmetric drops, samples were put on a cylindrical sample holder (stainless steel, $d = 5$ mm) with a polished surface. The drops reached their equilibrium shape after heating the BCP to 150°C for 30 minutes. The surface tension was obtained by averaging the results of five independent measurements by axisymmetric drop shape analysis¹⁶⁵ using ADSA software. Using the same device, the contact angle of water on 300 nm thick A_m -b- D_n films annealed for 12 h at 150°C was determined at room temperature. For this purpose, 10 to 15 μ l of ultrapure water were deposited onto the A_m -

b- D_n films using an automated dosing unit. Results obtained from four independent measurements were averaged.

3.3. Preparation of A_m -b- D_n nano-tubes and rods

Porous alumina templates (AAO) were kindly provided by Max-Planck Institute for Micro-structure Physics, Halle. These self ordered nano pore array of AAO templates are prepared by anodic oxidation of aluminum according to the procedures developed by Masuda et.al.^{63, 64} AAO templates were characterized by SEM and the nano pores are arranged in hexagonal pattern. Templates with 400 nm pore diameter and 100 or 60 μm depth were used for infiltration.

A_m -b- D_n BCP was homogeneously distributed on AAO membranes heated to 150°C and the BCP melt was spread over the alumina surface homogeneously. The AAO coated with A_m -b- D_n was then placed in a cylindrical furnace and kept at 150°C for 48 h under argon atmosphere while a load of 0.7 kg/cm² was applied to press the BCP against the AAO. After removing the samples from the furnace, residual BCP was removed from their surfaces by scraping with sharp blades. Then the aluminium substrates, to which the porous alumina layers had been attached, were selectively etched with a solution containing CuCl₂·2H₂O and 37% HCl at RT for around 10 minutes. Further SEM images were taken with a JEOL JSM-6701F microscope operated at accelerating voltages of 5.0 kV on the top and cross-sectioned surface of the template in order to check the infiltrated nanostructures (tube or rods). To release the A_m -b- D_n 1D nanostructures, the AAO was selectively etched with aqueous KOH for 24 h. The suspensions thus obtained were washed several times with deionized water and methanol. Methanolic suspensions of released A_m -b- D_n 1D nanostructures were directly dropped onto copper grids coated with a holey carbon film and probed by TEM using a JEOL 1010 machine operated at 100 keV. The internal morphology of the A_m -b- D_n tube wall was probed by TEM on ultrathin slices containing sections of A_m -b- D_n nanotubes. The ultrathin slices were prepared by depositing A_m -b- D_n 1D nanostructures into conical molds and embedding them in epoxy resin (Durcupan ACM). After curing at 60°C for 48 hours, the specimens were mounted on an ultra-microtome equipped with a diamond knife. Slices with a thickness of 100 nm or less, as determined from their interference colors, were transferred onto copper grids coated with holey carbon films for TEM analysis.

3.4. Results and Discussion

Series of block copolymers $\mathbf{A}_m\text{-b-}\mathbf{D}_n$ with symmetric block lengths having different overall chain length (i.e. $\mathbf{A}_{100}\text{-b-}\mathbf{D}_{100}$, $\mathbf{A}_{50}\text{-b-}\mathbf{D}_{50}$ and $\mathbf{A}_{25}\text{-b-}\mathbf{D}_{25}$) were melt infiltrated into 400 nm nanoporous aluminium oxide template at 150° C. The BCP $\mathbf{A}_m\text{-b-}\mathbf{D}_n$ consists of a polar block **A** bearing two ester groups per repeat unit and a second block **D** containing one perfluorinated alkyl moiety per repeat unit, leading to a higher incompatibility between the two blocks and a low interfacial energy. The synthetic details of $\mathbf{A}_m\text{-b-}\mathbf{D}_n$ are given in section 2. Scheme 3.1 depicts the general structure of infiltrated BCP and melt infiltration, table 3.1 shows the GPC and DSC data.

Table 3.1. GPC and DSC data of infiltrated block-copolymers

Sample	$M_n^{2)}$ (cal) (g/mol)	M_n (GPC) (g/mol)	PDI	Tg ₁ ¹⁾ (° C)	Tg ₂ ¹⁾ (° C)
$\mathbf{A}_{100}\text{-b-}\mathbf{D}_{100}$	63 500	50 800	1,2	82.8	101.3
$\mathbf{A}_{50}\text{-b-}\mathbf{D}_{50}$	31 750	24 300	1,2	81.7	101.9
$\mathbf{A}_{25}\text{-b-}\mathbf{D}_{25}$	15 875	14 200	1,1	80.1	-

¹⁾ Determined by DSC measurements

²⁾ Calculated molecular weight

3.4.1. X-ray scattering and Rheology characterization of bulk $\mathbf{A}_m\text{-b-}\mathbf{D}_n$

The microscopic state of order of the samples at infiltration temperature (150° C) was analyzed by small angle X-ray scattering (SAXS) and dynamic mechanical measurements at 150° C. In the SAXS-analysis (see Table 3.2 and Figure 3.1a) the presence of higher order scattering peaks for the sample $\mathbf{A}_{100}\text{-b-}\mathbf{D}_{100}$ clearly proved the presence of an ordered structure due to microphase separation^{163, 166} at the conditions of filling (T=150 °C). The ratio of the relative peak positions of scattering peaks (1:√3:√7) and the TEM image (see figure 3.7c) suggest a hexagonal morphology. Although in case of $\mathbf{A}_{50}\text{-b-}\mathbf{D}_{50}$ the higher order scattering peaks are weak (1: √4:√7), they still indicated that the sample is microphase separated which is also confirmed by narrow first order scattering peak (cf. table 3.2). In contrast, the sample $\mathbf{A}_{25}\text{-b-}\mathbf{D}_{25}$ shows a much broader scattering peak (cf. table 3.2) and no higher order reflections both indicating a disordered structure. The quantitative analysis of the scattering pattern (FWHM and χN) was done using the mean field expression for the structure factor given by Leibler.¹⁶⁴ The Leibler fit was performed only for $\mathbf{A}_{25}\text{-b-}\mathbf{D}_{25}$ because the Leibler structure factor is not applicable for ordered structures (figure 3.1b) whereas the other two BCPs were fitted

using Lorentz peak + power law fitting function for the calculation of full width half maximum (FWHM) of first order scattering peak (see figure 3.1c and d).

The Structure Factor $S(q)$ according to Leibler¹⁶⁴ reads as

$$S(q) = \frac{N}{F(x) - 2\chi N} \quad (3.1)$$

$$\text{Where: } F(x) = \frac{g_D(x,1)}{g_D(x,f)g_D(x,1-f) - \frac{1}{4}[g_D(x,1) - g_D(x,f) - g_D(x,1-f)]^2} \quad (3.2)$$

$g_D(x, f)$, the Debye function, is defined as

$$g_D(x, f) = \frac{2}{x^2} (fx + e^{-fx} - 1)$$

and

$$x = q^2 Nb^2 / 6 = q^2 R_g^2$$

With R_g denoting the radius of gyration of a Gaussian chain of N monomers each of the length b . The structure factor $S(q)$ in eq. (3.1) has a maximum for scattering vectors $q = q^*$. There is a certain critical value of χN , $(\chi N)_s$, for which $S(q)$ diverges at $q = q^*$. $(\chi N)_s$ depends on the composition f . We know from SAXS and TEM analysis that $\mathbf{A}_{100}\text{-b-}\mathbf{D}_{100}$ having cylindrical morphology is asymmetric in block composition. Hence it is reasonable to assume that the composition of a minor component in $\mathbf{A}_m\text{-b-}\mathbf{D}_n$ (when $m=n$) is $f=1/3$. Therefore here we use $f=1/3$ for the determination of χN .

$$(\chi N)_s = 13.1372 \quad , \quad f = 1/3. \quad (3.3)$$

Based on eq. (3.1), the scattering data for the block copolymer $\mathbf{A}_{25}\text{-b-}\mathbf{D}_{25}$ were fitted and the fit function was defined as

$$y(q) = \frac{K}{F(q, R_g) - a} + y_0 + bq^c \quad (3.4)$$

where $F(q, R_g)$ corresponds to $F(x)$ in eq. (3.2) with $f = 1/3$. K , R_g , a , y_0 , b and c were fit parameters. The first part of $y(q)$ is proportional to the structure factor according to Leibler. The two other contributions in eq. (3.4) represent scattering that is not due to the structure of the block copolymer. In figure 3.1b, the SAXS data of the block copolymer

$\mathbf{A}_{25}\text{-b-}\mathbf{D}_{25}$ at 150°C are shown together with a fit corresponding to $y(q)$ in eq. (3.4). According to this fit

$$(\chi N)_{\mathbf{A}_{25}\text{-}\mathbf{D}_{25}} = 12.03 \quad (150^\circ \text{C}) \quad (3.5)$$

This value is particularly smaller than $(\chi N)_s$ in eq. (3.3) indicating the disordered state of $\mathbf{A}_{25}\text{-b-}\mathbf{D}_{25}$ at 150°C . In addition, one can also easily calculate $(\chi N)\mathbf{A}_{50}\text{-b-}\mathbf{D}_{50}$ and $(\chi N)\mathbf{A}_{100}\text{-b-}\mathbf{D}_{100}$ since the corresponding block copolymers only possess a higher degree of polymerization than $\mathbf{A}_{25}\text{-b-}\mathbf{D}_{25}$

$$(\chi N)_s = 13.14, \text{ spinodal point.}$$

$$(\chi N)\mathbf{A}_{25}\text{-b-}\mathbf{D}_{25} = 12.03, \text{ disordered.}$$

$$(\chi N)\mathbf{A}_{50}\text{-b-}\mathbf{D}_{50} = 24.06, \text{ ordered.}$$

$$(\chi N)\mathbf{A}_{100}\text{-b-}\mathbf{D}_{100} = 48.12, \text{ ordered.}$$

The Leibler fit for $\mathbf{A}_{25}\text{-b-}\mathbf{D}_{25}$ scattering pattern yields a χN value of about 12.03, below the critical value of 13.14 for asymmetric block-copolymers ($f = 1/3$) at which microphase separation sets in and this confirms the disordered state of $\mathbf{A}_{25}\text{-b-}\mathbf{D}_{25}$ at infiltration conditions.

Table 3.2. SAXS data of infiltrated block-copolymers at 150°C

sample	FWHM* (nm^{-1}), (SAXS)	χN	period (nm), (SAXS)	morphology
$\mathbf{A}_{100}\text{-b-}\mathbf{D}_{100}$	0.0042	48.12	31	hexagonal
$\mathbf{A}_{50}\text{-b-}\mathbf{D}_{50}$	0.0059	24.06	22	hexagonal
$\mathbf{A}_{25}\text{-b-}\mathbf{D}_{25}$	0.0215	12.03	15	disordered

* Full width half maximum of first order scattering peak

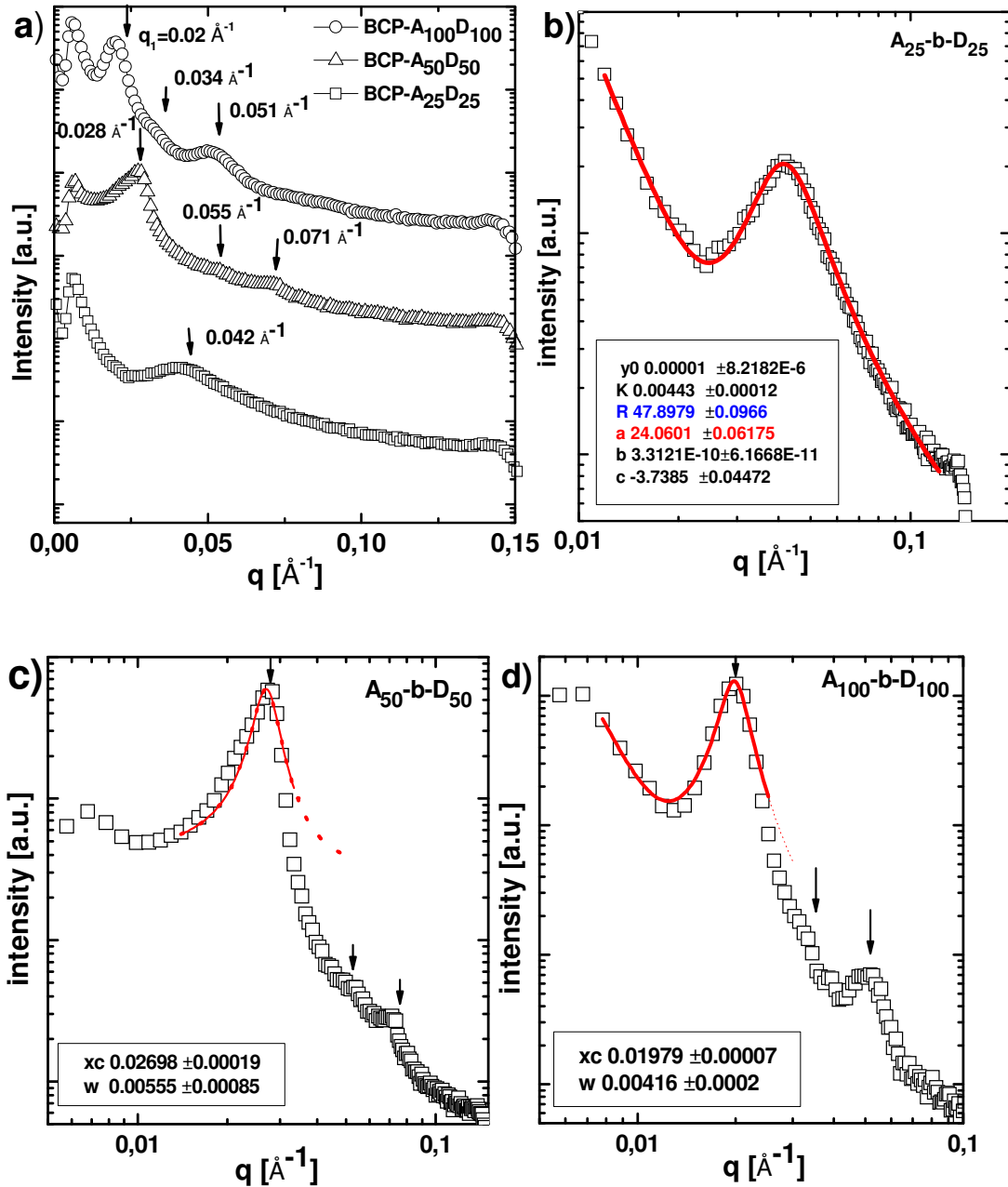


Figure 3.1. a) SAXS of microphase separated A_m -b- D_n measured at infiltration temperature i.e. 150°C (data sets are vertically shifted). b) Leibler fit (red line) for the SAXS data (open squares) of sample A_{25} -b- D_{25} at 150°C to determine χN , SAXS curve fitting for c) A_{50} -b- D_{50} and d) A_{100} -b- D_{100} to determine FWHM (squares are measured points and the red line is from fitting function). Fitted curves (b, c, d) are plotted in double log scale for clarity.

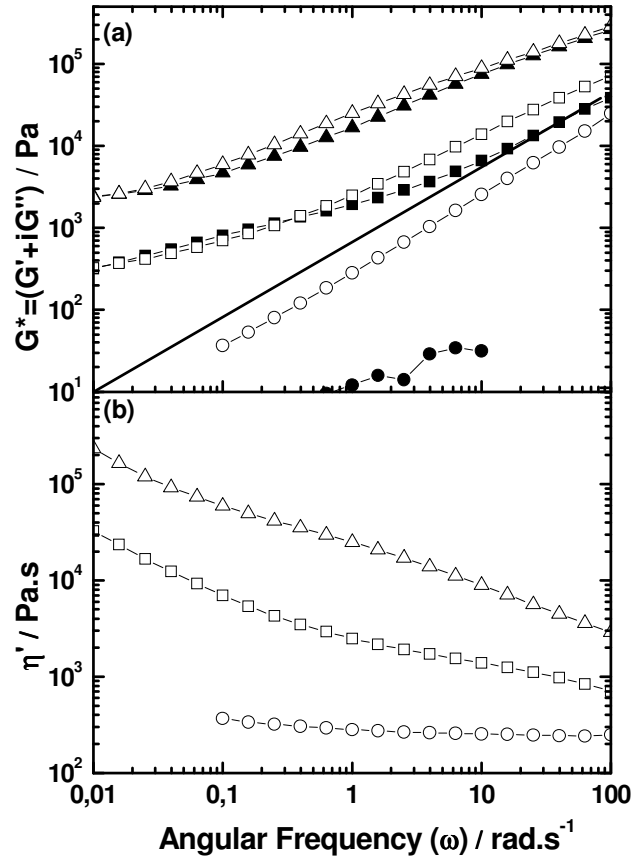


Figure 3.2. Real and imaginary part of the dynamic shear modulus and real part of the dynamic viscosity for the block copolymers A_nD_n measured at 150°C , (a) $G^* = G' + iG''$ vs angular frequency (ω) for $A_{100}\text{-b-}D_{100}$ (triangles, \blacktriangledown), $A_{50}\text{-b-}D_{50}$ (squares, \blacksquare), $A_{25}\text{-b-}D_{25}$ (circles, \bullet). Solid and hollow symbols correspond to storage modulus (G') and loss modulus (G'') respectively. (b) Real part of viscosity ($\eta' = G''/\omega$) vs angular frequency (ω) for $A_{100}\text{-b-}D_{100}$ (triangles, \blacktriangledown), $A_{50}\text{-b-}D_{50}$ (squares, \blacksquare), $A_{25}\text{-b-}D_{25}$ (circles). (note: storage modulus (G') of $A_{25}\text{-b-}D_{25}$ is too low to measure).

These conclusions are confirmed by rheological measurements. Figure 3.2 shows the dynamic shear modulus $G^*(\omega) = G(\omega) + iG''(\omega)$ and the real part of the viscosity $\eta' = G''/\omega$ of the three samples measured at $T = 150^\circ\text{C}$. Only for $A_{25}\text{-b-}D_{25}$ the relation $G'' \sim \omega$ is consistent with terminal flow, while the weaker ω -dependence for the other two samples is typical for an ordered state of the sample^{97, 167} and indicates the absence of terminal flow. G' and G'' values for $A_{100}\text{-b-}D_{100}$ and $A_{50}\text{-b-}D_{50}$ are almost similar and show a frequency (ω) dependency similar to that observed with other block copolymers in ordered state^{167, 168} where $G' \approx G'' \sim \omega^{1/2}$. It is well known that the terminal flow in a

block copolymer melt is hindered due to the ordered structures formed from microphase separation of incompatible blocks.^{5, 97, 168} G' of $A_{25}\text{-b-}D_{25}$ is too low to measure due to the sensitivity limit of the transducer in our rheometer and normally G' scales to ω^2 in the terminal flow region for a disordered BCP melts. Real part of the viscosity (η') for $A_{25}\text{-b-}D_{25}$ is constant and independent of ω , which is indicating the Newtonian flow behavior and hence strengthening the picture of disordered state.

3.4.2. Surface energy characterization of $A_m\text{-b-}D_n$

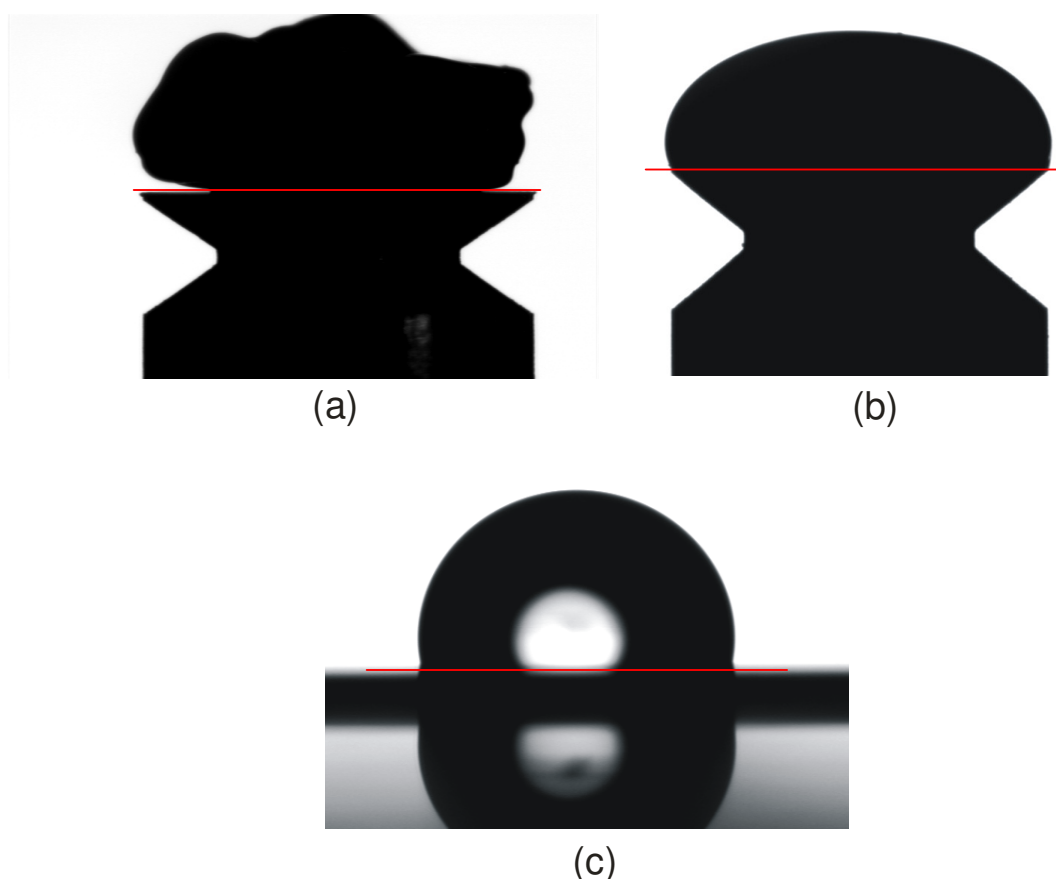


Figure 3.3. (a) $A_{100}\text{-b-}D_{100}$ melt on cylindrical sample holder (stainless steel, $d = 5$ mm) after 6 hours at 150°C , does not make the droplet, (b) $A_{25}\text{-b-}D_{25}$ melt drop used for the determination of the surface tension located on a cylindrical sample holder at 150°C after 30 min. (c) Water droplet deposited on a 300 nm thick $A_{100}\text{-b-}D_{100}$ film at room temperature. The $A_{100}\text{-b-}D_{100}$ film was heated to 150°C for 12 h prior to the contact angle measurements. (Red line in the above figure shows the interface).

Melt drop measurements were carried out for $A_{100}\text{-b-}D_{100}$ and $A_{25}\text{-b-}D_{25}$ to determine the surface energy of the BCP. Figure 3.3a and b shows the melt drop of $A_{100}\text{-b-}D_{100}$ and

$A_{25}\text{-}b\text{-}D_{25}$ located on a cylindrical sample holder (stainless steel, $d = 5$ mm) with a polished surface after heating to 150°C for 30 min. Since $A_{100}\text{-}b\text{-}D_{100}$ melts do not show terminal flow at this temperature, the melt does not obtain a drop shape even after 6 hours kept at 150°C and hence the calculation of surface energy was not possible.¹⁶⁵ Whereas the $A_{25}\text{-}b\text{-}D_{25}$ is disordered and show terminal flow according to SAXS and rheological measurements and forms the melt drop on the sample holder within 15 min of time at 150°C . Thus, the surface energy of $A_{25}\text{-}b\text{-}D_{25}$ was determined and amounted to 15.04 ± 0.44 mN/m. It is reasonable to assume that the surface energies of the other two BCPs with longer chain lengths is not significantly different from the surface energy of $A_{25}\text{-}b\text{-}D_{25}$ as the only difference between them is the chain lengths and microscopic ordered states. Hence, $A_m\text{-}b\text{-}D_n$, have low surface energies and show surface properties comparable to those previously reported for other BCPs containing fluorinated blocks.^{120, 126, 127} The water contact angle at room temperature on about 300 nm thick $A_m\text{-}b\text{-}D_n$ BCP films deposited on Si wafers were measured and amounted to $\approx 105^\circ$ for all the samples (Figure 3.3a), a result indicative of super-hydrophobic behavior.^{134, 169}

3.4.3. Influence of chain length on nanostructure formation

Scanning electron microscopy (SEM) pictures (figure 3.4) shows the cross sections of AAO (pore diameter: 400 nm; pore depth 100 μm) melt infiltrated with $A_{100}\text{-}b\text{-}D_{100}$ at 150°C for ~ 48 hours. During infiltration, a load of 0.7 kg/cm^2 was imposed on the BCP on the surface of the AAO. The uppermost $\sim 10\text{ }\mu\text{m}$ of the pores next to the pore mouths are infiltrated by capillary rise yielding solid rod-like segments clearly discernible in Figure 3.4a. At the pore bottoms, few of the pores are also completely filled with solid BCP rod segments with lengths of a few microns and well developed menisci (Figure 3.4b). The solid BCP entities at the pore mouths and the pore bottoms are connected by tubular segments with lengths of some tens of μm , clearly evidencing the formation of extended $A_{100}\text{-}b\text{-}D_{100}$ precursor films on the pore walls, which is seen clearly in the figure 3.4c showing the tubular segments protruding out of the cross sectioned AAO template somewhere at the middle of the template depth. Removing the residual BCP from the surface of the AAO with a sharp blade partially uncovered the openings of the tubular segments of the $A_{100}\text{-}b\text{-}D_{100}$ 1D nanostructures as depicted in figure 3.4d, presumably because their rod-like segments were pulled out of the pores in the course this treatment.

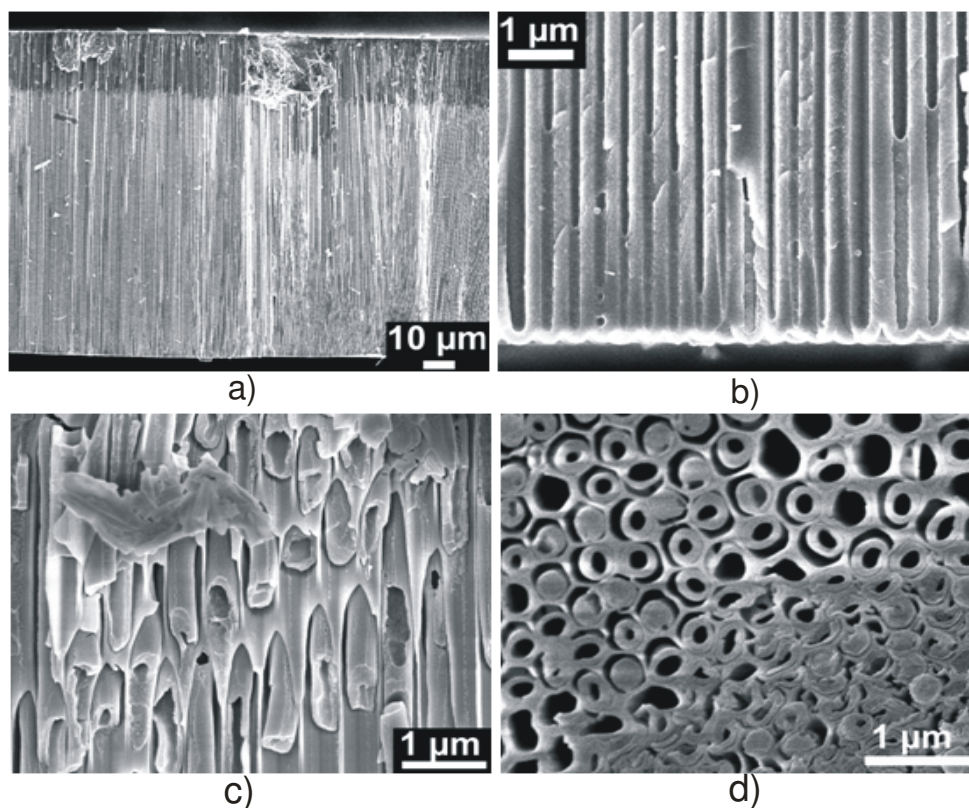


Figure 3.4. SEM pictures of AAO (pore diameter: 400 nm; pore depth 100 μm) infiltrated $A_{100}D_{100}$ at 150 $^{\circ}\text{C}$ for ~ 48 hours. a)-c) Cross sections; a) overview; (b) pore bottoms; (c) detail of the middle portion of the AAO membrane. d) Surface of the AAO membrane after scraping off the residual BCP film with a sharp blade.

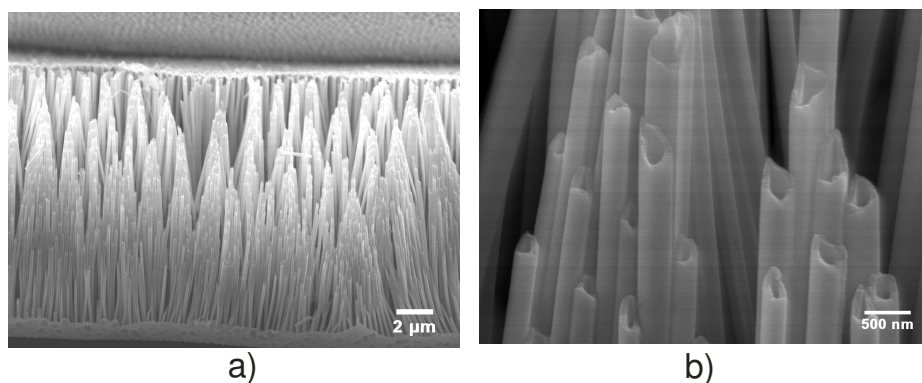


Figure 3.5. SEM images of a) $A_{50}\text{-b-}D_{50}$ annotates protruding out from the AAO after partial etching away of AAO template with KOH, b) zoom or close view clearly showing the freely standing hollow tubular nanostructures.

BCP $A_{50}\text{-b-}D_{50}$ shows the same infiltration behaviour like $A_{100}\text{-b-}D_{100}$ and yields tubular structures; figure 3.5 shows the BCP $A_{50}\text{-b-}D_{50}$ hollow tubular structures standing after

scraping the residual BCP on the template surface and partially etching away the alumina template. This result suggests that the hollow spaces of the tubular segments can be accessed easily. On the other hand upon melt infiltration of BCP $A_{25}\text{-b-D}_{25}$, having shorter chain length and low molecular weight compared to other two polymers, filled the pores completely and furnished nanorods. Figure 3.6 shows the SEM pictures of the cross section of AAO melt infiltrated with $A_{25}\text{-b-D}_{25}$ at 150 °C for ~48 hours. Unlike $A_{100}\text{-b-D}_{100}$, the BCP $A_{25}\text{-b-D}_{25}$ infiltrated throughout the depth of the template is evidenced in the SEM pictures (see figure 3.4a and figure 3.6a). Completely filled solid BCP rods are visible in SEM images taken near to the pore mouth (figure 3.6b), middle (figure 3.6c) and the bottom (figure 3.6d) of the AAO template.

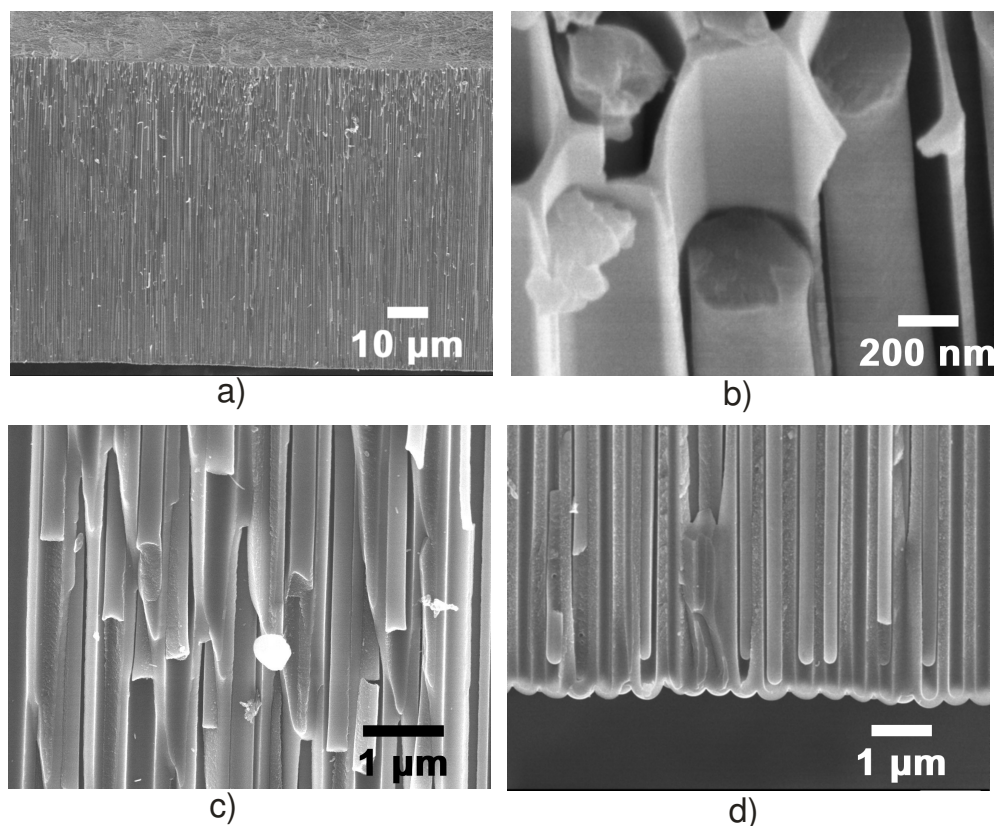


Figure 3.6. SEM images of AAO (pore diameter: 400 nm; pore depth 100 μm) infiltrated $A_{25}\text{-b-D}_{25}$ at 150 °C for ~48 hours. a) Cross sectional overview of complete template; (b) 30° tilt near the pore mouth after scraping the residual BCP on top surface; (c) detail of the middle portion of the AAO membrane. d) Cross section at the pore bottoms of AAO membrane.

An important and interesting point concerns the underlying mechanism of either pore or rod-formation. Infiltration may involve the rapid formation of a precursor film on the

pore walls of the hard template (generating nanotubes) and later the subsequent formation of menisci across the pores at local instabilities⁷³ in the precursor films, (if the precursor film formed is unstable), allowing the complete filling or the slow filling of the pore volume by a solid thread of the molten polymer driven by capillary forces (generating nanorods).^{36-38, 74, 75} For a high surface energy substrate under conditions of complete wetting the first process will usually precede the second.⁷² The time scale on which the instabilities develop or the capillary filling of nanopores occur depends on the viscosity or here more generally on the ability of the infiltrating polymer melt to flow. The observed morphology of the nanostructures (rods or tubes) can now easily be explained on the basis of the mechanical properties of the different copolymers (see figure 3.2). Obviously the formation of a precursor film is not suppressed by the long relaxation times of the microphase separated sample and the fact that pure viscous flow is impossible. Therefore, the two samples with higher molecular weight form nanotubes. Any subsequent process leading to complete filling of the pores either by capillary rise or by instabilities of the thin film covering the pore walls is suppressed or takes a quite longer times as it requires viscous flow. Such processes on the other hand are possible in the low molecular weight sample which shows terminal flow and a moderate viscosity ($\eta \approx 250$ Pa s) in the rheological measurements due to the homogeneous nature of the disordered melt and the lower molecular weight.

3.5.4. BCP Tube wall morphology characterization

TEM images of the released nanotubes clearly shows the mass/thickness contrast to the solid tube wall and their hollow center (see Figure 3.7a and b) confirming the tubular structures. The nanoscopic domain structure of $\mathbf{A}_{100}\text{-b-}\mathbf{D}_{100}$ was probed by transmission electron microscopy (TEM). Fluorine-rich domains consisting of block **D** show higher mass/thickness contrast than domains consisting of block **A**. Hence, the nanoscopic domain structure can be visualized by TEM without further staining. As obvious from the TEM image of an ultrathin slice of bulk $\mathbf{A}_{100}\text{-b-}\mathbf{D}_{100}$ displayed in Figure 3.7c, hexagonally arranged cylinders consisting of component **A** (bright) are embedded in a matrix consisting of component **D** (dark). The apparent period of ~ 30 nm is in line with the SAXS results summarized in Table 3.2. Figure 3.7d shows the TEM image of an ultrathin slice of the solid rod like segments formed near the AAO template pore mouth upon melt infiltration of $\mathbf{A}_{100}\text{-b-}\mathbf{D}_{100}$. The solid rod-like segments clearly exhibit a domain structure similar to that of the bulk BCP that apparently consist of cylindrical **A**

domains appearing bright oriented along the long axes of the A_{100} - b - D_{100} 1D nanostructures surrounded by matrix component D appearing dark.

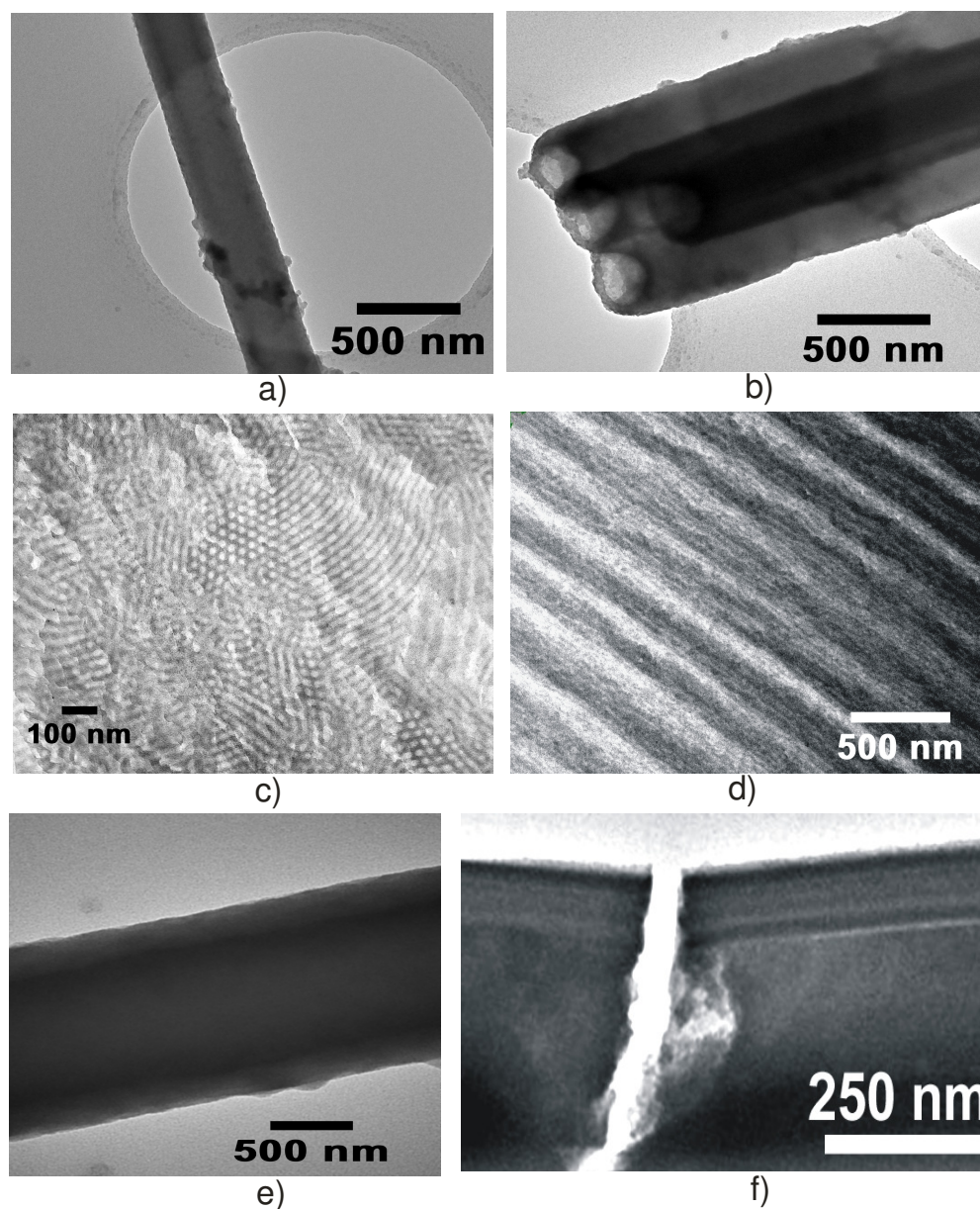


Figure 3.7. TEM images of a-b) released A_{100} - b - D_{100} nanotubes showing darker solid edges and lighter hollow center; c) Ultrathin section of bulk A_{100} - b - D_{100} ; d) sections along rod-like segments embedded in an ultrathin slice; e) top view of an intact tubular segment; f) ultrathin slice containing a section along a tubular segment. The interior of the tube is seen in the lower part, the tube wall/air interface in the upper part of the image. Fluorine-rich areas have higher mass/thickness contrast and appear darker than areas with low fluorine content.

A top view of a tubular segment of an intact $A_{100}\text{-}b\text{-}D_{100}$ 1D nanostructure is shown in Figure 3.7e. A pronounced dark line, which marks the area where the path length of electrons passing the tube wall is maximal, sharply separates an outer rim from the area where the hollow interior of the tube is located. Hence, the inner surface of the tubular segment consists of a **D** lamella appearing dark, which is surrounded by an **A** lamella appearing significantly brighter. Moreover, bright corona-like features discernible at the outer tube surface might indicate that the outermost layer of the tube walls consist of an **A** layer. The overall thickness of the tube wall is ≈ 60 nm, that is, about twice the period of $A_{100}\text{-}b\text{-}D_{100}$ (cf. Table 3.2). However, the contrast pattern in the top view image seen in Figure 3.7e predominantly originates from the path lengths of the electrons passing the tube walls and the curvature of the latter. Therefore, the nanoscopic domain structure of $A_{100}\text{-}b\text{-}D_{100}$ is more obvious from the ultrathin section along a tubular segment displayed in Figure 3.7f. A dark line indicative of a **D** lamella is seen at the inner surface of the tube wall, while close to its outer surface in the uppermost part of Figure 3.7f a second **D** lamella can be identified. Again, the presence of a brighter outermost rim might originate from a layer of **A** blocks segregated to the pore walls of the AAO. The contrast patterns seen in Figure 3.7e and f indicates the phase-transition of the asymmetric norbornene block-copolymer (hexagonal bulk morphology in bulk) into concentric lamellar structure³⁶⁻³⁸ (within the tube/cylindrical confinement) and it is consistent with the notion that the perfluorinated alkyl moieties of the **D** blocks segregated to the polymer/air interface surrounding the interior hollow space of the tube, whereas the polar **A** blocks probably segregated to the outer tube surface adhering to the hydroxyl-terminated pore walls of the AAO. Hence, it is reasonable to assume that the tube walls consist of two concentric **A/D** double lamellae. The preferential segregation of block **D** to polymer/air interface to minimize the overall surface energy also drives the formation of precursor film on pore walls, which is unusual for microphase separated and ordered BCPs.

Homopolymer A_{200} and BCP $A_{50}\text{-}b\text{-}C_{13}$ was also melt infiltrated into 400 nm templates and SEM investigation was conducted. In case of homopolymer infiltration, SEM images showed both tubular structures and completely filled rods and in case of $A_{50}\text{-}b\text{-}C_{13}$ we see the collapsed tubular structures at regular intervals along the length due to the developed melt instabilities. This is may be due to the low viscosity and molecular weight ($M_n=17,200$) of $A_{50}\text{-}b\text{-}C_{13}$ melt.

3.6. Conclusions

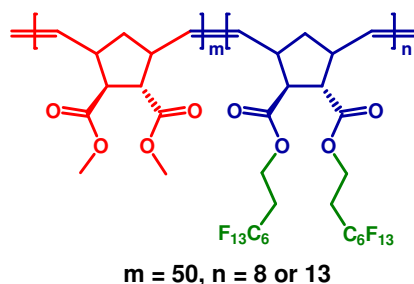
In conclusion, the melt infiltration of specifically designed low surface energy fluorinated norbornene BCPs (poly(**A_m-b-D_n**)) forms precursor film on the AAO pore walls and the solidification of which yields tubular BCP nanostructures, thus enabling us to prepare the BCP nanotubes with a layered wall structure. A change in microscopic state of order of the poly(**A_m-b-D_n**) ($m=n=25, 50, 100$) via changing of the molecular weight allows to control the morphology of the nanostructures, i.e. tubes or rods (tubes for $m=n=50, 100$ or rods for $m=n=25$), as the filling process of AAO pores also depends on the rheological properties of the infiltrating polymer.

Section 4

Hierarchical Nanostructures via Nano- and Micro-phase Separation

4.1. Concept

In this section we discuss the characterization of hierarchical nanostructures in norbornene block copolymers containing semi-fluorinated alkyl side chain. The synthesis of norbornene block copolymers, (poly(A_m -b- C_n)), (see scheme 4.1)), with block-C containing long semi-fluorinated alkyl side chains are described in section 2. The ordering and formation of nanodomains by nanophase separation of side chains in comblike polymers has been observed earlier.^{86, 91, 96, 170} In our block copolymer system similar phenomena of nanophase separation of semi fluorinated alkyl side chains can occur within the confined state of microphase separated block copolymer domains. The phase separated and ordered domains in polymers can be determined by X-ray scattering experiments as they scatter the incident X-rays due to the electronic densities difference between the two phases. Hence, we used X-ray scattering technique to confirm the mesoscopic and nanoscopic domains in our side chain block copolymer systems. The polymer chains in the different domains of phase separated system have independent chain dynamics and relaxation behavior.^{91, 95, 101} Therefore we applied dynamic mechanical analysis (DMA) and dielectric relaxation spectroscopy methods to trace the independent chain relaxations of phase separated domains as a proof for the presence of hierarchical nanostructures in the side chain block copolymers poly(A_m -b- C_n).



Scheme 4.1. General structure of the investigated block copolymers (poly(A_m -b- C_n))

4.2. Characterization methods: Structure and Chain dynamics

X-ray scattering Experiment: X-ray scattering measurements were performed on a small angle instrument assembled by JJ X-rays based on a 2D detector by Bruker Hi-star and a Rigaku rotating anode with focusing optics. Cu-K α radiations with wavelength $\lambda=1.56 \text{ \AA}$ was used for measurements. Instrument was calibrated using silver behenate as a reference material. For temperature dependent measurements Linkam hot stage was used with equilibration time of 15 minutes. Small angle X-ray scattering (SAXS) was measured in the q range of $(0.009 \text{ \AA}^{-1} \leq q \leq 0.15 \text{ \AA}^{-1})$ and intermediate range X-ray scattering was measured in the q range $(0.15 \text{ \AA}^{-1} \leq q \leq 0.60 \text{ \AA}^{-1})$.

Dynamic Mechanical Analysis (DMA): Dynamic shear modulus $G^*=G'+iG''$ was measured using Anton Paar MCR501 instrument. Controlled strain used for the measurement is 0.015%. For construction of the Arrhenius plot, isotherms were measured in the range of 0.1 to 100 rad/s with five points per decade. Equilibration time at each temperature is 180s with the step of 4K. For the temperature scans, a rate of 1K/min was used at a constant frequency of 10 rad/s with point density of 2 points/min. All the measurements were performed in controlled nitrogen atmosphere.

Dielectric Spectroscopy: The dielectric function $\epsilon^*(\omega) = \epsilon'(\omega) - i\epsilon''(\omega)$ was measured using a Novocontrol Alpha analyzer in the frequency range from 10^{-1} to 10^7 Hz. Measurements were performed on films with 25 μm thickness and 20mm diameter with kapton spacers pressed on standard gold plated brass electrodes. Isotherms were measured at temperatures between -120°C and 140°C with a temperature step of 5K.

Differential Scanning Calorimetry(DSC): Perkin Elmer Diamond DSC was used for measurements with the rates of $dT/dt=10\text{K/min}$. Samples with approximately 5mg mass were encapsulated in the standard open pans.

Gel Permeation Chromatography (GPC): Molecular weight distributions were determined by GPC measurements done on a Viscotek VE2001 system using polystyrene standards for conventional external calibration with Viscotek VE3580 refractive index detector. GPC and DSC data for investigated polymers are given in table 4.1.

Table 4.1. Physicochemical properties of investigated polymers.

Sample	M_n (cal) ¹⁾ (g/mol)	M_n (GPC) (g/mol)	PDI	Tg _A (° C)	Tg _C (° C)
Poly (A ₂₀₀)	42,046	40,000	1.17	72.36	-
Poly(A ₅₀ -b-C ₁₃)	21,862	16.400	1.20	69.55	24.76
Poly(A ₅₀ -b-C ₈)	17,492	13.000	1.20	67.39	22

¹⁾Calculated molecular weight

4.3. Results and Discussion

4.3.1. X-ray scattering results: Small angle and Intermediate q range

The microphase separation and its morphology of the main chains of the synthesized block copolymers, Poly(A_m-b-C_n), was analysed by small angle X-ray scattering (SAXS) in the q range of ($0.009 \text{ \AA}^{-1} \leq q \leq 0.15 \text{ \AA}^{-1}$). Figure 4.1a and b shows the SAXS curves for both the block copolymers, A₅₀-b-C₁₃ and A₅₀-b-C₈ respectively, at different temperatures from -50° C to 90° C in the steps of 20° C. The presence of prominent higher order scattering peaks up to fourth order in both the samples is an authentic evidence for the long range and well ordered periodic structures formed due to the microphase separation between the block A and C. In the case of A₅₀-b-C₁₃, we can see a sharp first order scattering peak (q_1) positioned at 0.026 \AA^{-1} corresponding to the long period (d) of 24 nm according to $q = 2\pi/d$ and the relative peak positions of the higher order scattering peaks with q_1 are in the ratio of $1:\sqrt{4}:\sqrt{7}:\sqrt{9}$ suggesting the hexagonally ordered cylindrical structures. Whereas in case of A₅₀-b-C₈ a narrow first order scattering peak (q_1) is positioned at 0.030 relating to the long period (d) of 21 nm with equidistantly spaced higher order peaks in relative to q_1 (1:2:3:4) confirming the lamellar structure. Further the scattering pattern of both the samples does not show clean temperature dependence i.e. there is no significant change in either position or shape of the scattering peaks with the change in temperature, which indicates that the morphology is prevented and our system is far away from T_{ODT}. A change from cylindrical to lamellar morphology upon decreasing the chain length of block C from 13 to 8 indicates the larger volume fraction of C in block copolymer A₅₀-b-C₁₃ and hence it is reasonable to assume the cylinders of A in the matrix of C. Even though the block C having lower

degree of polymerization compared to block A, the larger volume fraction of block C in the block copolymer is accounted from the bulky semi-fluorinated alkyl side chains.

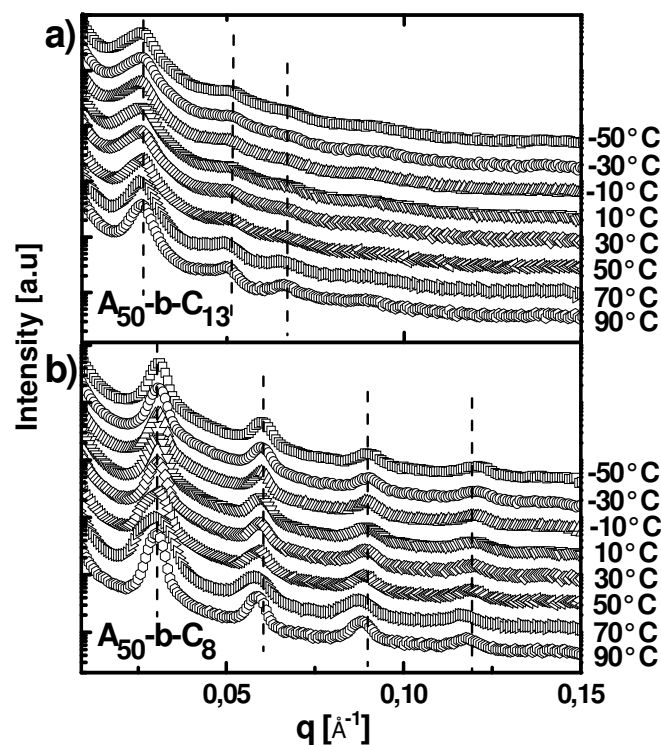


Figure 4.1. Small angle X-ray scattering curves (I vs q) of poly(A_m - b - C_n) at different temperatures are shown. a) A_{50} - b - C_{13} and b) A_{50} - b - C_8 . The data sets are vertically shifted.

The nanophase separation of the semi-fluorinated side chains from the main chain of the block C was evidenced from the X-ray scattering in the intermediate q range ($0.15 \text{ \AA}^{-1} \leq q \leq 0.60 \text{ \AA}^{-1}$). Figure 4.2a and b shows the X-ray scattering data in the intermediate q range for A_{50} - b - C_{13} (asymmetric) and A_{50} - b - C_8 (symmetric) respectively. The heating (-50 to 90°C) and cooling (90°C to -50°C) scans were performed in order to check the temperature dependence. The prepeak at 0.2198 \AA^{-1} , corresponding to $d = 2.9 \text{ nm}$, is seen in both the samples at lower temperatures and up to around 70°C . This prepeak is characteristic of the nanodomain (2.9 nm) formed by the nanophase separation of semi-fluorinated alkyl side chains in block C from the main chain of the block copolymer and these kind of alkyl side chain nanophase separation has been earlier observed in polymers and oligomers.^{86, 91} The prepeak gradually vanishes upon heating above 70°C and reappears upon cooling back below 70°C (figure 4.2). The reappearance of the

prepeak upon cooling is suggesting that the nanophase separation or demixing of fluorinated alkyl side chains from the main polymer chain sets in below 70° C and mixing occurs above this temperature.

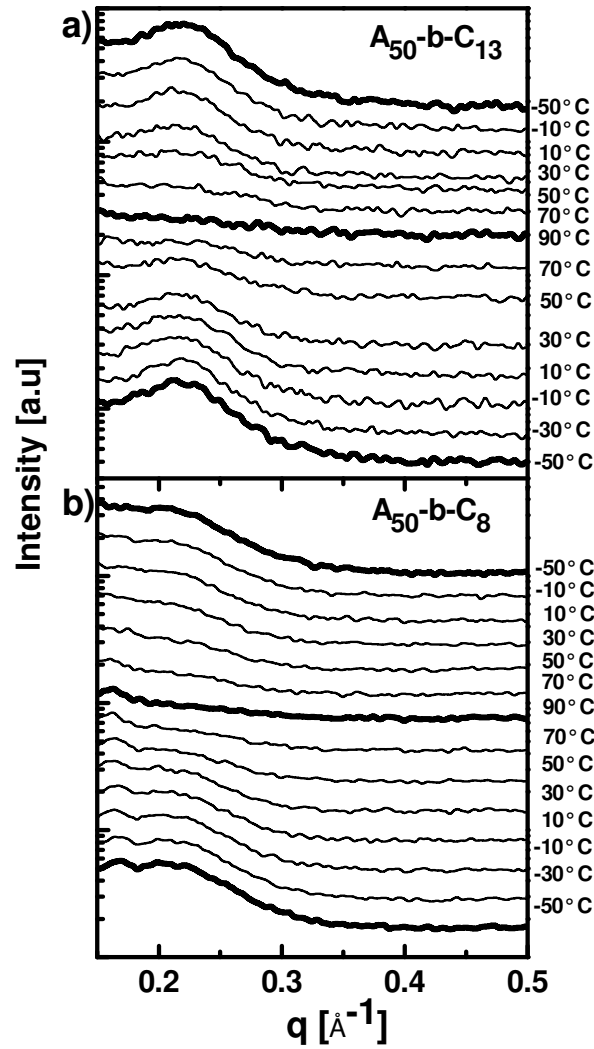


Figure 4.2. X-ray scattering curves (I vs q) in an intermediate q range ($0.15 \text{ \AA}^{-1} \leq q \leq 0.60 \text{ \AA}^{-1}$) for a) $A_{50}\text{-b-C}_{13}$ and b) $A_{50}\text{-b-C}_8$. Heating (-50° C to 90° C) followed by cooling (90° C to -50° C) scans are shown.

4.3.2. Dynamic mechanical analysis (DMA)

Dynamic mechanical analysis was conducted in shear mode and the shear complex modulus (G^*), i.e. $G^*(T) = G'(T) + iG''(T)$ where G' is storage modulus and G'' is loss modulus, for homopolymer A_{200} , block copolymers $A_{50}\text{-b-C}_{13}$ and $A_{50}\text{-b-C}_8$ is shown in figure 4.3. Two independent relaxation processes at around -115° C and 77° C are

evident (figure 4.3a) in case of homopolymer A. The low temperature process at -115°C corresponds to the ' β ' process i.e. localized motions of the norbornene monomeric units, whereas the relaxation process at 75°C relates to ' α ' process of the norbornene main chain caused by the co-operative motions of the complete monomeric unit. The ' α ' process obtained by DMA is comparable to the results obtained by DSC (see table 4.1).

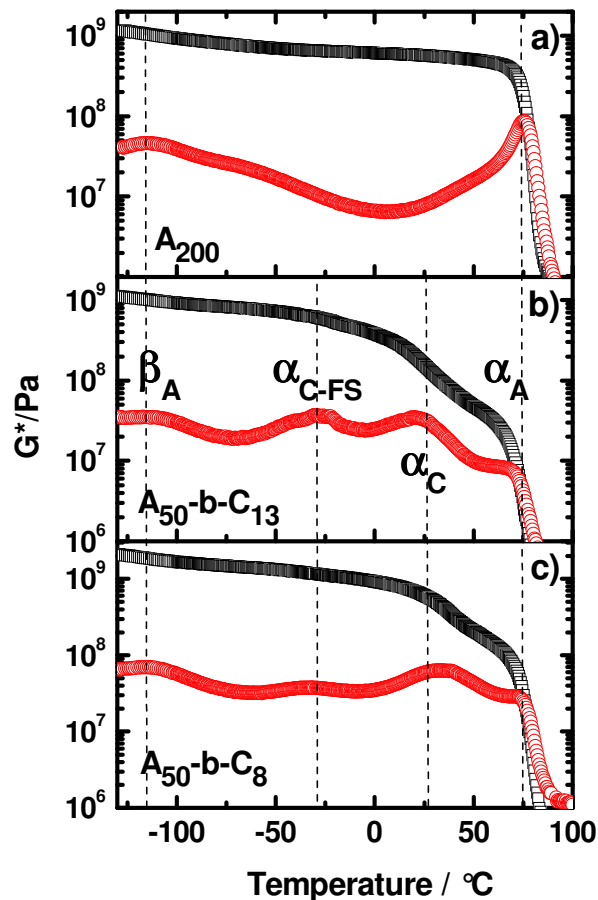


Figure 4.3. Dynamic Mechanical Thermal Analysis (DMTA) data ($G^* = G' + iG''$) vs temperature (T) is shown for a) homopolymer A_{200} , b) $A_{50-b-C_{13}}$ and c) A_{50-b-C_8} . Black open squares and red open circles corresponds to G' and G'' respectively. Vertical dashed lines show different relaxation process.

The block copolymers $A_{50-b-C_{13}}$ and A_{50-b-C_8} exhibits four different relaxation processes (figure 4.3b, c) at around -115°C , -29°C , 22°C and 77°C . The relaxation at 77°C , ' α ' process, originating from the polymer A chain and ' β ' process of norbornene monomeric units at -120°C is already known from the DMA measurements of neat homopolymer A. Hence, it is obvious that the relaxation processes seen at -29°C and

22° C are originated from polymer C chain. From DSC measurements of Poly(A_m-b-C_n) block copolymers we know that the glass transition (T_g) of the block C is around 24° C (c.f table 4.1) and it is so reasonable to say that the relaxation process at 22° C is the 'α' process of block C. The glass transition of block C is reduced in comparison to block A due to the internal plasticization effect of flexible side chains as predicted by Heijboer¹⁶² for PnAMAs. The other low temperature relaxation process at -29° C is related to the cooperative motions or 'α_{FS}' process with in the nanophase separated fluorinated alky side chains (FS). This relaxation peak gives an additional confirmation for the presence of nanoscopic domains within the microphase separated structure. Independent relaxation data for homopolymer C was not accessible as synthesis of homopolymer C is not feasible due to the solubility limit.

4.3.3. Dielectric Relaxation Spectroscopy results

Considering the molecular structure of the block copolymer (Scheme 4.1), presence of polar groups (COO) forms the dielectric active centers⁹¹ and hence dielectric relaxation measurements could be performed on these systems. Dielectric spectroscopy is widely used to study the relaxation behavior of polymeric materials, small molecules and liquid crystalline materials.¹⁷¹ It detects dipole fluctuations on different time scales seen in dielectric spectra as relaxation processes and also provides useful information related to mobility of charge carriers. Differences in electro-negativity between covalently bonded atoms lead to a permanent electric dipole moment. The dynamics of molecules having significant permanent dipole moments can be studied by dielectric spectroscopy. However, molecules having permanent dipole moment does not show macroscopic polarization in the absence of external electric field. When an electric field (static or alternating) is applied to such a type of molecules the dipoles can orient in the direction of applied electric field leading to dipolar polarization of the entire sample. The ability of the dipoles to reorient depending on temperature and frequency or time is detectable by dielectric spectroscopy, which gives the information about the relaxation behavior of the sample.¹⁷¹ In case of DMA sinusoidal strain is applied and the stress relaxation is measured to follow the chain dynamics, but here in case of dielectric spectroscopy the alternating voltage (V) is applied on the sample and the total current (I) through the capacitor with a phase shift (δ) is measured, from which the total impedance in turn the complex permittivity (ε*) is obtained. In our polymers, the main dipole component is on

a flexible side chains and hence the dynamics and relaxation behavior of the side chains can be probed via dielectric measurements.

Figure 4.4 shows the complex permittivity (ϵ^*), i.e. $\epsilon^*(T) = \epsilon'(T) - i\epsilon''(T)$ for homopolymer A_{200} , block copolymers $A_{50}\text{-b-}C_{13}$ and $A_{50}\text{-b-}C_8$. In case of A_{200} two relaxation loss peaks are observed, at low temperature corresponding to the β process centered at -105°C and α process of the complete monomeric unit of A at 67°C . Correspondingly two steps are seen in $\epsilon'(T)$. Figure 4.4b and c shows $\epsilon^*(T)$ for $A_{50}\text{-b-}C_{13}$ and $A_{50}\text{-b-}C_8$ block copolymers respectively. Here in $\epsilon''(T)$ two merged relaxation processes are observed at -105°C , and -29°C . The former belongs to the block A as evidenced from the neat homopolymer A and the later is α relaxation process of fluorinated side chains. A smeared out and broad relaxation peak is observed in the temperature range 25 to 70°C originating from the overlap of α relaxation processes of both block A and C main chain. Results are in accordance to the DMA results which is again indicating the independent dynamics of the phase separated regimes strengthening the picture predicted.

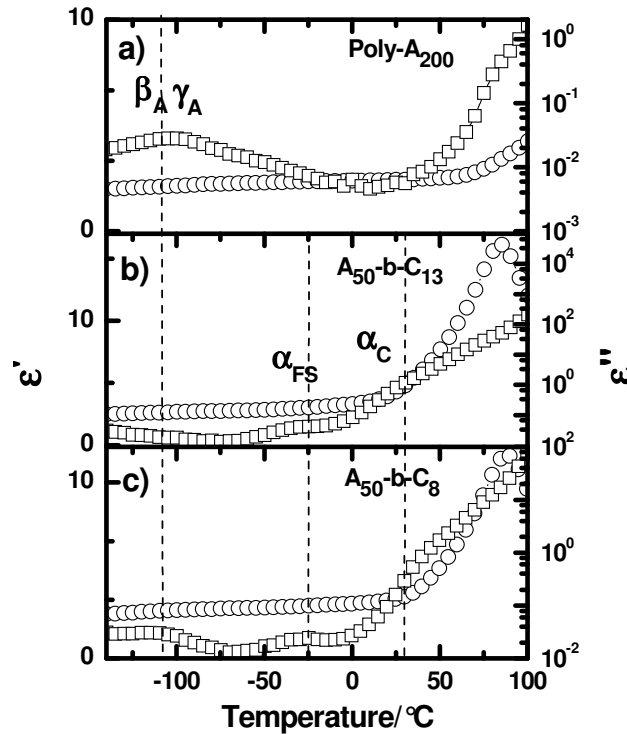


Figure 4.4. Dielectric permittivity ($\epsilon^* = \epsilon' - i\epsilon''$) vs temperature (T) is shown for a) homopolymer A_{200} , b) $A_{50}\text{-b-}C_{13}$ and c) $A_{50}\text{-b-}C_8$. Open circles and open squares

corresponds to ϵ' and ϵ'' respectively. The vertical dashed lines show different relaxation process.

Dielectric spectroscopy frequency measurements on our samples have been performed in a wide frequency and temperature range (figure 4.5). We will focus here on results obtained at low temperatures ($-140\text{ }^{\circ}\text{C} \leq T \leq 10\text{ }^{\circ}\text{C}$) showing the secondary relaxations β and γ as well as the α_{FS} process. The dielectric spectra measured at high temperatures are dominated by strong conductivity contributions. Thus, the α_{A} and α_{FS} processes are practically hidden or only seen as a weak shoulder which cannot be evaluated. The low temperature isotherms $\epsilon''(\omega)$ for the homopolymer A_{200} show a very broad and weak relaxation peak which shifts expectedly to higher frequencies if the temperature increases (Figure 4.5a).

Its peak width decreases for higher temperatures. Based on a comparison of the peak maxima positions with those taken from the shear curves and a more detailed inspection of the peak width as function of temperature one can conclude that this peak contains contributions from two secondary relaxation processes, β and γ , indicating the appearance of two different types of localized motions in glassy A_{200} . It is not possible in this case to de-convolute the contributions of both relaxation processes. Thus, we will only incorporate the maximum positions of the β process appearing at low frequencies in the further discussion. The peak maxima were taken manually from the ϵ'' isotherms (Figure 4.5).

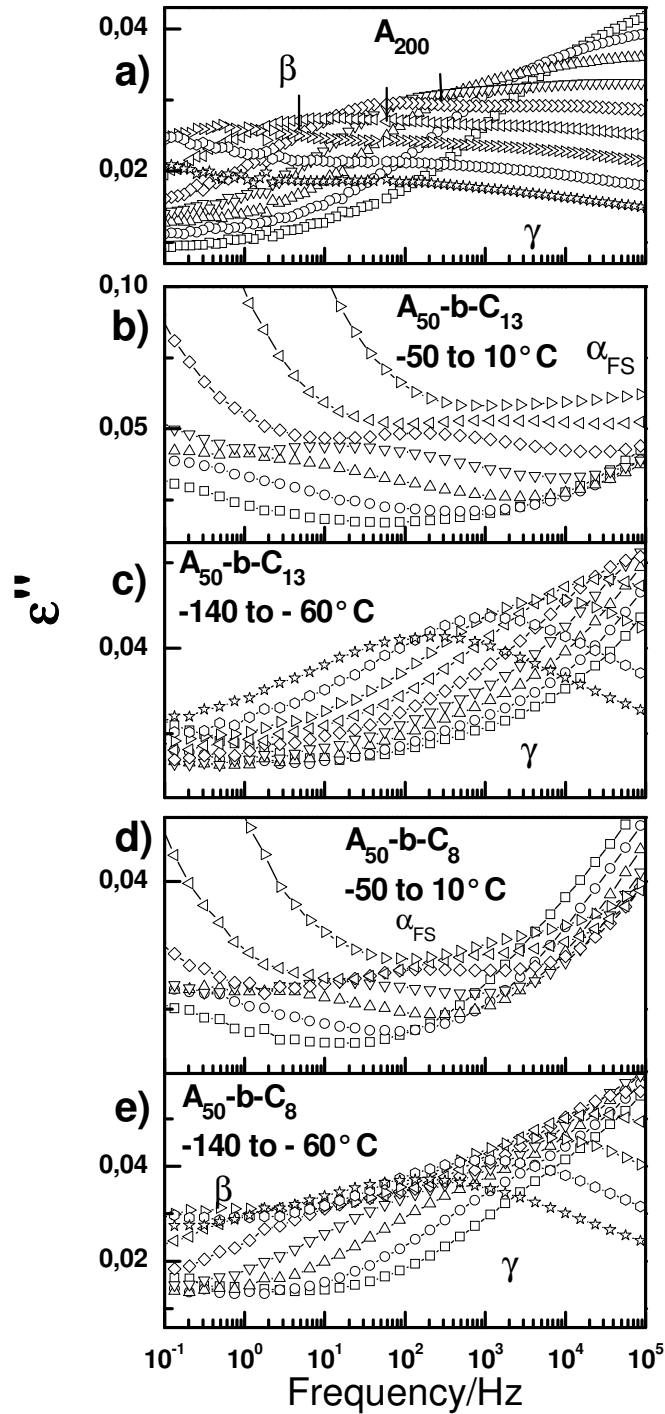


Figure 4.5. Dielectric relaxation spectroscopy isotherms (ϵ'' vs freq) for a) Homopolymer A_{200} from -140 to -60°C , b) and D) block copolymer $A_{50}\text{-b-C}_{13}$ from -50 to 10°C and -140 to -60°C respectively, d) and e) block copolymer $A_{50}\text{-b-C}_8$ from -50 to 10°C and -140 to -60°C respectively.

Isotherms for the block copolymer $\mathbf{A}_{50}\text{-b-}\mathbf{C}_{13}$ measured at comparable temperatures are given in Figure 4.5c. The results show clearly that the shape of the peak has changed. The peak maximum appears now at the high frequency end of the broad peak and β contributions dominating in the \mathbf{A}_{200} homopolymer seem to be strongly suppressed. The γ process dominates obviously in case of this block copolymer. Similar behavior with slightly stronger contributions of the β process is observed for the $\mathbf{A}_{50}\text{-b-}\mathbf{C}_8$ block copolymer (Figure 4.5e). Such a significant change in the dielectric spectrum is somehow surprising since there are only 13 or 8 monomeric units in the \mathbf{C} block as compared to 50 units in the \mathbf{A} blocks. However, one has to take into account that the dielectric signals are tiny and that the fluorinated side chains of the \mathbf{C} block are quite long. Obviously the incorporation of the fluorinated side chains amplifies the γ relaxation process and suppresses the β relaxation. This is interesting since the main chain of \mathbf{A} and \mathbf{C} blocks are identical. The only difference between both monomers is the long partly fluorinated side chain carrying only a small dipole but contributing significantly to the volume of the \mathbf{C} block. It should be mentioned that the total relaxation strength $\Delta\epsilon_{\beta\gamma}$ of the merged-in β and γ processes for the homopolymer and both block copolymers are similar. This finding seems to be in line with the fact that the main chains of \mathbf{A} and \mathbf{C} block carry the same dipole moment per unit. However, it cannot be excluded that a new relaxation process sitting on top of the γ relaxation appears in the side chains of the \mathbf{C} block although this seems to be unlikely.

An α_{FS} process is observed in the dielectric data at intermediate temperatures ($-50\text{ }^\circ\text{C} \leq T \leq 10\text{ }^\circ\text{C}$) in accordance with shear data for both block copolymers (Figures 4.5b and d). According to our previous discussion, this process should reflect motions within nanodomains formed by aggregated side chains of the \mathbf{C} block. The small dielectric relaxation strength $\Delta\epsilon_{\alpha_{\text{FS}}}$ and the temperature dependence of the relaxation frequency ω_{osc} which corresponds to that obtained for the α_{FS} process in shear data (see figure 4.6) fit to this interpretation. Note that it is impossible to get quantitative information about the temperature dependence of relaxation strength $\Delta\epsilon_{\alpha_{\text{FS}}}$ and shape for the α_{FS} peak since it is located in the valley between the α_{C} and $\beta\gamma$ peaks. In this frequency range all four relaxation processes do superimpose. Clear is that the α_{FS} peak moves out of the measuring frequency window at around $10\text{ }^\circ\text{C}$ (figure 4.5c and e), i.e., significantly below

that temperature where the pre-peak disappears in the diffraction pattern as shown in Figure 4.2a and b).

An Arrhenius plot compiling the obtained information about the relaxation behavior of all three investigated polymers is given in Figure 4.6. Five relaxation processes are observed for both block copolymers, $A_{50-b-C_{13}}$ and A_{50-b-C_8} , namely the α_A , α_C , α_{FS} , β and γ processes. The α_C and α_{FS} relaxations appear only in the **C** block and have not been found for the A_{200} homopolymer. The results from shear and dielectric spectroscopy do basically coincide. Small shifts of the order of half a decade between the loss maxima positions in dielectric and shear curves might be due to the fact the both methods measure different susceptibilities and accordingly also different fluctuations.^{172, 173} Note, that the frequency temperature position of all relaxation processes is practically independent on the block copolymer morphology and nearly identical for $A_{50-b-C_{13}}$ and A_{50-b-C_8} samples.

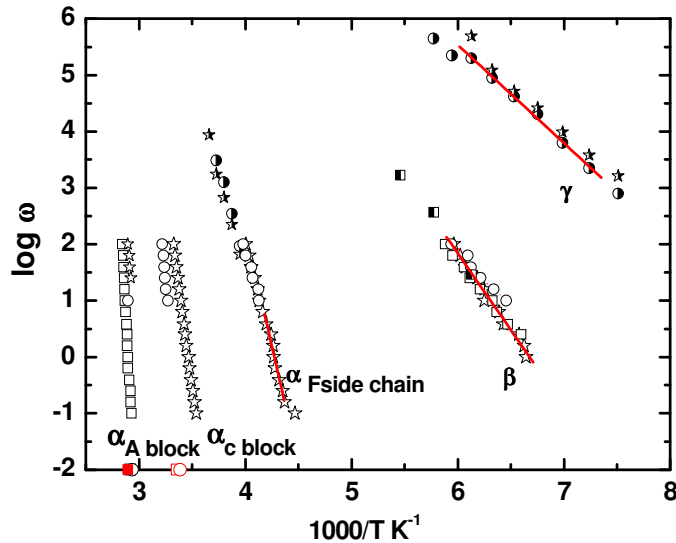


Figure 4.6. Arrhenius plot for the A_{200} homopolymer (squares) and the block copolymers $A_{50-b-C_{13}}$ (stars) and A_{50-b-C_8} (circles) obtained from peak maxima positions of shear isochrones (open symbols) and dielectric isotherms (half filled symbols). The five different relaxation processes (α_A , α_C , α_{FS} , β , γ) appearing in these samples are labeled. DSC glass temperatures from scans with a heating rate of 10 K/min (red squares) are shown for comparison.

The dynamic glass transition α_A of the **A** block in both microphase-separated block copolymers corresponds to that in homopolymer A_{200} with the same microstructure but higher molecular weight. The dynamic glass transition α_C of the **C** block, with the same

main chain as the **A** block but long fluorinated side chains attached to it, appears at lower temperatures. The observed reduction of the relaxation temperatures may be due to internal plasticization effects as known for polymers with long alkyl groups.^{95, 162} The glass temperatures from DSC scans with a heating rate of 10 K/min are also in good agreement with the extrapolated α traces for **A** and **C** blocks assuming that the relaxation time at T_g is approximately 100 s. Interestingly, the steepness indices $m = -\text{dlog}\omega/\text{d}(T_g/T)|_{T=T_g}$ ¹⁷⁴ of both dynamic glass transitions, α_A and α_C , seem to be quite high of the order of $m_{\alpha A} = 136.12$ and $m_{\alpha C} = 47.84$. These m values are extremely large and close to that for most fragile glasses reported in the literature.¹⁷⁴

The β and γ processes in our system show the typical features of an ordinary secondary relaxation process. Their temperature dependence can be described by an Arrhenius law $\omega = \Omega \exp(-E_A/kT)$ with high temperature limits for the relaxation frequencies which are in both cases $\Omega \sim 10^{15}$ rad/s and activation energies which are $E_{A,\beta} = 18.67$ J/mol and $E_{A,\gamma} = 13.32$ J/mol for the β and γ processes, respectively. In accordance with the discussion in Ref.¹⁷⁵ a large steepness indices $m_{\alpha A}$ and $m_{\alpha C}$ are accompanied by a very high $\alpha\beta$ (and $\alpha\gamma$) crossover frequencies, $\omega_{\alpha\beta}$ (and $\omega_{\alpha\gamma}$), related to that point in the Arrhenius plot where the extrapolated traces of α and β (α and γ) process would merge.

More unusual is the temperature dependence of the α_{FS} process. There are clear indications for a non-Arrhenius-like behavior although the α_{FS} trace appears linear in the Arrhenius plot in the accessible frequency window. However, an Arrhenius fit gives an apparent activation energy of about $E_{FS,\alpha} = 61.26$ J/mol but a limiting frequency Ω of about 10^{31} rad/s. This value is unphysical and indicates that the slope of the α_{FS} trace should change at higher temperatures corresponding to a non-Arrhenius-like temperature dependence. The steepness index calculated for the α_{FS} process is $m_{FS} \sim 30.45$ corresponding to that of a relatively strong glass. In case of Arrhenius-like behavior one would expect 16. Similar behavior has been reported for the α_{PE} process in self-assembled alkyl nanodomains reported for various nanophase-separated side chain polymers containing long alkyl groups.^{91, 95} We conclude that the α_{FS} process shows indeed typical features of a dynamic glass transition and reflects most likely cooperative motions in nanodomains formed by aggregated side chains of the partly fluorinated **C** block.

4.3.4. Discussion on hierarchy of length scales

The presented results show clearly that the investigated, Poly(**A**_m-b-**C**_n) copolymers are self-assembled systems with a hierarchy of length scales in the nanometer range. Classical microphase separation of incompatible **A** and **C** blocks leads to a large scale structure with long spacing of about 24 nm while nanophase separation of main and side chains in the **C** domains results in an internal structure with typical periodicities d_{nps} of about 2.9 nm. Like in the side chain polymers containing long alkyl groups, nanophase separation of the **C** block with long partly fluorinated side chains is indicated by (i) a pre-peak in the range $q \sim 0.2198 \text{ \AA}^{-1}$ and (ii) a main chain independent dynamics (α_{FS}) in the side chain domains showing a non-Arrhenius-like temperature dependence. Obviously, nanophase separation can also occur under confinement, i.e., in self-assembled **C** block domains which are only 10 times larger than d_{nps} . The situation in the hierarchically structured block copolymer with cylindrical morphology (**A**₅₀-b-**C**₁₃) should be similar to that sketched in Figure 4.7. Note, that the backbones of the **C** block are aligned basically perpendicular to the interfaces between both microphases and that the fluorinated side chains are non-interdigitated. Only under this condition one can explain the observed d_{nps} (2.9 nm) values which are nearly twice larger than the extended length (1.41 nm) of the partly fluorinated side chains of the **C** block. Similar structures have been proposed for other block copolymers containing one component being a polymer with long side chains. One can conclude that the two structure formation mechanisms in such systems can occur more or less independently. Such systems can optimise most likely their packing on two different length scales in parallel since the competition between both mechanisms is limited, i.e., the side chain polymer component (block **C**) can manage to nanophase separate like under bulk conditions. In this respect, the situation might be different from that in microphase-separated block copolymers containing crystallisable components like polyethylene or polyethyleneoxide.¹⁷⁶⁻¹⁷⁸ In this case there is surely a competition of both structure formation mechanisms, micro phase separation and crystallization, since the thickness of the folded crystalline lamellae is typically similar to the size of the domains formed due to microphase separation. Hence crystallization can destroy the original block copolymer morphology and strong non-equilibrium effects do appear.¹⁷⁹⁻¹⁸² The coexistence of two structure formation mechanisms which do not strongly compete like in our hierarchically structured block copolymers might be a useful strategy to design functional materials which are close to

equilibrium but able to combine the properties of individual domains with different dimensions. Note, that nanophase separated side chain polymers containing alkyl groups of different length are materials with truly predictable structure-property relations. Damping can be introduced in a controlled way since the frequency temperature position of the α_{PE} process in the alkyl nanodomains depends systematically on the side chains length (and nanodomain d_{nps}) but not on the main chain properties.^{91, 95} Similar behavior would be expected for comb-like polymers in the nanophase-separated state containing other side chains, e.g. long partly fluorinated sequences. In combination with a systematic variation of the second block this can be used to fine tune the mechanical properties of self-assembled systems with hierarchical structure. Other properties of such polymers might be optimised following the same strategy.

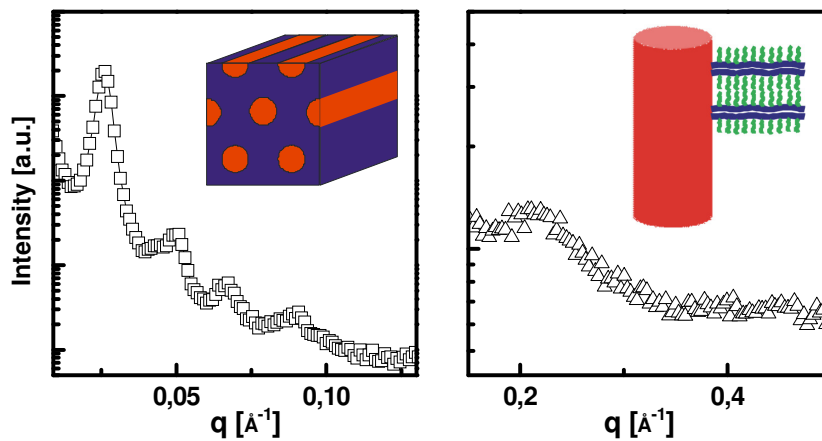


Figure 4.7. X-ray scattering curves at small and intermediate q range for $A_{50}\text{-}b\text{-}C_{13}$. The insets in the graph shows the schematic pictures of microphase separated cylindrical morphology and the nanodomain of semi-fluorinated side chains (green).

4.3.5. Temperature dependency of nanophase separation

An interesting finding of this work is that the pre-peak indicating the nanophase separation in the **C** block connected with an aggregation of long partly fluorinated side chains shows obviously significant temperature dependence. The pre-peak broadens during heating, disappears finally at temperatures around $T_c \sim 90^\circ\text{C}$ and reappears again during cooling (figure 4.2). This observation can be interpreted as an indication for a transition from the nanophase-separated state to a de-mixed state without nanophase separated main and side chain domains. A similar behavior of the pre-peak has been

reported for other block copolymers with partly fluorinated side chains near 70°C ⁸⁵ but never observed to our knowledge for comb-like polymers containing long alkyl groups. The latter show usually a well pronounced pre-peak until degradation starts to appear.⁹⁶ Hence, systems with partly fluorinated side chains could be a suitable model system to study the order-to-disorder transition in nanophase-separated side chain polymers.

A very first evaluation of the temperature dependence of pre-peak intensity I_{FS} and pre-width w_{FS} for the $\text{A}_{50}\text{-b-C}_{13}$ sample (cf. Figure 4.8a and b) shows that there are indeed similarities to the behaviour of microphase-separated block copolymers close to T_{ODT} . The plot I_{FS}^{-1} vs. T^{-1} in Figure 4.8a shows indications for two regions with distinguishable temperature dependence. The reciprocal intensity I_{FS}^{-1} , as obtained from the fitting the pre-peak using allometric Lorentz function, decreases significantly with increasing T^{-1} below 3.0 K^{-1} and is constant at larger reciprocal temperatures. The transition between both regions is at 3.3 K^{-1} corresponding to $\sim 31^{\circ} \text{ C}$ may indicate something like a transition temperature T_{msc} for the nanophase separated side chain polymer used as block C in our systems. Below T_{msc} main and side chains are well separated and above both subunits are relatively well mixed. A similar transition at T_{msc} is indicated if the peak width w_{FS} is plotted vs. T^{-1} (Figure 4.8b). The peak width w_{FS} is relatively small and constant above T_{msc}^{-1} while it seemingly increases for T^{-1} values below. In general the behavior of the pre-peak remembers to well known features of the main peak in scattering pattern of microphase-separated block copolymers close to T_{ODT} .^{164, 183} In these systems the peak intensity also decreases roughly proportional to the mean field prediction $I^{-1} \sim T^{-1}$ above T_{ODT} accompanied by a significant peak broadening.

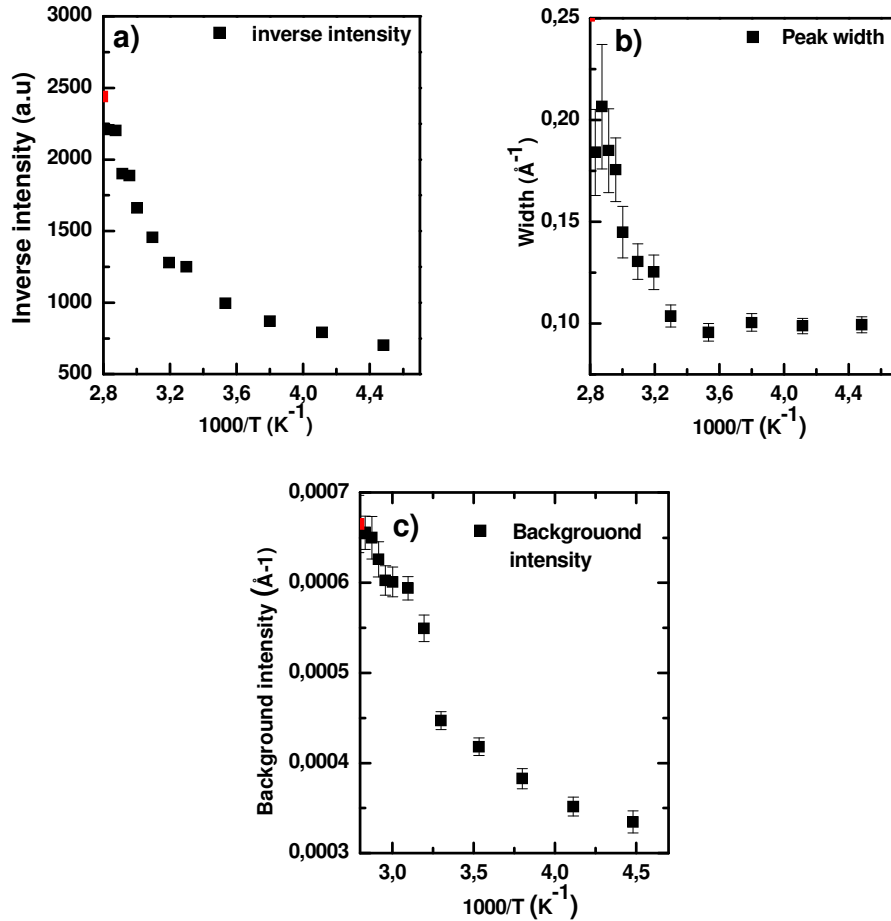


Figure 4.8. Quantitative evaluation of temperature dependency of X-ray scattering pre-peak of $A_{50}\text{-}b\text{-}C_{13}$. a) Inverse pre-peak intensity (I_{FS}^{-1}) vs inverse temperature (T^{-1}) b) pre-peak width (w_{FS}) vs inverse temperature (T^{-1}) and c) scattering background intensity vs inverse temperature.

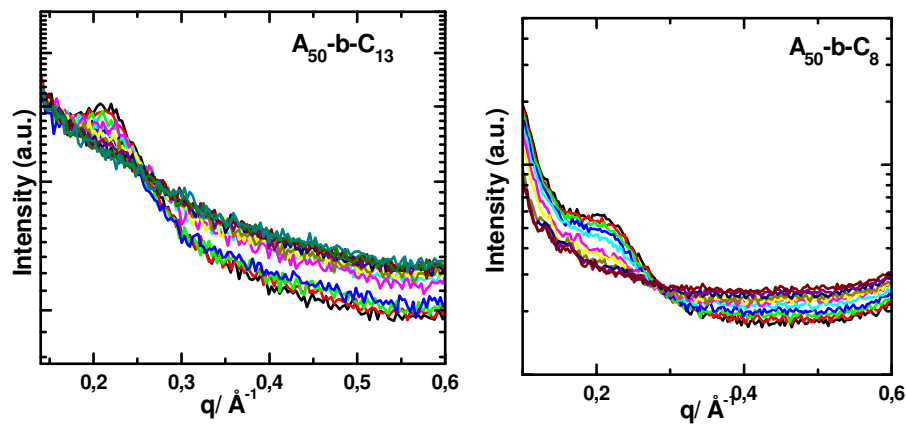


Figure 4.9. Overlay of X-ray scattering curves at different temperatures in intermediate q range, where pre-peak for nanodomain is seen, for a) $A_{50}\text{-}b\text{-}C_{13}$ and b) $A_{50}\text{-}b\text{-}C_8$.

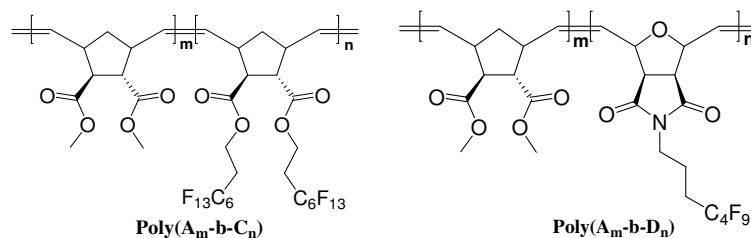
However, we notice a sudden jump or increase in the background scattering intensity at the same temperature ($\sim 31^\circ\text{C}$) (figure 4.8c) where the pre-peak intensity and width changes, which also coincides with the glass transition temperature (T_g) of side chains bearing block C. Figure 4.9 shows the overlay of pre-peak scattering curves at different temperatures. At lower temperatures below 30°C , the pre-peak at $q \sim 0.2198\text{ \AA}^{-1}$ is clearly visible whereas at higher temperatures the pre-peak disappears and the absolute background intensity at higher q ($0.4\text{-}0.6\text{ \AA}^{-1}$) increases drastically. The change in compressibility factor or volume expansion of block C, as it traverse through its T_g , could influence the scattering intensity due to temperature dependent density fluctuations between the phases in BCPs.¹⁸⁴ The pre-peak intensity may be suppressed as a result of decrease in the scattering contrast between the side chain nanodomains and the block C main chain domains due to the density fluctuations. This leads to the speculation that the suppressed pre-peak may be simply submerged in the increased background intensity and not visible anymore. Hence, the temperature dependency of pre-peak intensity and width in this case is not sufficient enough to confirm the transition from de-mixed to mixed state of side chains and main chains of block C. Unfortunately, a theory which describes the phase behavior of nanophase separated side chain polymers quantitatively is still missing. From the experimental point of view it seems to be of special interest whether or not the indications for a transition temperature T_{msc} in the scattering data are supported by changes in the relaxation behavior. This would be expected in the framework of the nanophase separation picture. In particular, the α_{SC} process interpreted as reflection of an independent dynamics within self-assembled side chain domains should disappear or change qualitatively above T_{msc} . For the block copolymers studied in this work the α_{SC} process is unfortunately inaccessible in dielectric spectra measured near T_{msc} as it is outside the frequency window and superimposing with other relaxation processes. We think that the open questions mentioned above should be in the focus of further investigations on partly fluorinated side chain polymers. Such studies may contribute to a better understanding of nanophase separation effects in side chain polymers which are still not well describable and predictable based on the knowledge of their microstructure.

4.4. Conclusions

In conclusion, block copolymer Poly(**A**_m-b-**C**_n) (m=50, n=8 or 13) containing the semi-fluorinated long alkyl side chains exhibit the self-assembled hierarchical nanostructures. The presence of prominent scattering peaks in smaller q range confirms the mesoscopic domains (24 nm, primary structures) formed from microphase separation of incompatible block **A** and **C**, whereas the pre-peak at $q \sim 0.2198 \text{ \AA}^{-1}$ confirms the nanodomains ($d_{\text{np}}=2.9 \text{ nm}$) of side chains confined within the block **C** domains as secondary structures. Further the detailed study of side chain dynamics and relaxation behavior via DMA and dielectric relaxation spectroscopy, revealed a main chain independent dynamics (α_{FS}) in the side chain domains showing a non-Arrhenius-like temperature dependence, confirmed the nanoscopic side chain domains and structural hierarchy.

Section 5. Summary

Summed up, (+/-)-*endo,exo*-bicyclo[2,2,1]-hept-5-ene-2,3-dicarboxylic acid-bis-O-methyl ester (monomer **A**) and (+/-)-*endo,exo*[2.2.1] bicyclo-2-ene-5,6-dicarboxylic acid-bis(3,3,4,4,5,5,6,6,7,7,8,8,8-tridecafluorooctyl) ester (monomer **C**) were synthesized by Diels-Alder reaction of cyclopentadiene and dicarboxylic acid with subsequent acylation and esterification using respective alcohols. (+/-)-*exo*-*N*-(4,4,5,5,6,6,7,7,7-nonafluoroheptyl)-10-oxa-4-azatricyclodec-8-ene-3,5-dione (monomer **D**) was synthesized from cyclo-addition reaction of furan and maleimide with subsequent substitution of fluorinated bromo-compound. The systematic study of block copolymerization and crossover reaction of monomer **A** with monomer **C** or **D**, using Grubbs 1st and 3rd generation catalyst, via classical ¹H-NMR and GPC reveals controlled polymerization and complete crossover reaction yielding BCP with low polydispersities of PDI = 1.2 or smaller. Monitoring crossover reaction using MALDI mass spectrometry, particularly in case of **A** to **D**, showed the presence of considerable amount of homopolymer **A** species after crossover reactions with both Grubbs 1st and 3rd generation catalyst. Homopolymer poly(**A**_n) can be used as a probe for detection of the crossover-reaction via MALDI-methods, using defined amounts of equivalents of monomer **D**. Kinetic analysis revealed large differences between the use of Grubbs 1st- and Grubbs 3rd-generation catalyst, the Grubbs 3rd-generation catalyst being significantly faster is more efficient-catalyst during the crossover reaction. MALDI-analysis revealed no large differences between Grubbs 1st and 3rd generation catalyst in the quality and efficiency of the crossover-process from **A** to **D**. However, the crossover being incomplete the final block copolymers obtained have good polydispersities (PDI ≤ 1.2) with well controlled architecture, which is sufficient enough for preparing the required block copolymers poly(**A**_m-**b**-**D**_n) and poly(**A**_m-**b**-**C**_n) (scheme 5.1) for further nanotube preparation and nanophase separation studies respectively.



Scheme 5.1. Chemical structures of synthesized block copolymers.

Symmetric and asymmetric block composition of both poly(A_m - b - C_n) and poly(A_m - b - D_n) were synthesized with Grubbs 1st generation catalyst. SAXS measurements revealed the lamellar and hexagonally arranged cylindrical structures with 20-30 nm domain size depending upon the chain lengths. TEM images (figure 5.1) confirm the morphology obtained from SAXS.

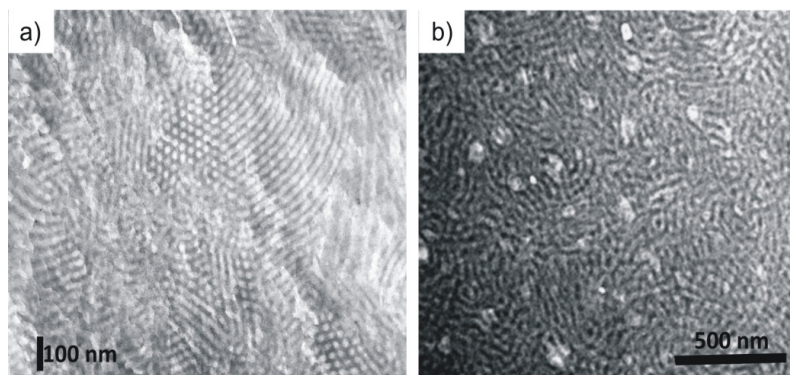


Figure 5.1. TEM image of a) A_{100} - b - D_{100} , hexagonally packed cylinders (bright) of block **A** in matrix of block **D** (dark). b) A_{140} - b - D_{60} , lamellar morphology.

Further the tubular nanostructures with walls exhibiting mesoscopic fine structures were accessible by melt infiltration of BCPs, (poly(A_m - b - D_n)), containing a fluorinated block into self-ordered AAO pores (figure 5.2). The microphase-separated BCPs commonly infiltrate AAO as solid threads according to classical capillary rise, whereas BCPs containing a fluorinated block, (poly(A_m - b - D_n)), formed mesoscopic precursor films on the pore walls under conditions where terminal flow is suppressed by microphase separation. Therefore, terminal flow is not essential for the formation of precursor films consisting of ordered liquids like microphase-separated BCPs, their development can apparently be driven by low surface energies of the newly formed polymer/air interfaces significantly reducing the overall interfacial energy of the system. Tubular BCP nanostructures with walls exhibiting internal mesoscopic fine structures such as concentric lamellae (figure 5.2) are accessible by solidification of the precursor films while circumventing the drawbacks associated with infiltration of BCP solutions into porous templates. Melt infiltration of BCPs able to form polymer/air interfaces with sufficiently low surface energies should be a generic access to nanostructures combining the functionalities of tubular morphologies and of microphase-separated BCPs. For example, internal and external surfaces of tubular BCP nanostructures may have different polarities since non-polar blocks (block-**D**) will segregate to the inner

polymer/air interface and polar blocks (block-A) to the external polymer/AAO interface. The generated concentric layers are unique in their structure, as the phenomenon opens up the possibility to design nanotubes with a functionalized internal or external surface independent of mechanical properties providing the necessary structural integrity which can be delivered by the other component of the copolymer. Hence, different parts of the tube walls could be selectively functionalized. It is conceivable that design and engineering of electronic, optical, chemical and mechanical properties of the tube walls might yield customized nano scaled components for charge-storage materials, solar cells and electrode materials.

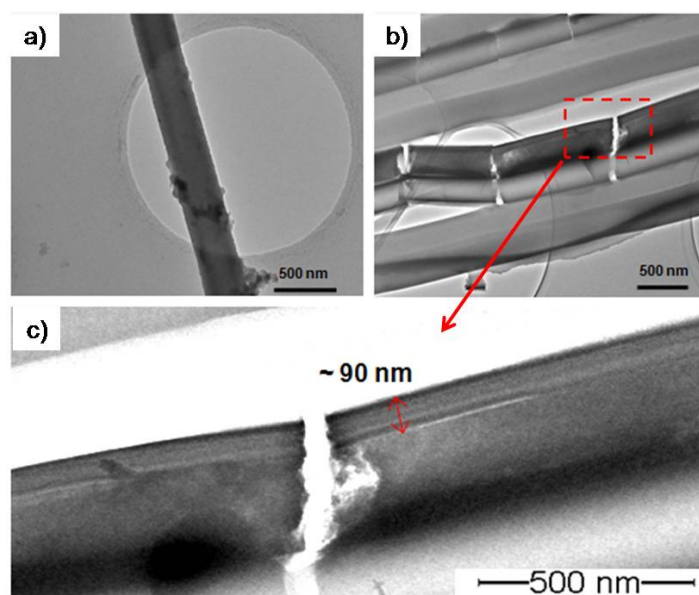


Figure 5.2. TEM images of a) released nanotube (A_{100} -b- D_{100}) showing darker edges and lighter hollow center, b) ultrathin slice of longitudinal cross-section of a released tube, c) expansion of figure b showing concentric lamellar structure in the tube wall with fluorine-rich areas (block **D**) having higher mass/thickness contrast and appearing darker than areas with low fluorine content (block **A**).

The morphology of the resulting nanostructures (tubes and rods) can be controlled by the internal state of order of the block copolymer. A simple change of molecular weight leads to control of either tube ($m=n=50, 100$) or nanorod ($m=n=25$). The disordered A_{25} -b- D_{25} exhibiting terminal flow fills the AAO pore completely generating nanorods where as ordered A_{100} -b- D_{100} and A_{50} -b- D_{50} yields tubular structures (figure 5.3).

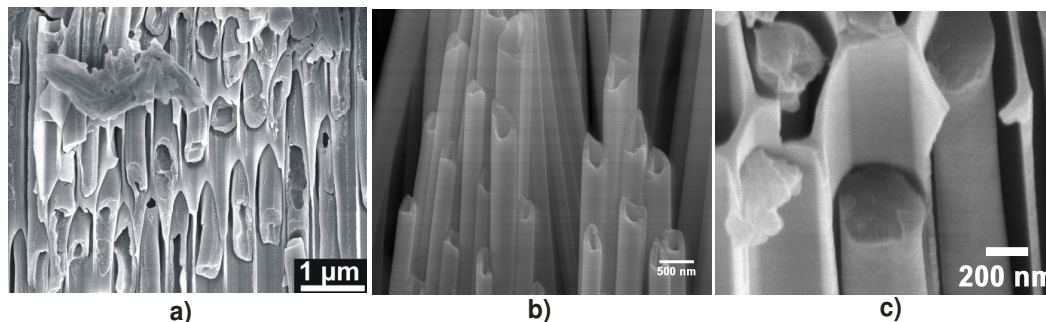


Figure 5.3. SEM images of AAO templates infiltrated with a) A_{100} - b - D_{100} , cross section of template showing the nanotubes protruding. b) nanotubes protruding out of alumina template formed from A_{50} - b - D_{50} . c) A_{25} - b - D_{25} nanorods with in the AAO template, side-view.

In the last section, the incompatibility driven and self-assembled nanostructures with a hierarchy of length scales in the nanometre range was investigated in the semi fluorinated long alkyl side chain containing symmetric and asymmetric BCP (poly(A_m - b - C_n)) in the bulk state. In a symmetric composition the block **A** and **C** form alternating lamellar structure and in case of asymmetric composition block **A** cylinders are arranged hexagonally in the matrix **C** due to the classical micro phase separation of incompatible **A** and **C** blocks. This leads to a large scale structure with long spacing of about 24 nm. While the nanophase separation of main and semi-fluorinated side chains in the **C** domains results in an internal structure of about 2.9 nm within the mesoscopic domains (24 nm). The pre-peak in the X-ray scattering at q range 0.2198 \AA^{-1} confirms the side chain nanodomain (figure 5.4). Additionally the main chain independent dynamics and primary α_{PE} like relaxation of semi-fluorinated side chains showing a non-Arrhenius-like temperature dependence obtained from DMA and dielectric relaxation spectroscopy measurements evidence the nanophase separated side chain domains. The side chain nanodomain size ($d_{nps}=2.9 \text{ nm}$) is almost twice the size of all *trans* extended length (1.407 nm) of semi-fluorinated side chains on block **C** and hence the side chains in the nanodomains are extended and are not interdigitated (figure 5.4). The nanophase separation under the confined state, i.e. within microphase separated BCP domains, can occur similarly like in the bulk state of side chain homopolymers.

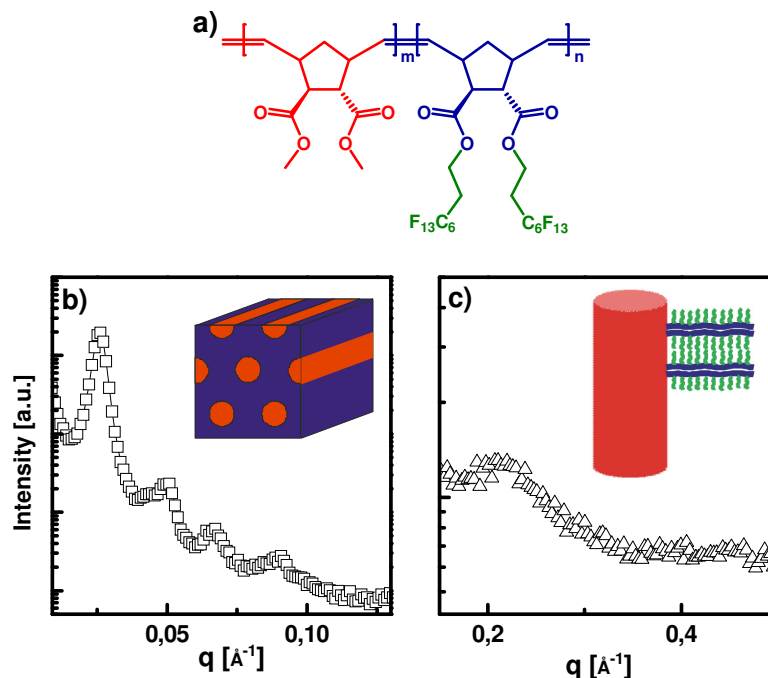


Figure 5.4. a) General structure of $\text{poly}(\text{A}_m\text{-b-C}_n)$, b) SAXS curve for $\text{poly}(\text{A}_{50}\text{-b-C}_{13})$ and inset schematic of BCP $\text{A}_{50}\text{-b-C}_{13}$ morphology in which **A** cylinders are hexagonally distributed in **C** matrix. c) X-ray scattering curve for $\text{poly}(\text{A}_{50}\text{-b-C}_{13})$ in the intermediate q range and the inset is the schematic showing the backbones of the **C** block (blue) aligned perpendicular to cylinder of block **A** (red) i.e. to the interfaces between both microphases and fluorinated side chains (green) are non-interdigitated.

Combination of these two structure formation mechanisms which are mostly independent of each other and can occur in parallel within a system proves to be one of the efficient pathways to fabricate the nanostructures in hierarchy levels with controlled composition and dimensions. The systematic variation of the second block and the side chains can be used to fine tune the mechanical properties of self-assembled systems with hierarchical structures. Other properties like optical, electrical, chemical and etc. of such polymers might be optimised by inclusion of certain functional moieties into the side chains. Hence the future studies should be focused in the direction of property optimization of such nano structures orienting towards application.

6. References

1. Hamley, I. W., Nanostructure fabrication using block copolymers. *Nanotechnology* **2003**, *14* (10), R39-R54.
2. Park, C.; Yoon, J.; Thomas, E. L., Enabling nanotechnology with self assembled block copolymer patterns. *Polymer* **2003**, *44* (22), 6725-6760.
3. Förster, S.; Konrad, M., From self-organizing polymers to nano- and biomaterials. *J. Mater. Chem.* **2003**, *13* (11), 2671-2688.
4. Förster, S.; Plantenberg, T., From Self-Organizing Polymers to Nanohybrid and Biomaterials. *Angew. Chem. Int. Ed.* **2002**, *41* (5), 688-714.
5. Bates, F. S.; Fredrickson, G. H., Block Copolymer Thermodynamics: Theory and Experiment. *Annu. Rev. Phys. Chem.* **1990**, *41* (1), 525-557.
6. Matsen, M. W.; Bates, F. S., Unifying Weak- and Strong-Segregation Block Copolymer Theories. *Macromolecules* **1996**, *29* (4), 1091-1098.
7. Lev, D. G.; et al., Phase separation in confined systems. *Rep. Prog. Phys.* **1999**, *62* (12), 1573.
8. Yu, B.; Sun, P.; Chen, T.; Jin, Q.; Ding, D.; Li, B.; Shi, A.-C., Confinement-Induced Novel Morphologies of Block Copolymers. *Phys. Rev. Lett.* **2006**, *96* (13), 138306-4.
9. S.-M. Park; Stoykovich, M. P.; Ruiz, R.; Zhang, Y.; Black, C. T.; Nealey, P. F., Directed Assembly of Lamellae- Forming Block Copolymers by Using Chemically and Topographically Patterned Substrates. *Adv. Mater.* **2007**, *19* (4), 607-611.
10. Koneripalli, N.; Singh, N.; Levicky, R.; Bates, F. S.; Gallagher, P. D.; Satija, S. K., Confined Block Copolymer Thin Films. *Macromolecules* **1995**, *28* (8), 2897-2904.
11. Russell, T. P.; Lambooy, P.; Kellogg, G. J.; Mayes, A. M., Diblock copolymers under confinement. *Phys. Rev. B: Condens. Matter* **1995**, *213-214*, 22-25.
12. Hamley, I. W., Ordering in thin films of block copolymers: Fundamentals to potential applications. *Prog. Poly. Sci.* **2009**, *34* (11), 1161-1210.
13. Knoll, A.; Horvat, A.; Lyakhova, K. S.; Krausch, G.; Sevink, G. J. A.; Zvelindovsky, A. V.; Magerle, R., Phase Behavior in Thin Films of Cylinder-Forming Block Copolymers. *Phys. Rev. Lett.* **2002**, *89* (3), 035501.
14. E. W Edwards; Montague, M. F.; Solak, H. H.; Hawker, C. J.; Nealey, P. F., Precise Control over Molecular Dimensions of Block-Copolymer Domains Using the Interfacial Energy of Chemically Nanopatterned Substrates. *Adv. Mater.* **2004**, *16* (15), 1315-1319.
15. Edwards, E. W.; Muller, M.; Stoykovich, M. P.; Solak, H. H.; dePablo, J. J.; Nealey, P. F., Dimensions and Shapes of Block Copolymer Domains Assembled on Lithographically Defined Chemically Patterned Substrates. *Macromolecules* **2007**, *40* (1), 90-96.
16. Kim, S. O.; Kim, B. H.; Kim, K.; Koo, C. M.; Stoykovich, M. P.; Nealey, P. F.; Solak, H. H., Defect Structure in Thin Films of a Lamellar Block Copolymer Self-Assembled on Neutral Homogeneous and Chemically Nanopatterned Surfaces. *Macromolecules* **2006**, *39* (16), 5466-5470.
17. Edwards, E. W.; Stoykovich, M. P.; Solak, H. H.; Nealey, P. F., Long-Range Order and Orientation of Cylinder-Forming Block Copolymers on Chemically Nanopatterned Striped Surfaces. *Macromolecules* **2006**, *39* (10), 3598-3607.
18. Yang, X. M.; Peters, R. D.; Nealey, P. F.; Solak, H. H.; Cerrina, F., Guided Self-Assembly of Symmetric Diblock Copolymer Films on Chemically Nanopatterned Substrates. *Macromolecules* **2000**, *33* (26), 9575-9582.
19. Stoykovich, M. P.; Edwards, E. W.; Solak, H. H.; Nealey, P. F., Phase Behavior of Symmetric Ternary Block Copolymer-Homopolymer Blends in Thin Films and on Chemically Patterned Surfaces. *Phys. Rev. Lett.* **2006**, *97* (14), 147802-4.

20. Wang, Q.; Nealey, P. F.; de Pablo, J. J., Simulations of the Morphology of Cylinder-Forming Asymmetric Diblock Copolymer Thin Films on Nanopatterned Substrates. *Macromolecules* **2003**, *36* (5), 1731-1740.
21. Nath, S. K.; Nealey, P. F.; de Pablo, J. J., Density functional theory of molecular structure for thin diblock copolymer films on chemically heterogeneous surfaces. *J. Chem. Phys.* **1999**, *110* (15), 7483-7490.
22. Yang, X. M.; Peters, R. D.; Nealey, P. F., Imaging the Substrate/Film Interface of Thin Films of Diblock Copolymers on Chemically Patterned Surfaces. *Macromolecules* **2002**, *35* (6), 2406-2409.
23. Fasolka, M. J.; Banerjee, P.; Mayes, A. M.; Pickett, G.; Balazs, A. C., Morphology of Ultrathin Supported Diblock Copolymer Films: Theory and Experiment. *Macromolecules* **2000**, *33* (15), 5702-5712.
24. Huang, E.; Rockford, L.; Russell, T. P.; Hawker, C. J., Nanodomain control in copolymer thin films. *Nature* **1998**, *395* (6704), 757-758.
25. Walton, D. G.; Kellogg, G. J.; Mayes, A. M.; Lambooy, P.; Russell, T. P., A Free Energy Model for Confined Diblock Copolymers. *Macromolecules* **1994**, *27* (21), 6225-6228.
26. Kellogg, G. J.; Walton, D. G.; Mayes, A. M.; Lambooy, P.; Russell, T. P.; Gallagher, P. D.; Satija, S. K., Observed Surface Energy Effects in Confined Diblock Copolymers. *Phys.Rev.Lett.* **1996**, *76* (14), 2503.
27. Wang, Q.; Nealey, P. F.; de Pablo, J. J., Monte Carlo Simulations of Asymmetric Diblock Copolymer Thin Films Confined between Two Homogeneous Surfaces. *Macromolecules* **2001**, *34* (10), 3458-3470.
28. Wang, Q.; Yan, Q.; Nealey, P. F.; de Pablo, J. J., Monte Carlo simulations of diblock copolymer thin films confined between two homogeneous surfaces. *J. Chem. Phys.* **2000**, *112* (1), 450-464.
29. Wang, Q.; Yan, Q.; Nealey, P. F.; de Pablo, J. J., Monte Carlo Simulations of Diblock Copolymer Thin Films Confined between Chemically Heterogeneous Hard Surfaces. *Macromolecules* **2000**, *33* (12), 4512-4525.
30. Cheng, J. Y.; Mayes, A. M.; Ross, C. A., Nanostructure engineering by templated self-assembly of block copolymers. *Nat Mater* **2004**, *3* (11), 823-828.
31. He, X.; Song, M.; Liang, H.; Pan, C., Self-assembly of the symmetric diblock copolymer in a confined state: Monte Carlo simulation. *The Journal of Chemical Physics* **2001**, *114* (23), 10510-10513.
32. Sevink, G. J. A.; Zvelindovsky, A. V.; Fraaije, J. G. E. M.; Huinink, H. P., Morphology of symmetric block copolymer in a cylindrical pore. *J. Chem. Phys.* **2001**, *115* (17), 8226-8230.
33. Li, W.; Wickham, R. A., Self-Assembled Morphologies of a Diblock Copolymer Melt Confined in a Cylindrical Nanopore. *Macromolecules* **2006**, *39* (24), 8492-8498.
34. Yu, B.; Sun, P.; Chen, T.; Jin, Q.; Ding, D.; Li, B.; Shi, A.-C., Confinement-Induced Novel Morphologies of Block Copolymers. *Phys. Rev.Lett.* **2006**, *96* (13), 138306-4.
35. Hongqi, X.; Kyusoon, S.; Taehyung, K.; Sungin, M.; McCarthy, T. J.; Russell, T. P., The influence of confinement and curvature on the morphology of block copolymers. *J. Polym. Sci. Part B: Polym.Phys.* **2005**, *43* (23), 3377-3383.
36. Xiang, H.; Shin, K.; Kim, T.; Moon, S. I.; McCarthy, T. J.; Russell, T. P., Block Copolymers under Cylindrical Confinement. *Macromolecules* **2004**, *37* (15), 5660-5664.
37. Shin, K.; Xiang, H.; Moon, S. I.; Kim, T.; McCarthy, T. J.; Russell, T. P., Curving and Frustrating Flatland. *Science* **2004**, *306* (5693), 76-.
38. Yiming, S.; Martin, S.; Danilo, Z.; Rameshwar, A.; Goerg, H. M.; Ulrich, G., Diameter-Dependence of the Morphology of PS-b-PMMA Nanorods Confined Within Ordered Porous Alumina Templates. *Macromol. Rapid Comm.* **2005**, *26* (5), 369-375.
39. Xiang, H.; Shin, K.; Kim, T.; Moon, S. I.; McCarthy, T. J.; Russell, T. P., From Cylinders to Helices upon Confinement. *Macromolecules* **2005**, *38* (4), 1055-1056.

40. Yong, Z.; Lei, J., Hollow Micro/Nanomaterials with Multilevel Interior Structures. *Adv. Mater.* **2009**, *21* (36), 3621-3638.
41. Wang, Y.; Gösele, U.; Steinhart, M., Mesoporous Polymer Nanofibers by Infiltration of Block Copolymers with Sacrificial Domains into Porous Alumina. *Chem. Mater.* **2007**, *20* (2), 379-381.
42. Wang, Y.; Gösele, U.; Steinhart, M., Mesoporous Block Copolymer Nanorods by Swelling-Induced Morphology Reconstruction. *Nano Lett.* **2008**, *8* (10), 3548-3553.
43. Hamely, I. W., *Block copolymers in solutions: Fundamentals and Applications*. Wiley, Chichester, West sussex. **2005**.
44. Zhang, L.; Eisenberg, A., Multiple Morphologies of "Crew-Cut" Aggregates of Polystyrene-b-poly(acrylic acid) Block Copolymers. *Science* **1995**, *268* (5218), 1728-1731.
45. Jain, S.; Bates, F. S., Consequences of Nonergodicity in Aqueous Binary PEO⁺PB Micellar Dispersions. *Macromolecules* **2004**, *37* (4), 1511-1523.
46. Pochan, D. J.; Chen, Z.; Cui, H.; Hales, K.; Qi, K.; Wooley, K. L., Toroidal Triblock Copolymer Assemblies. *Science* **2004**, *306* (5693), 94-97.
47. Won, Y.-Y.; Davis, H. T.; Bates, F. S., Giant Wormlike Rubber Micelles. *Science* **1999**, *283* (5404), 960-963.
48. Discher, D. E.; Eisenberg, A., Polymer Vesicles. *Science* **2002**, *297* (5583), 967-973.
49. Albrecht, K.; Mourran, A.; Moeller, M., Surface Micelles and Surface-Induced Nanopatterns Formed by Block Copolymers. In *Ordered Polymeric Nanostructures at Surfaces*, 2006; pp 57-70.
50. Tao, J.; Stewart, S.; Liu, G.; Yang, M., Star and Cylindrical Micelles of Polystyrene-block-poly(2-cinnamoyl ethyl methacrylate) in Cyclopentane. *Macromolecules* **1997**, *30* (9), 2738-2745.
51. Hamley, I. W., Nanoshells and nanotubes from block copolymers. *Soft Matter* **2005**, *1* (1), 36-43.
52. Yu, K.; Eisenberg, A., Bilayer Morphologies of Self-Assembled Crew-Cut Aggregates of Amphiphilic PS-b-PEO Diblock Copolymers in Solution. *Macromolecules* **1998**, *31* (11), 3509-3518.
53. Hyde, S., T., Curvature and the global structure of interfaces in surfactant -water systems. *J. Phys. Colloques* **1990**, *51* (C7), 209-228.
54. Yu, K.; Zhang, L.; Eisenberg, A., Novel Morphologies of Crew-Cut Aggregates of Amphiphilic Diblock Copolymers in Dilute Solution. *Langmuir* **1996**, *12* (25), 5980-5984.
55. Raez, J.; Manners, I.; Winnik, M. A., Nanotubes from the Self-Assembly of Asymmetric Crystalline-coil poly(ferrocenyldimethylsilane)-block-poly(dimethyl siloxane). *J. Am. Chem. Soc.* **2002**, *124* (35), 10381-10395.
56. Stewart, S.; Liu, G., Block Copolymer Nanotubes. *Angew. Chem. Int. Ed.* **2000**, *39* (2), 340-344.
57. Ulrich, R.; Chesne, A. D.; Templin, M.; Wiesner, U., Nano-objects with Controlled Shape, Size, and Composition from Block Copolymer Mesophases. *Adv. Mat.* **1999**, *11* (2), 141-146.
58. Lazzari, M.; López-Quintela, M. A., Block Copolymers as a Tool for Nanomaterial Fabrication. *Adv. Mat.* **2003**, *15* (19), 1583-1594.
59. Liu, G.; Ding, J.; Qiao, L.; Guo, A.; Dymov, B. P.; Gleeson, J. T.; Hashimoto, T.; Saijo, K., Polystyrene-block-poly(2-cinnamoyl ethyl methacrylate) Nanofibers - Preparation, Characterization, and Liquid Crystalline Properties. *Chem. Eur. J.* **1999**, *5* (9), 2740-2749.
60. Liu, G., Nanofibers. *Adv. Mat.* **1997**, *9* (5), 437-439.
61. Liu, G., Block Copolymer Nanotubes Derived from Self-Assembly. In *Self-Assembled Nanomaterials II, Vol. 220: advances in Polymer science*, Springer/Heidelberg, 2008; pp 29-64.

62. Vibha, K.; Jung Hun, L.; Jay Hoon, P.; Manuel, M.; Yong Lak, J., Confined Assembly of Asymmetric Block-Copolymer Nanofibers via Multiaxial Jet Electrospinning. *Small* **2009**, *9999*.
63. Masuda, H.; Fukuda, K., Ordered Metal Nanohole Arrays Made by a Two-Step Replication of Honeycomb Structures of Anodic Alumina. *Science* **1995**, *268* (5216), 1466-1468.
64. Masuda, H.; Yada, K.; Osaka, A., Self-Ordering of Cell Configuration of Anodic Porous Alumina with Large-Size Pores in Phosphoric Acid Solution. *Jpn. J. Appl. Phys.* **1998**, *37* (Part 2, No. 11A), L1340.
65. Martin, C. R., Nanomaterials: A Membrane-Based Synthetic Approach. *Science* **1994**, *266* (5193), 1961-1966.
66. Kim, E.; Xia, Y.; Whitesides, G. M., Polymer microstructures formed by moulding in capillaries. *Nature* **1995**, *376* (6541), 581-584.
67. Steinhart, M.; Wendorff, J. H.; Greiner, A.; Wehrspohn, R. B.; Nielsch, K.; Schilling, J.; Choi, J.; Gosele, U., Polymer Nanotubes by Wetting of Ordered Porous Templates. *Science* **2002**, *296* (5575), 1997-.
68. Steinhart, M.; Wehrspohn, R. B.; Gösele, U.; Wendorff, J. H., Nanotubes by Template Wetting: A Modular Assembly System. *Angew. Chem. Int. Ed.* **2004**, *43* (11), 1334-1344.
69. de Gennes, P. G., Wetting: statics and dynamics. *Reviews of Modern Physics* **1985**, *57* (3), 827.
70. Fox, H. W.; Hare, E. F.; Zisman, W. A., Wetting Properties of Organic Liquids on High-Energy Surfaces. *J. Phys. Chem.* **1955**, *59* (10), 1097-1106.
71. de Gennes P.-G; Brochard-Wyart .F; Quere .Q, Capillarity andWetting Phenomena. *Springer-Verlag* **2004**.
72. Zhang, M.; Dobriyal, P.; Chen, J. T.; Russell, T. P.; Olmo, J.; Merry, A., Wetting Transition in Cylindrical Alumina Nanopores with Polymer Melts. *Nano Lett.* **2006**, *6* (5), 1075-1079.
73. Chen, J. T.; Zhang, M.; Russell, T. P., Instabilities in Nanoporous Media. *Nano Lett.* **2007**, *7* (1), 183-187.
74. Everett, D. H.; Haynes, J. M., Model studies of capillary condensation. I. Cylindrical pore model with zero contact angle. *J. Colloid Interface Sci.* **1972**, *38* (1), 125-137.
75. Hammond, P. S., Nonlinear adjustment of a thin annular film of viscous fluid surrounding a thread of another within a circular cylindrical pipe. *J. Fluid Mech.* **1983**, *137* (-1), 363-384.
76. Silko, G.; Kathrin, S.; Petra, G.; Heiko, K.; Paul, T. M.; Andreas, G.; Joachim, H. W.; Ralf, B. W.; Ulrich, G.; Martin, S., Nondestructive Mechanical Release of Ordered Polymer Microfiber Arrays from Porous Templates. *Small* **2007**, *3* (6), 993-1000.
77. Martin, J.; Mijangos, C., Tailored Polymer-Based Nanofibers and Nanotubes by Means of Different Infiltration Methods into Alumina Nanopores. *Langmuir* **2009**, *25* (2), 1181.
78. Chen, J.-T.; Shin, K.; Leiston-Belanger, J. M.; Zhang, M.; Russell, T. P., Amorphous Carbon Nanotubes with Tunable Properties via Template Wetting. *Adv. Func. Mater.* **2006**, *16* (11), 1476-1480.
79. Rodriguez, A. T.; Chen, M.; Chen, Z.; Brinker, C. J.; Fan, H., Nanoporous Carbon Nanotubes Synthesized through Confined Hydrogen-Bonding Self-Assembly. *J. Am. Chem. Soc.* **2006**, *128* (29), 9276-9277.
80. Yong, W.; Yong, Q.; Andreas, B.; Eric, Y.; Changcheng, H.; Lianbing, Z.; Ulrich, G.; Mato, K.; Martin, S., Nanoscopic Morphologies in Block Copolymer Nanorods as Templates for Atomic-Layer Deposition of Semiconductors. *Adv. Mater.* **2009**, 9999.
81. Wang, Y.; Qin, Y.; Berger, A.; Yau, E.; He, C.; Zhang, L.; Gösele, U.; Knez, M.; Steinhart, M., Nanoscopic Morphologies in Block Copolymer Nanorods as Templates for Atomic-Layer Deposition of Semiconductors. *Adv. Mater.* **2009**, *21* (27), 2763-2766.

82. Bernett, M. K.; Zisman, W. A., Wetting properties of acrylic and methacrylic polymers containing fluorinated side chains. *J. Phys. Chem.* **1962**, *66* (6), 1207-1208.
83. Bernett, M. K.; Zisman, W. A., Wetting properties of polyhexafluoropropylene. *J. Phys. Chem.* **1961**, *65* (12), 2266-2267.
84. Pospiech, D.; Komber, H.; Voigt, D.; Jehnichen, D.; Häußler, L.; Gottwald, A.; Kollig, W.; Eckstein, K.; Baier, A.; Grundke, K., Synthesis and characterization of semifluorinated polymers and block copolymers. *Macromol. Symp.* **2003**, *199* (1), 173-186.
85. Al-Hussein, M.; Serero, Y.; Konovalov, O.; Mourran, A.; Moller, M.; de Jeu, W. H., Nanoordering of Fluorinated Side-Chain Liquid Crystalline/Amorphous Diblock Copolymers. *Macromolecules* **2005**, *38* (23), 9610-9616.
86. Beiner, M.; Schroter, K.; Hempel, E.; Reissig, S.; Donth, E., Multiple Glass Transition and Nanophase Separation in Poly(n-alkyl methacrylate) Homopolymers. *Macromolecules* **1999**, *32* (19), 6278-6282.
87. Chen, W.; Wunderlich, B., Nanophase separation of small and large molecules. *Macromol. Chem. Phys.* **1999**, *200* (2), 283-311.
88. Cowie, J. M. G.; Haq, Z.; McEwen, I. J.; Velickovic, J., Poly(alkyl itaconates): 8. Observations of dual glass transitions and crystallinity in the dialkyl ester series diheptyl to di-icosyl. *Polymer* **1981**, *22* (3), 327-332.
89. Floudas, G.; Stepanek, P., Structure and Dynamics of Poly(n-decyl methacrylate) below and above the Glass Transition. *Macromolecules* **1998**, *31* (20), 6951-6957.
90. Wunderlich, B., Thermodynamics and properties of nanophases. *Thermochimica Acta* **2009**, *492* (1-2), 2-15.
91. Beiner, M.; Huth, H., Nanophase separation and hindered glass transition in side-chain polymers. *Nat. Mater.* **2003**, *2* (9), 595-599.
92. Arrighi, V.; Triolo, A.; McEwen, I. J.; Holmes, P.; Triolo, R.; Amenitsch, H., Observation of Local Order in Poly(di-n-alkyl itaconate)s. *Macromolecules* **2000**, *33* (14), 4989-4991.
93. McCreight, K. W.; Ge, J. J.; Guo, M.; Mann, I.; Li, F.; Shen, Z.; Jin, X.; Harris, F. W.; Cheng, S. Z. D., Phase structures and transition behaviors in polymers containing rigid rodlike backbones with flexible side chains. V. Methylene side-chain effects on structure and molecular motion in a series of polyimides. *J. Poly. Sci. B: Poly. Phys.* **1999**, *37* (14), 1633-1646.
94. Nurulla, I.; Morikita, T.; Fukumoto, H.; Yamamoto, T., Preparation and Properties of Poly[(2-alkylbenzimidazole)-alt-thiophene]s with Long Alkyl Side Chains. *Macromol. Chem. Phys.* **2001**, *202* (11), 2335-2340.
95. Pankaj, S.; Hempel, E.; Beiner, M., Side-Chain Dynamics and Crystallization in a Series of Regiorandom Poly(3-alkylthiophenes). *Macromolecules* **2009**, *42* (3), 716-724.
96. Arbe, A.; Genix, A.-C.; Colmenero, J.; Richter, D.; Fouquet, P., Anomalous relaxation of self-assembled alkyl nanodomains in high-order poly(n-alkyl methacrylates). *Soft Matter* **2008**, *4* (9), 1792-1795.
97. Fredrickson, G. H.; Bates, F. S., Dynamics of Block Copolymers: Theory and Experiment. *Annu. Rev. Mater. Sci.* **1996**, *26* (1), 501-550.
98. Pospiech, D.; Häußler, L.; Jehnichen, D.; Kollig, W.; Eckstein, K.; Grundke, K., Bulk and surface properties of blends with semifluorinated polymers and block copolymers. *Macromol. Symp.* **2003**, *198* (1), 421-434.
99. Tsui, J.; Pospiech, D.; Jehnichen, D.; Häußler, L.; Kremer, F., Molecular dynamics in semifluorinated-side-chain polysulfone studied by broadband dielectric spectroscopy. *J. Appl. Polym. Sci.* **2007**, *105* (1), 201-207.
100. Pospiech, D.; Haussler, L.; Eckstein, K.; Komber, H.; Voigt, D.; Jehnichen, D.; Friedel, P.; Gottwald, A.; Kollig, W.; Kricheldorf, H. R., Synthesis and Phase Separation Behaviour of High Performance Multiblock Copolymers. *High Perform. Polym.* **2001**, *13* (2), S275-292.

101. Tsuiji, J.; Hartmann, L.; Kremer, F.; Pospiech, D.; Jehnichen, D.; Häußler, L., Molecular dynamics in semifluorinated side-chain polyesters as studied by broadband dielectric spectroscopy. *Polymer* **2006**, *47* (20), 7189-7197.
102. Gitsas, A.; Floudas, G.; Butt, H. J.; Pakula, T.; Matyjaszewski, K., Effects of Nanoscale Confinement and Pressure on the Dynamics of pODMA-b-ptBA-b-pODMA Triblock Copolymers. *Macromolecules* **2010**, *43* (5), 2453-2462.
103. Hempel, E.; Budde, H.; Höring, S.; Beiner, M., Side chain crystallization in microphase-separated poly(styrene-block-octadecylmethacrylate) copolymers. *Thermochimica Acta* **2005**, *432* (2), 254-261.
104. Mierzwa, M.; Floudas, G.; Wewerka, A., Dynamics of side-chain liquid-crystalline polymers: A dielectric spectroscopy investigation. *Phys. Rev. E* **2001**, *64* (3), 031703.
105. Schrock, R. R., Living ring-opening metathesis polymerization catalyzed by well-characterized transition-metal alkylidene complexes. *Acc. Chem. Res.* **1990**, *23* (5), 158-165.
106. Nguyen, S. T.; Johnson, L. K.; Grubbs, R. H.; Ziller, J. W., Ring-opening metathesis polymerization (ROMP) of norbornene by a Group VIII carbene complex in protic media. *J. Am. Chem. Soc.* **1992**, *114* (10), 3974-3975.
107. Charvet, R.; Novak, B. M., One-Pot, One-Catalyst Synthesis of Graft Copolymers by Controlled ROMP and ATRP Polymerizations. *Macromolecules* **2004**, *37* (23), 8808-8811.
108. Bielawski, C. W.; Grubbs, R. H., Living ring-opening metathesis polymerization. *Prog. Polym. Sci.* **2007**, *32* (1), 1-29.
109. Chauvin, Y., Olefin Metathesis: The Early Days (Nobel Lecture). *Angew. Chem. Int. Ed.* **2006**, *45* (23), 3740-3747.
110. Christian, S., The Ring Opening Metathesis Polymerisation Toolbox. *Macromol. Rapid Comm.* **2004**, *25* (14), 1283-1297.
111. Grubbs, R. H., Olefin-Metathesis Catalysts for the Preparation of Molecules and Materials (Nobel Lecture). *Angew. Chem. Int. Ed.* **2006**, *45* (23), 3760-3765.
112. Schrock, R. R., Multiple Metal-Carbon Bonds for Catalytic Metathesis Reactions (Nobel Lecture). *Angew. Chem. Int. Ed.* **2006**, *45* (23), 3748-3759.
113. Walker, R.; Conrad, R. M.; Grubbs, R. H., The Living ROMP of trans-Cyclooctene. *Macromolecules* **2009**, *42* (3), 599-605.
114. Matyjaszewski, K., Ranking living systems. *Macromolecules* **1993**, *26* (7), 1787-1788.
115. Choi, T.-L.; Grubbs, R. H., Controlled Living Ring-Opening-Metathesis Polymerization by a Fast-Initiating Ruthenium Catalyst. *Angew. Chemie Int. Ed.* **2003**, *42* (15), 1743-1746.
116. Wewerka, K.; Wewerka, A.; Stelzer, F.; Gallot, B.; Andruzzi, L.; Galli, G., New Microphase-Separated Diblock Copolymers Carrying Semifluorinated Side Groups Prepared by ROMP. *Macromol. Rapid Comm.* **2003**, *24* (15), 906-910.
117. Feast, W. J.; Khosravi, E., Synthesis of fluorinated polymers via ROMP: a review. *J. Fluorine Chem.* **1999**, (100), 117-125.
118. Dounis, P.; James Feast, W., A route to low polydispersity linear and star polyethylenes via ring-opening metathesis polymerization. *Polymer* **1996**, *37* (12), 2547-2554.
119. Trzaska, S. T.; Lee, L.-B. W.; Register, R. A., Synthesis of Narrow-Distribution "perfect" Polyethylene and Its Block Copolymers by Polymerization of Cyclopentene. *Macromolecules* **2000**, *33* (25), 9215-9221.
120. Notestein, J. M.; Lee, L.-B. W.; Register, R. A., Well-Defined Diblock Copolymers via Termination of Living ROMP with Anionically Polymerized Macromolecular Aldehydes. *Macromolecules* **2002**, *35* (6), 1985-1987.
121. Risse, W.; Grubbs, R. H., Block and graft copolymers by living ring-opening olefin metathesis polymerization. *J. Mol. Catal. A: Chem.* **1991**, *65* (1-2), 211-217.

122. Tritto, I.; Sacchi, M. C.; Grubbs, R. H., From ring-opening metathesis polymerization to Ziegler-Natta polymerization: A method for obtaining polynorbornene-polyethylene block copolymers. *J. Mol. Catal. A: Chem.* **1993**, *82* (1), 103-111.
123. Novak, B.; Risse, W.; Grubbs, R., The development of well-defined catalysts for ring-opening olefin metathesis polymerizations (ROMP). In *Polymer Synthesis Oxidation Processes, Vol. 102: advances in Polymer science, Springer/Heidelberg*, 1992; pp 47-72.
124. Risse, W.; Grubbs, R. H., A novel route to block copolymers by changing the mechanism from living ring-opening metathesis polymerization of cyclic olefins to aldol condensation polymerization of silyl vinyl ethers. *Macromolecules* **1989**, *22* (4), 1558-1562.
125. Weck, M.; Schwab, P.; Grubbs, R. H., Synthesis of ABA Triblock Copolymers of Norbornenes and 7-Oxanorbornenes via Living Ring-Opening Metathesis Polymerization Using Well-Defined, Bimetallic Ruthenium Catalysts. *Macromolecules* **1996**, *29* (5), 1789-1793.
126. Iyengar, D. R.; Perutz, S. M.; Dai, C.-A.; Ober, C. K.; Kramer, E. J., Surface Segregation Studies of Fluorine-Containing Diblock Copolymers *Macromolecules* **1996**, *29* (4), 1229-1234.
127. Wang, J.; Mao, G.; Ober, C. K.; Kramer, E. J., Liquid Crystalline, Semifluorinated Side Group Block Copolymers with Stable Low Energy Surfaces: Synthesis, Liquid Crystalline Structure, and Critical Surface Tension. *Macromolecules* **1997**, *30* (7), 1906-1914.
128. Li, X.; Andruzzi, L.; Chiellini, E.; Galli, G.; Ober, C. K.; Hexemer, A.; Kramer, E. J.; Fischer, D. A., Semifluorinated Aromatic Side-Group Polystyrene-Based Block Copolymers: Bulk Structure and Surface Orientation Studies. *Macromolecules* **2002**, *35* (21), 8078-8087.
129. Kim, B. G.; Chung, J.-S.; Sohn, E.-H.; Kwak, S.-Y.; Lee, J.-C., Comb-Like Fluorinated Polystyrenes Having Different Side Chain Interconnecting Groups. *Macromolecules* **2009**, *42* (9), 3333-3339.
130. Luning, J.; Stohr, J.; Song, K. Y.; Hawker, C. J.; Iodice, P.; Nguyen, C. V.; Yoon, D. Y., Correlation of Surface and Bulk Order in Low Surface Energy Polymers. *Macromolecules* **2001**, *34* (5), 1128-1130.
131. Stubenrauch, K.; Moitzl, C.; Fritz, G.; Glatter, O.; Trimmel, G.; Stelzer, F., Precise Tuning of Micelle, Core, and Shell Size by the Composition of Amphiphilic Block Copolymers Derived from ROMP Investigated by DLS and SAXS. *Macromolecules* **2006**, *39* (17), 5865-5874.
132. Binder, W. H.; Kluger, C.; Josipovic, M.; Straif, C. J.; Friedbacher, G., Directing Supramolecular Nanoparticle Binding onto Polymer Films: Film Formation and Influence of Receptor Density on Binding Densities. *Macromolecules* **2006**, *39* (23), 8092-8101.
133. Shimizu, T.; Tanaka, Y.; Kutsumizu, S.; Yano, S., Ordered Structure of poly(1H,1H-fluoroalkyl alpha-fluoroacrylate)s. *Macromolecules* **1996**, *29* (1), 156-164.
134. Genzer, J.; Efimenko, K., Creating Long-Lived Superhydrophobic Polymer Surfaces Through Mechanically Assembled Monolayers. *Science* **2000**, *290* (5499), 2130-2133.
135. Genzer, J.; Sivaniah, E.; Kramer, E. J.; Wang, J.; Xiang, M.; Char, K.; Ober, C. K.; Bubeck, R. A.; Fischer, D. A.; Graupe, M.; Colorado, R.; Shmakova, O. E.; Lee, T. R., Molecular Orientation of Single and Two-Armed Monodendron Semifluorinated Chains on "Soft" and "Hard" Surfaces Studied Using NEXAFS. *Macromolecules* **2000**, *33* (16), 6068-6077.
136. Montaudo, G.; Samperi, F.; Montaudo, M. S., Characterization of synthetic polymers by MALDI-MS. *Prog. Polym. Sci.* **2006**, *31* (3), 277-357.
137. Maurizio, S. M., Mass spectra of copolymers. *Mass Spectrom. Rev.* **2002**, *21* (2), 108-144.
138. Wilczek-Vera, G.; Yu, Y.; Waddell, K.; Danis, P. O.; Eisenberg, A., Detailed structural analysis of diblock copolymers by matrix-assisted laser desorption/ionization time-of-flight mass spectrometry. *Rapid Commun. Mass Spectrom.* **1999**, *13* (9), 764-777.
139. Wilczek-Vera, G.; Yu, Y.; Waddell, K.; Danis, P. O.; Eisenberg, A., Analysis of Diblock Copolymers of Poly(alpha-methylstyrene)-block-polystyrene by Mass Spectrometry. *Macromolecules* **1999**, *32* (7), 2180-2187.

140. Wilczek-Vera, G.; Danis, P. O.; Eisenberg, A., Individual Block Length Distributions of Block Copolymers of Polystyrene-block-Poly(alpha-methylstyrene) by MALDI/TOF Mass Spectrometry. *Macromolecules* **1996**, *29* (11), 4036-4044.
141. Willemse, R. X. E.; Staal, B. B. P.; Donkers, E. H. D.; van Herk, A. M., Copolymer Fingerprints of Polystyrene-block-polyisoprene by MALDI-ToF-MS. *Macromolecules* **2004**, *37* (15), 5717-5723.
142. Lee, D.; Teraoka, I.; Fujiwara, T.; Kimura, Y., Phase Fluctuation Chromatography of Diblock Copolymer of Poly(ethylene glycol) and Poly(L-lactide) for Fractionation by the Block Length Ratio. *Macromolecules* **2001**, *34* (14), 4949-4957.
143. Huijser, S.; Staal, B. B. P.; Huang, J.; Duchateau, R.; Koning, C. E., Chemical Composition and Topology of Poly(lactide-co-glycolide) Revealed by Pushing MALDI-TOF MS to Its Limit. *Angew. Chem., Int. Ed.* **2006**, *45* (25), 4104-4108.
144. Meier, M. A. R.; Aerts, S. N. H.; Staal, B. B. P.; Rasa, M.; Schubert, U. S., PEO-*b*-PCL Block Copolymers: Synthesis, Detailed Characterization, and Selected Micellar Drug Encapsulation Behavior. *Macromol. Rapid Commun.* **2005**, *26* (24), 1918-1924.
145. Schrock, R. R.; Gabert, A. J.; Singh, R.; Hock, A. S., Synthesis of High Oxidation State Bimetallic Alkylidene Complexes for Controlled ROMP Synthesis of Triblock Copolymers. *Organometallics* **2005**, *24* (21), 5058-5066.
146. Hilf, S.; Grubbs, R. H.; Kilbinger, A. F. M., Sacrificial Synthesis of Hydroxy-Functionalized ROMP Polymers: An Efficiency Study. *Macromolecules* **2008**, *41* (16), 6006-6011.
147. Scherman, O. A.; Rutenberg, I. M.; Grubbs, R. H., Direct Synthesis of Soluble, End-Functionalized Polyenes and Polyacetylene Block Copolymers. *J. Am. Chem. Soc.* **2003**, *125* (28), 8515-8522.
148. Guttman, C. M.; Flynn, K. M.; Wallace, W. E.; Kearsley, A. J., Quantitative Mass Spectrometry and Polydisperse Materials: Creation of an Absolute Molecular Mass Distribution Polymer Standard. *Macromolecules* **2009**, *42* (5), 1695-1702.
149. Schnöll-Bitai, I.; Hrebicek, T.; Rizzi, A., Towards a Quantitative Interpretation of Polymer Distributions from MALDI-TOF Spectra. *Macromol. Chem. Phys.* **2007**, *208* (5), 485-495.
150. Wetzel, S. J.; Guttman, C. M.; Girard, J. E., The influence of matrix and laser energy on the molecular mass distribution of synthetic polymers obtained by MALDI-TOF-MS. *Int. J. Mass Spectrom.* **2004**, *238* (3), 215-225.
151. Liu, X. M.; Maziarz, E. P.; Quinn, E.; Lai, Y.-C., A perspective on relative quantitation of a polydisperse polymer using chromatography and mass spectrometry. *Int. J. Mass Spectrom.* **2004**, *238* (3), 227-233.
152. Guttman, C. M.; Wetzel, S. J.; Blair, W. R.; Fanconi, B. M.; Girard, J. E.; Goldschmidt, R. J.; Wallace, W. E.; VanderHart, D. L., NIST-Sponsored Interlaboratory Comparison of Polystyrene Molecular Mass Distribution Obtained by Matrix-Assisted Laser Desorption/Ionization Time-of-Flight Mass Spectrometry: Statistical Analysis. *Anal. Chem.* **2001**, *73* (6), 1252-1262.
153. Chen, H.; He, M.; Pei, J.; He, H., Quantitative Analysis of Synthetic Polymers Using Matrix-Assisted Laser Desorption/Ionization Time-of-Flight Mass Spectrometry. *Anal. Chem.* **2003**, *75* (23), 6531-6535.
154. Chen, H.; He, M., Quantitation of synthetic polymers using an internal standard by matrix-assisted laser desorption/ionization time-of-flight mass spectrometry. *J. Am. Soc. Mass Spectrom.* **2005**, *16* (1), 100-106.
155. Grubbs, R. H., Olefin metathesis. *Tetrahedron* **2004**, *60* (34), 7117-7140.
156. Love, J. A.; Sanford, M. S.; Day, M. W.; Grubbs, R. H., Synthesis, Structure, and Activity of Enhanced Initiators for Olefin Metathesis. *J. Am. Chem. Soc.* **2003**, *Vol 125*, 10103-10109.
157. Sanford, M. S.; Ulman, M.; Grubbs, R. H., New Insights into the Mechanism of Ruthenium-Catalyzed Olefin Metathesis Reactions. *J. Am. Chem. Soc.* **2001**, *123* (4), 749-750.

158. Frenzel, U.; Nuyken, O., Ruthenium-Based Metathesis Initiators: Development and Use in Ring-Opening Metathesis Polymerization. *J. Poly. Sci. Part A: Poly. Chem.* **2002**, Vol 40 2859-2915.
159. Black, G.; Maher, D.; Risse, W., Living Ring-Opening Olefin Metathesis Polymerization. In *Handbook of Metathesis*, Professor Robert, H. G., Ed. 2008, pp 2-71, ISBN: 3527306161.
160. Khosravi, E., Synthesis of Copolymers. In *Handbook of Metathesis*, Professor Robert, H. G., Ed. 2008; Vol. ISBN: 3527306161, pp 72-117.
161. Kanaoka, S.; Grubbs, R. H., Synthesis of Block Copolymers of Silicon-Containing Norbornene Derivatives via Living Ring-Opening Metathesis Polymerization Catalyzed by a Ruthenium Carbene Complex. *Macromolecules* **1995**, 28 (13), 4707-4713.
162. Heijboer, J., *Physics of non crystalline solids; Prins, J.A., Ed.1; North Holland: Amsterdam 1965*, 231.
163. Abetz, V.; Simon, P., Phase Behavior and Morphologies of Block Copolymers. In *Block Copolymers I, Vol. 189: Advances in Polymer Science, Springer Berlin / Heidelberg, 2005*, 125., 2005; pp 125-212.
164. Leibler, L., Theory of Microphase Separation in Block Copolymers. *Macromolecules* **1980**, 13 (6), 1602-1617.
165. Río, O. I. d.; Neumann, A. W., Axisymmetric Drop Shape Analysis: Computational Methods for the Measurement of Interfacial Properties from the Shape and Dimensions of Pendant and Sessile Drops. *J. Colloid Interface Sci.* **1997**, 196 (2), 136-147.
166. Chu, B.; Hsiao, B. S., Small-Angle X-ray Scattering of Polymers. *Chem. Rev.* **2001**, 101 (6), 1727-1762.
167. Stuhn, B.; Mutter, R.; Albrecht, T., Direct Observation of Structure Formation at the Temperature-Driven Order-To-Disorder Transition in Diblock Copolymers. *EPL (Europhysics Letters)* **1992**, 18 (5), 427-432.
168. Rosedale, J. H.; Bates, F. S.; Almdal, K.; Mortensen, K.; Wignall, G. D., Order and Disorder in Symmetric Diblock Copolymer Melts. *Macromolecules* **1995**, 28 (5), 1429-1443.
169. Schmidt, D. L.; Coburn, C. E.; DeKoven, B. M.; Potter, G. E.; Meyers, G. F.; Fischer, D. A., Water-based non-stick hydrophobic coatings. *Nature* **1994**, 368 (6466), 39-41.
170. Beiner, M., Relaxation in Poly(alkyl methacrylate)s: Crossover Region and Nanophase Separation. *Macromo. Rapid Commun.* **2001**, 22 (12), 869-895.
171. Boyd, R.; Smith, G., Polymer Dynamics and Relaxation. *Cambridge University Press 2007*, Ed.1 (ISBN: 9780521814195).
172. Beiner, M.; Korus, J.; Lockwenz, H.; Schroter, K.; Donth, E., Heat Capacity Spectroscopy Compared to Other Linear Response Methods at the Dynamic Glass Transition in Poly(vinyl acetate). *Macromolecules* **1996**, 29 (15), 5183-5189.
173. Donth, E.; Beiner, M.; Reissig, S.; Korus, J.; Garwe, F.; Vieweg, S.; Kahle, S.; Hempel, E.; Schroter, K., Fine Structure of the Main Transition in Amorphous Polymers: Entanglement Spacing and Characteristic Length of the Glass Transition. Discussion of Examples. *Macromolecules* **1996**, 29 (20), 6589-6600.
174. Bohmer, R.; Ngai, K. L.; Angell, C. A.; Plazek, D. J., Nonexponential relaxations in strong and fragile glass formers. *J.Chem.Phy.* **1993**, 99 (5), 4201-4209.
175. Beiner, M.; Huth, H.; Schröter, K., Crossover region of dynamic glass transition: general trends and individual aspects. *J. Non-Cryst. Solids* **2001**, 279 (2-3), 126-135.
176. Chen, H.-L.; Wu, J.-C.; Lin, T.-L.; Lin, J. S., Crystallization Kinetics in Microphase-Separated Poly(ethylene oxide)-block-poly(1,4-butadiene). *Macromolecules* **2001**, 34 (20), 6936-6944.
177. Loo, Y.-L.; Register, R. A.; Adamson, D. H., Polyethylene Crystal Orientation Induced by Block Copolymer Cylinders. *Macromolecules* **2000**, 33 (22), 8361-8366.
178. Li, T.; Wang, W. J.; Liu, R.; Liang, W. H.; Zhao, G. F.; Li, Z.; Wu, Q.; Zhu, F. M., Double-Crystalline Polyethylene-b-poly(ethylene oxide) with a Linear Polyethylene Block:

- Synthesis and Confined Crystallization in Self-Assembled Structure Formed from Aqueous Solution. *Macromolecules* **2009**, *42* (11), 3804-3810.
179. Ho, R.-M.; Lin, F.-H.; Tsai, C.-C.; Lin, C.-C.; Ko, B.-T.; Hsiao, B. S.; Sics, I., Crystallization-Induced Undulated Morphology in Polystyrene-*b*-Poly(l-lactide) Block Copolymer. *Macromolecules* **2004**, *37* (16), 5985-5994.
180. Loo, Y.-L.; Register, R. A.; Ryan, A. J., Polymer Crystallization in 25-nm Spheres. *Phys. Rev. Lett.* **2000**, *84* (18), 4120.
181. Loo, Y.-L.; Register, R. A.; Ryan, A. J.; Dee, G. T., Polymer Crystallization Confined in One, Two, or Three Dimensions. *Macromolecules* **2001**, *34* (26), 8968-8977.
182. Loo, Y.-L.; Register, R. A.; Ryan, A. J., Modes of Crystallization in Block Copolymer Microdomains: Breakout, Templated, and Confined. *Macromolecules* **2002**, *35* (6), 2365-2374.
183. Holzer, B.; Lehmann, A.; Stühn, B.; Kowalski, M., Asymmetric diblock copolymers near the microphase separation: limitations of mean field theory. *Polymer* **1991**, *32* (11), 1935-1942.
184. Stühn, B., The relation between the microphase separation transition and the glass transition in diblock copolymers. *J. Polym. Sci. Part B: Polym. Phys.* **1992**, *30* (9), 1013-1019.

7. Appendix

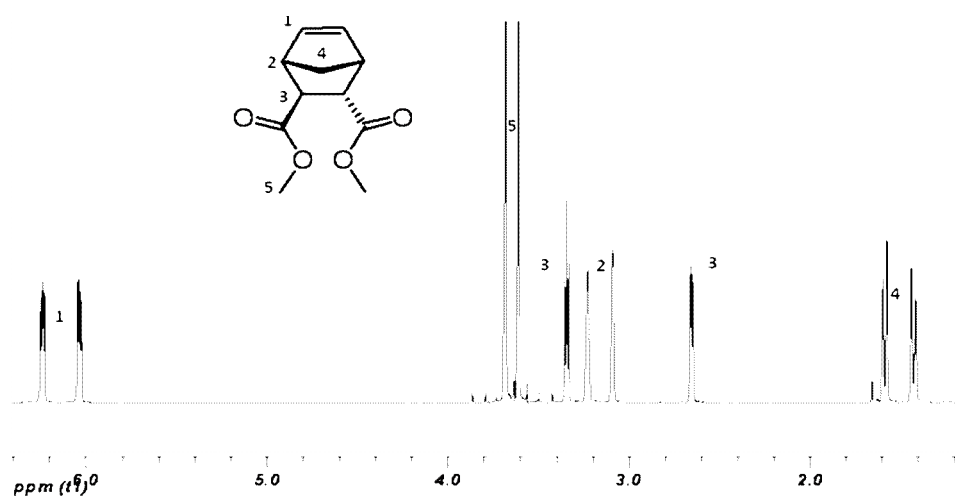


Figure 1. ^1H -NMR Spectra of monomer A

^1H NMR (δ ppm, CDCl_3 , 400 MHz): 6.27 (q, 1H), 6.07 (q, 1H), 3.71 (s, 3H), 3.64 (s, 3H), 3.37 (t, 1H), 3.26 (s, 1H), 3.13 (s, 1H), 2.68 (m, 1H), 1.60 (m, 1H), 1.47 (m, 1H).

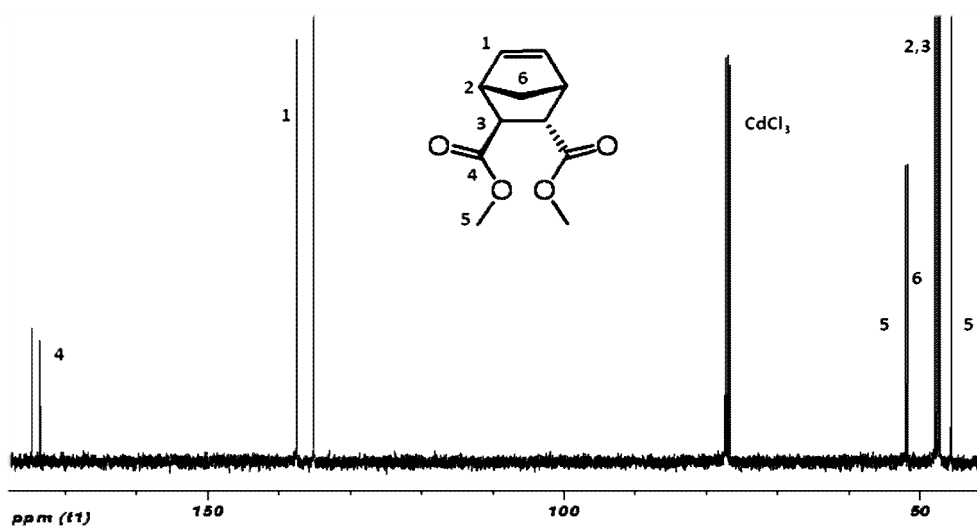


Figure 2. ^{13}C -NMR spectrum of monomer A

^{13}C NMR (δ ppm, CDCl_3 , 101 MHz): 174.74, 173.54, 137.48, 135.12, 52.02, 51.74, 47.93, 47.66, 47.35, 47.18, 45.67.

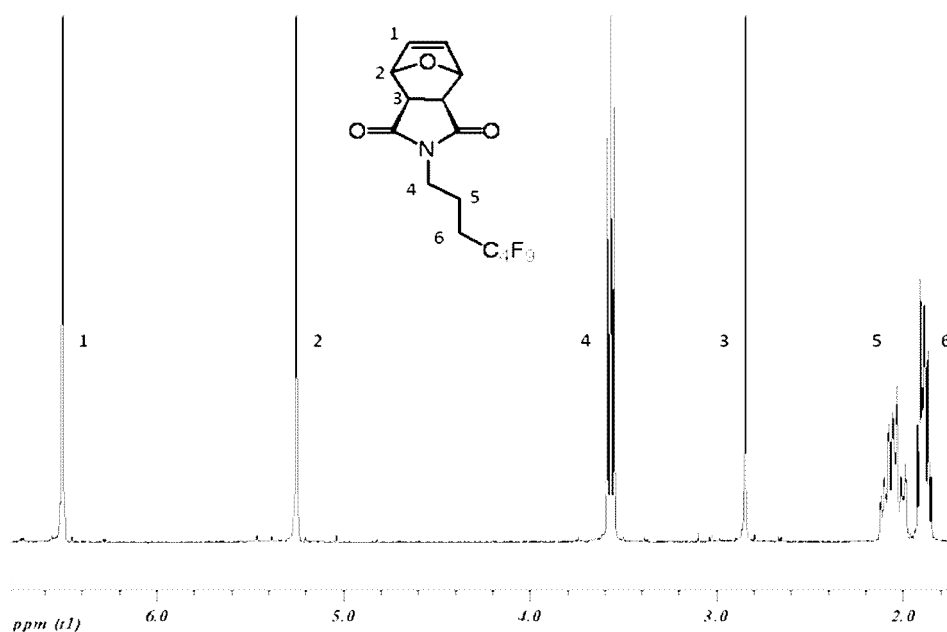


Figure 3. ^1H -NMR Spectra of monomer **D**

^1H NMR (δ ppm, CDCl_3 , 400 MHz): 6.51 (td, $J = 4.42, 0.80, 0.80$ Hz, 2H), 5.26 (td, $J = 1.87, 0.90, 0.90$ Hz, 2H), 3.57 (t, $J = 6.92, 6.92$ Hz, 2H), 2.88-2.83 (m, 2H), 2.14-1.97 (m, 2H), 1.95-1.83 (m, 2H).

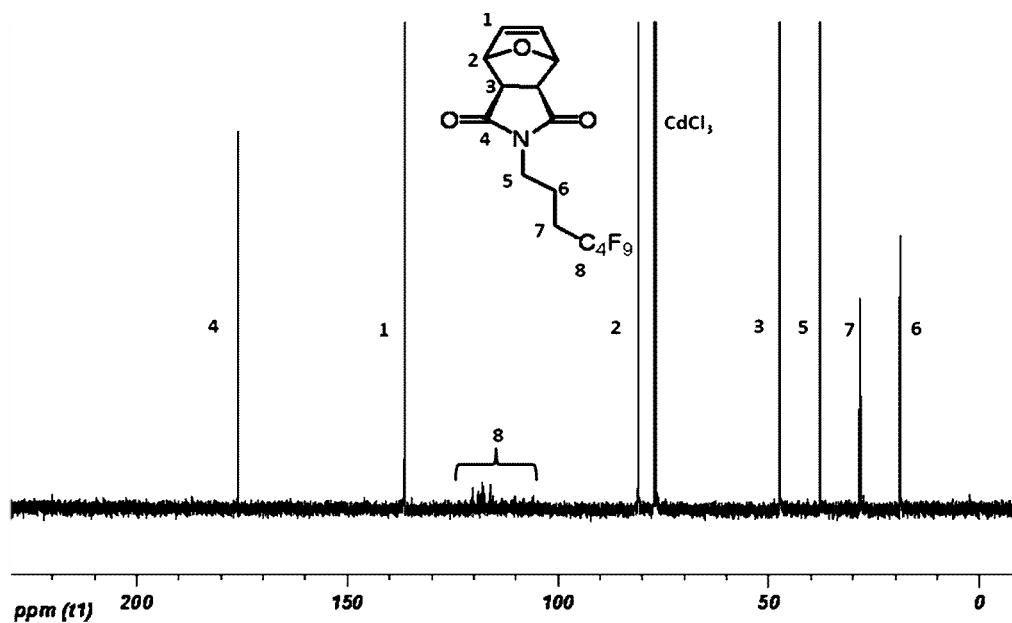


Figure 4. ^{13}C -NMR Spectra of monomer **D**

^{13}C NMR (δ ppm, CDCl_3 , 101 MHz): 176.00, 136.44, 121.5-105.0 (multiplets, $J_{FC} = 98\text{Hz}$, $J_{FC}^2 = 22$ Hz), 81.01, 47.40 (d, $J = 7.59$ Hz), 37.84, 28.52 (t, $J_{FC}^2 = 22$ Hz), 28.30, 28.08, 18.87 (t, $J = 3.85$ Hz).

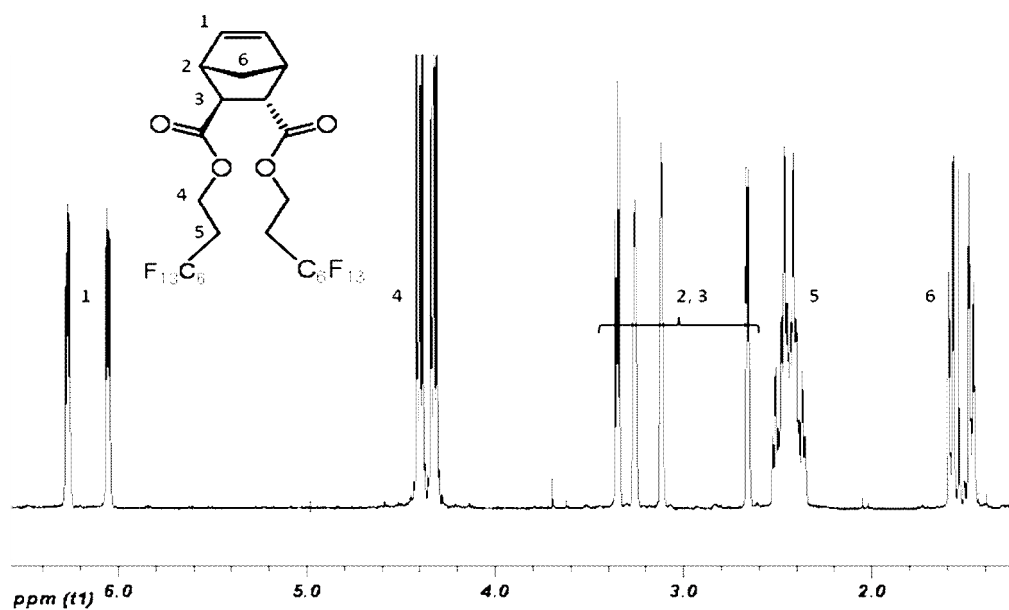


Figure 5. ^1H -NMR Spectra of monomer C

^1H NMR (δ ppm, CDCl_3 , 400 MHz): 6.27 (dd, $J = 5.59, 3.12$ Hz, 1H), 6.06 (dd, $J = 5.61, 2.81$ Hz, 1H), 4.36 (td, $J_{\text{H-F}} = 30.16, 6.35$, 4H), 3.40-3.20 (m, 2H), 3.17-3.06 (m, 1H), 2.66 (dd, $J = 4.57, 1.63$ Hz, 1H), 2.44 (tq, $J = 19.41, J = 6.32$ Hz, 4H), 1.64-1.41 (m, 1H), 1.28-1.19 (m, 1H).

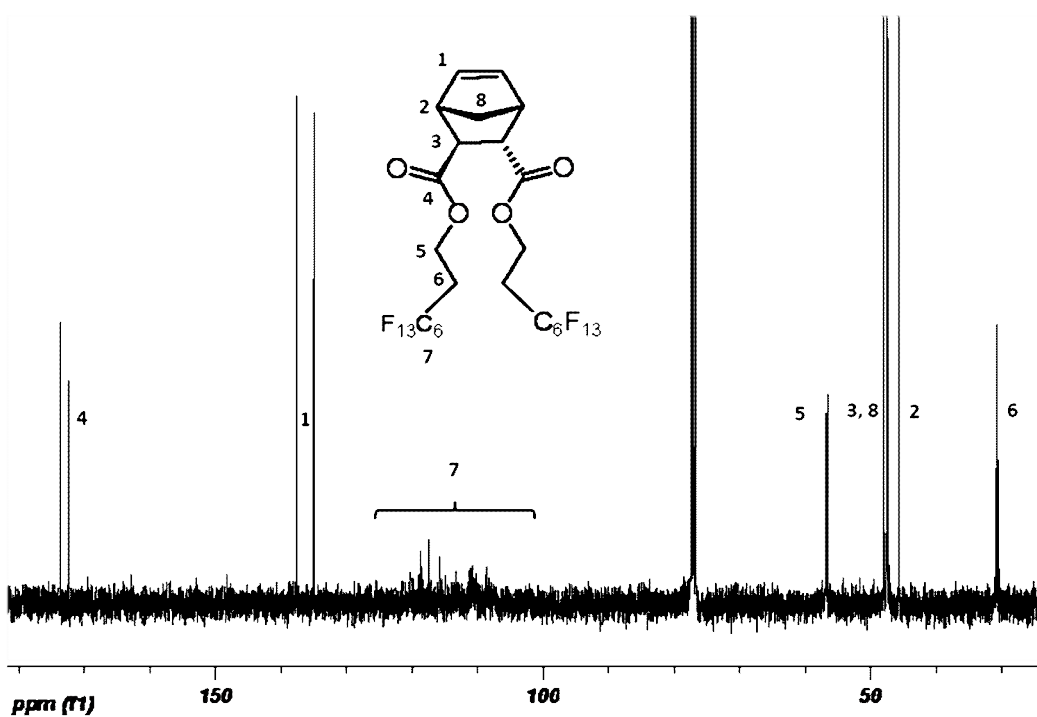


Figure 6. ^{13}C -NMR Spectra of monomer C

^{13}C NMR (δ ppm, CDCl_3 , 101 MHz): 173.63, 172.41, 137.55, 134.98, 100.00 – 120.20 (multiplet), 56.84 (dd, $J = 6.40, 2.74$ Hz), 56.59 (dd, $J = 6.70, 2.70$ Hz), 48.05, 47.50 (d, $J = 11.92$ Hz), 47.26, 45.67, 30.95-30.52.

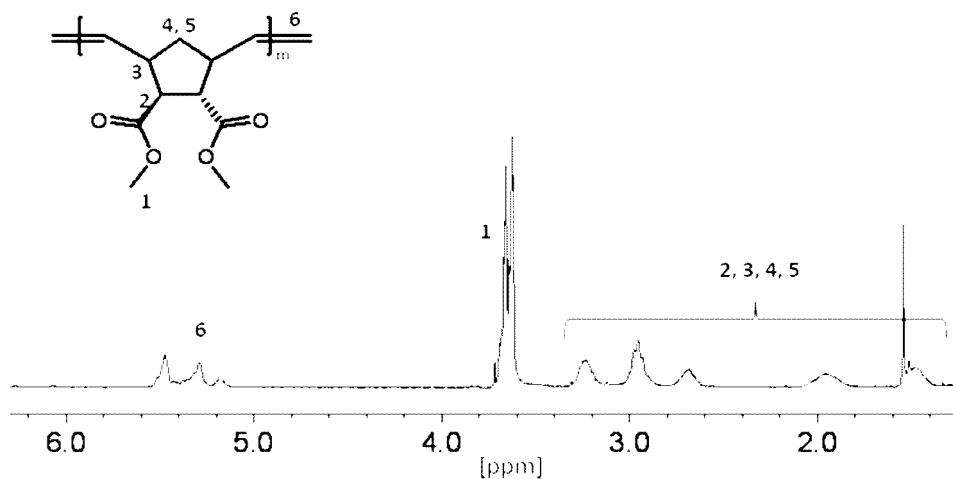


Figure 7. ^1H -NMR Spectra of poly(A_{200})

^1H NMR (δ ppm, CDCl_3 , 400 MHz): 5.48 -5.24 (m, 2H), 3.75-3.57 (m, 6H), 3.04-2.88 (m, 4H), 1.96 (s, 1H), 1.56 (s, 1H).

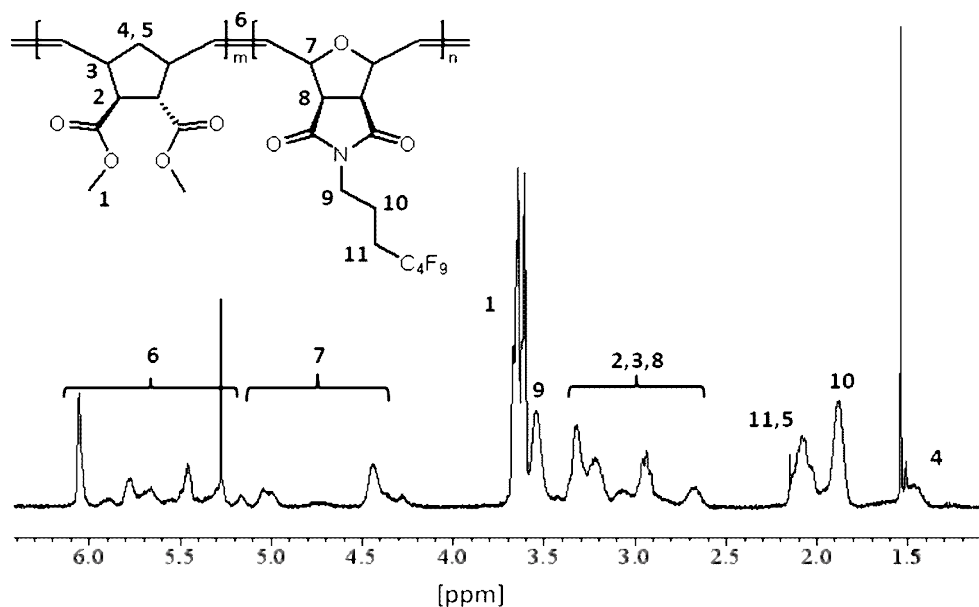


Figure 8. ^1H -NMR spectrum of poly($\text{A}_{100}\text{-b-D}_{100}$)

^1H NMR (δ ppm, CDCl_3 , 400 MHz): 6.20-4.22 (m, 6H), 3.77-3.60 (m, 6H), 3.60-3.45 (s, 2H), 3.43-2.60 (m, 6H), 2.15-1.77 (m, 5H), 1.55 (s, 1H).

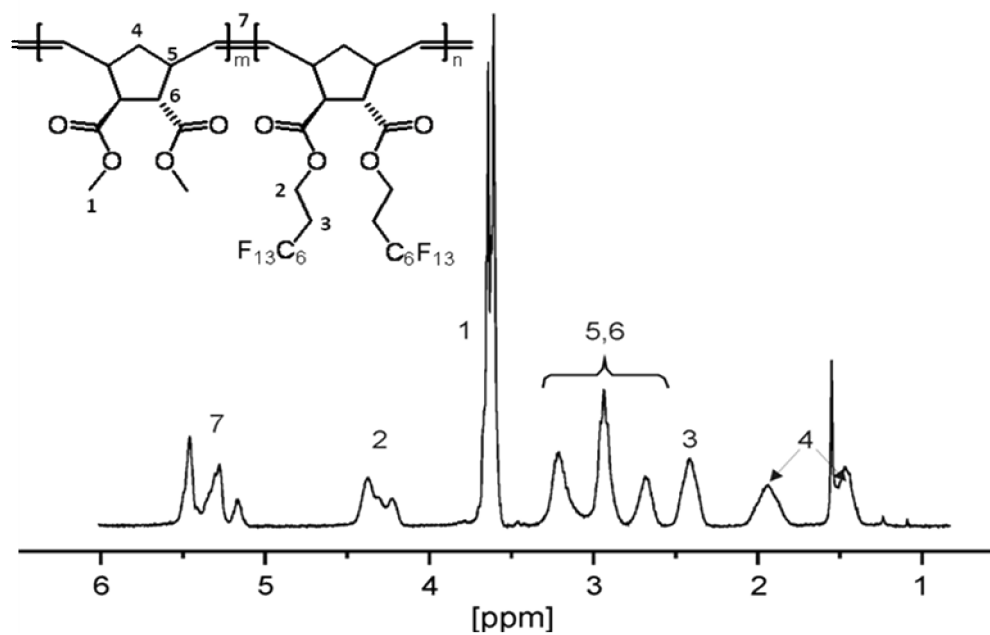


Figure 9. ¹H-NMR spectrum of poly(A₅₀-b-C₁₃)

¹H NMR (δ ppm, CDCl₃, 400 MHz): 5.60-5.10 (m, 2.6H), 4.51-4.15 (m, 1.2H), 3.73-3.57 (m, 6H), 3.38-2.59 (m, 5.1H), 2.43 (s, 1.3H), 1.95 (s, 1.2H), 1.54 (s, 1.2H).

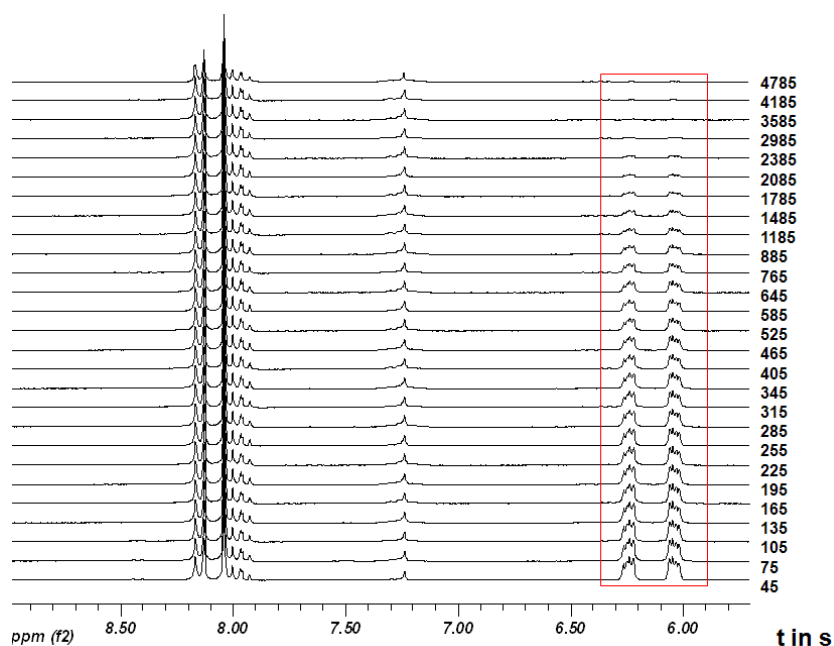


Figure 10. ¹H-NMR spectra of monomer A consumption during polymerization in CDCl₃ at 27° C with Grubbs I catalyst.

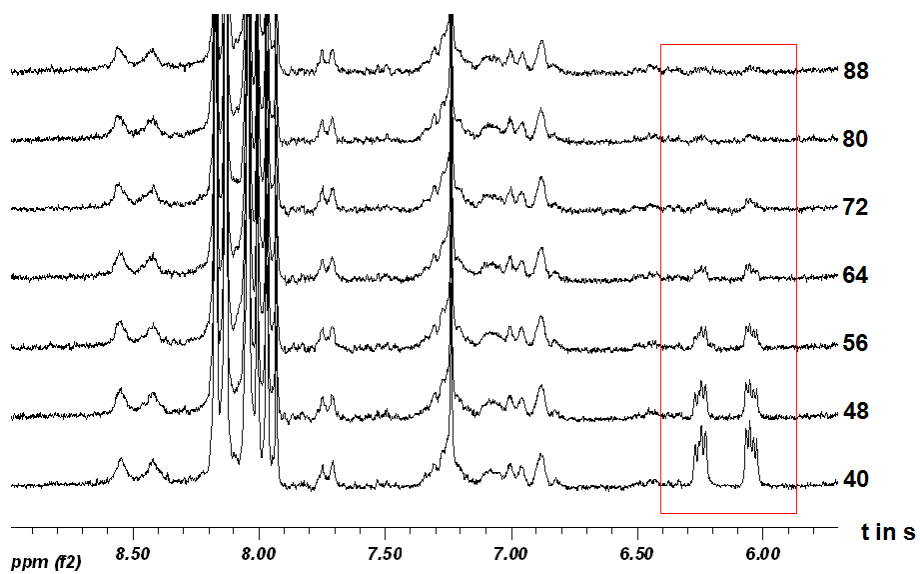


Figure 11. ¹H-NMR spectra of monomer A consumption during polymerization in CDCl₃ at 27° C with Grubbs **III** catalyst.

Bhanuprathap Pulamagatta

Richard Paulick str-13/822, Halle-06124

Germany

Phone-017624271971

E-mail: bhanuprathap.pulamagatta@chemie.uni-halle.de

Personal Details

Date of birth : 16th Oct, 1980
Sex : Male
Nationality : Indian

Educational Qualification

- **PhD in Dept. of Macromolecular Chemistry** (05/2007 – 10/2010)
Prof. Dr. Wolfgang Binder, Martin-Luther-University, Halle (Saale), Germany

Micro- and nanophase separated tubes and rods by melt-infiltration of block copolymers into inorganic nanopores
- **Master of Applied Polymer Science** (10/2004 - 12/2006)
Martin-Luther-University, Halle (Saale), Germany.

Thesis title: Bulk and surface property characterization of winter tire tread compound, at Continental AG, R&D tires, Hannover.

Majors: Polymer synthesis and chemistry, polymer processing, polymer physics.
- **Bachelor of Engineering in Polymer Science and Technology** (1998-2002)
Visveswaraiah Technological University, India.

Thesis title: Studies on thermo mechanical properties of advanced composite materials, at Hindustan Aeronautics Ltd. Bangalore.
- **Research Affiliation:** Research Member (02/2007 – present) - **Max-Planck Institute** for microstructure physics, Halle, Germany.

Professional Experience

- 1) Research Student (05/2006 - 11/2006) - Continental AG, Winter tire tread compound development dept., Hannover, Germany.
 - Research on softeners in winter tire tread compound for better grip on snow and ice surface.
- 2) Research Intern (09/2005 - 02/2006) - Continental AG, Advanced tire materials dept., Hannover, Germany.
 - Winter tire tread compound development for better grip on snow and ice surface.
- 3) Senior Technical Officer (12/2002 - 09/2004) - JK Tires Ltd, Business Unit-1, Mysore, India.

- Technical in-charge of rubber processing (compounding/mixing, extrusion and calendaring).

Publications

1. Synthesis of block copolymers with fluorinated norbornene derivatives via ROMP, Bhanuprathap Pulamagatta, Wolfgang. H. Binder, *Polymer Preprints*, **2008**, 49(1), 353.
2. Homologous Poly(isobutylenes): Novel Poly(isobutylene)/High-Density-Polyethylene-Hybrid-Polymers, Binder, W. H.; Kurzhals, S.; Pulamagatta, B.; Decker, U.; Pawar, G. M.; Wang, D.; Kühnel, C.; Buchmeiser, M. R. *Macromolecules*, **2008**, 41, 8405-8412.
3. Monitoring Block-Copolymer Crossover-Chemistry in ROMP: Catalyst Evaluation via Mass-Spectrometry (MALDI), Binder, W. H.; Pulamagatta, B.; Kir, O.; Kurzhals, S.; Barqawi, H.; Tanner, S. *Macromolecules*, **2009**, 42, 9457-9466.
4. Fiber - and tube - formation by melt infiltration of block copolymers into Al₂O₃-pores, Pulamagatta, B.; Binder, W. H.; Yau, E.; Gunkel, I.; Thurn-Albrecht, T.; Steinhart, M. *Macromol. Symp.* **2010**, 293, 58-62.
5. Block copolymer nanotubes by melt-infiltration of nanoporous aluminum oxide, Pulamagatta, B.; Yau, E.; Gunkel, I.; Thurn-Albrecht, T.; Schröter, K.; Steinhart, M.; and Binder, W. H., *Adv Mater*, **2010**, In Press.
6. Hierarchical nanostructures via micro- and nano-phase separation in semi-fluorinated norbornene block copolymers, Pulamagatta, B.; Pankaj, S.; Beiner, M.; Binder, W. H., *Macromolecules*, **2010**, In Press.

Conferences: Posters and Presentations

1. New fluorinated poly(norbornene)-block co-polymers: synthesis and characterization of phase morphology, 235th *American chemical society meeting*, New Orleans, USA, April-**2008**.
2. Novel Microphase-Separating Poly(norbornene) Block Copolymers: Synthesis and Preparation of 1D Nanostructures, *International Conference Polymeric Materials P-2008*, Halle/Saale, Germany, September-**2008**.
3. Multilayered polymer nanotubes by melt infiltration of ROMP block-copolymers, *ISOM XVIII - 18th International Symposium on Olefin Metathesis and Related Chemistry*, Leipzig, Germany, August-**2009**.
4. Polymer nanotubes with complex wall architectures by melt infiltration of block-copolymers, 8th *International Conference on Advanced Polymers via Macromolecular Engineering (APME)*, Dresden, Germany, October -**2009**.

Languages and Computer skills

- English, German (basic), Kannada and Hindi
- Microsoft Office, Origin, Chem Office, Scifinder

Erklärung zu etwaigen früheren Promotionsverfahren

Hermit erkläre ich, dass ich mich zuvor an keiner anderen Institution um den Doktorgrad beworben und dass ich keinerlei vergebliche Promotionsversuche unternommen habe.

Halle (Saale), Aug-2010

Bhanuprathap Pulamagatta